JAERI-M
6944

STUDY ON X-RAY SPECTROSCOPIC ANALYSIS BY THE USE OF NUCLEAR RADIATIONS FROM RADIOISOTOPES

February 1977

Hiroshi TOMINAGA

日本原子力研究所
Japan Atomic Energy Research Institute

JAERI - M 6944

Study on X-Ray Spectroscopic Analysis by the Use of Nuclear Radiations from Radioisotopes

Hiroshi TOMINAGA

Radioisotpe Center, JAERI

(Received January 27, 1977)

The basis and practice of analytical application of the characteristic X rays of low atomic number elements excited by mainly alpha rays from radioisotopes were studied. Some alpha emitters were proved to be advantageously usable to those elements, in particular, very low atomic number elements, despite their accompanying radiations. Operating characteristics of gas flow proportional counters were fully investigated, and besides, the characteristics of pulse-height distribution continuum in those counters and semiconductor detectors were comparatively studied as the detector for the low energy X rays. For calibration in quantitative analysis by the X-ray spectroscopy, a new simple semitheoretical method for thin specimens is proposed and on the other hand general formulae for matrix correction in thick specimens was derived. An industrial X-ray analyzer to simultaneously analyze four main elements of cement raw material mixtures was constructed with the use of a ^{210}Po alpha-ray source and gain-controlled proportional counters. Problems in practical analysis for the process control were solved and the analyzer has been used routinely in the process for more than ten years. Another analytical application to airborne dust is described as a typical example of application of the proposed calibration method for thin specimens.

JAERI－M 6944

放射性同位元素からの核放射線によるX線分光分析に関する研究

日本原子力研究所，アイソトープ事業部
富永　洋

（1977年1月27日受理）

RI放射線とくにα線により励起される低原子番号元素の特性X線について，その応用の基礎及び実際の研究を行なった。ある種のα放射体は，随伴放射線にもかゝわらず，それら元素とくに超低原子番号元素に有利に利用可能である。ガスフロー比例計数管の動作特性，さらに，低エネルギーX線検出器としての同計数管ならびに半導体検出器のパルス波高連続分布特性の比較検討を行なった。X線分光による定量分析時の検量に関しては，薄い試料のための新しい簡単な半理論法を提案し，また一方，厚い試料のマトリックス補正のための一般式を導出した。^{210}Po α線源とゲイン制御付きの比例計数管を用い，セメント原料中の4主成分を同時分析する，工業X線分析装置を製作した。工程管理上の実際分析における諸問題を解決し，同分析装置は，10年以上の期間にわたり，日常分析に使用されてきた。別に，薄い試料に関して提案した検量法の応用の典型例として，大気浮遊塵試料の分析について述べた。

Contents

1. Introduction

The development of X-ray spectrochemical analysis using radioisotopes as radiation sources has been closely related to the progress in both techniques on artificial radioisotope sources and X-ray measurement. Though the generation of characteristic X rays by radiations from a radioisotope was found at an early time of this century, the proposal of the utilization of the physical phenomena for the X-ray analysis was not made until the middle of 1950's after World War II.

In those days beta-ray emitting isotopes such as ^{90}Sr and ^{147}Pm which were obtained from the fission products of nuclear fuel became available, and studies were systematically made using those kinds of isotopes whose X-ray excitation efficiency is high. The studies on utilization of electromagnetic radiation sources were started afterward. Sources of electron-capture nuclides and secondary sources of radiations excited by beta rays (β-excited X-ray source) have been tested in these days. Nowadays, radioisotope sources emitting electromagnetic radiations (X rays or γ rays) are mostly utilized in many practical analyses in particular for middle atomic number elements, on account of the good signal-to-background ratio. Many kinds of low energy photon sources have been developed successively and they are available as sealed sources. On the other hand, it has been expected that the excitation of X rays by alpha-ray bombardment is advantageous for elements of low atomic numbers. Nevertheless, scarcely any study of the application has been made with an alpha-ray source, because much care is needed to deal with a source with thin film window and also because the measurement of low energy X rays from low atomic number elements is comparatively difficult. Besides,

fundamental studies of X-ray excitation by alpha rays is also not enough and problems remain in particular for the low atomic number region. Thereupon, mainly in the present work, fundamental and application studies on the X-ray excitation by alpha rays were made for low atomic number elements. In this connection, X rays from alpha-emitting isotopes were treated.

On the other hand, the technique of X-ray detection and measurement progressed greatly with the development of scintillation counters, which came to be adopted in most of X-ray fluorescence analyzers with radioisotope sources. In this case, the energy resolution is not good for X rays, so that the selective measurement of X rays is usually made by choosing foil filters. Proportional counters have been often used in studies for their better energy-resolution than scintillation counters. However, they have been little adopted in practical instruments because there are some questions in stability of operating characteristics. In order to use it in an industrial X-ray analyzer which analyses multi-elements simultaneously in the low energy X-ray region, the characteristics of gas flow proportional counters were fully investigated in this work. It was employed finally with automatic control of gain of the whole system including detector and circuit. The remarkable growth of recent semiconductor detectors expanded the area of application of X-ray fluorescence analysis with radioisotopes on account of the excellent capability on energy analysis. Multielement analysis and often trace element analysis are made with the new detectors. Here, the comparative studies were made on the background pulse-height distribution characteristics inherent in detectors, which are related to the capability of trace element analysis, for both semiconductor detectors and proportional counters.

Using a combination of alpha-ray source (with soft X-ray source) and gas flow proportional counters, an industrial X-ray analyzer which simultaneously analyzes four main elements of low atomic numbers in cement raw material mixtures was realized and successfully used for control of raw material supply in a cement factory. This is a case of typical example in the analysis of multicomponents of representative elements in low atomic numbers.

Another typical case of analysis of multielements whose number was more than ten and atomic numbers were neiboring, in thin specimens, was also studied by means of a high resolution semiconductor detector and an X-ray source of alpha-decay nuclide.

The present paper consists of the following eight chapters.

In chapter 2, introductory descriptions are given of theoretical formulae of characteristic X-ray intensities produced by three kinds of radiations and also of the background due to such as scattering of the radiations and bremsstrahlung.

In chapter 3, details of experiments and results on the X-ray yields and cross sections of low atomic number elements for alpha-particle impact are described. Discussions are made in comparison with theory and previous data for protons. (The contents of this chapter have not been published yet.)

In chapter 4, the contribution of gamma and X rays and internal conversion electrons from actual alpha-ray sources to both the characteristic X-ray production and the background are experimentally studied. At the same time, applicability of the X rays from ^{241}Am and tritium sources are discussed. (Partly published).

In chapter 5, firstly, operating characteristics concerning the usage

and construction of gas flow proportional counters for soft X rays are examined, and secondly, pulse-height distribution characteristics relating to the continuum background are investigated for proportional counters and semiconductor detectors. (The latter half has not been yet published.)

In chapter 6, calibration methods including correction of matrix effect for quantitative analysis are given of the two typical cases; thin specimens and thick specimens. Problems of accuracy, precision, and detection limit are also discussed. (Partly published.)

In chapter 7, descriptions are given of an industrial X-ray analyzer with both an alpha-ray source and gas flow proportional counters for analyzing simultaneously the four main components of low atomic numbers in cement raw material mixtures. (Published.)

In chapter 8, two applications are presented. One is quantitative analysis of cement raw mixtures as a performance test of the analyzer described in chapter 7. The other is analysis of airborne particulates as a typical example of multielement analysis in thin specimens by application of the proposed calibration method. (Main part has been published.)

Lastly, a summary is given in chapter 9.

The present paper is a revision of the thesis submitted to Kyoto University in May 1974, in partial fulfillment of the requirement for the degree of Doctor of Engineering. The research work presented was performed partly in Central Research Laboratory of Ube Industries, Ltd. during 1962 to 1965 and later in Radioisotope Center, Japan Atomic Energy Research Institute during 1966 to 1973. About three years have passed since the original manuscript was written, and a remarkable progress has been made in the period in the field. However, a major part of the paper appears to be still in a unique position. Some studies involved are

unpublished. It gives an overall description of the author's work in the field of X-ray spectroscopic analysis with radioisotope sources. The revision was confined to a few parts of apparently inadequte or insufficient description besides expression of sentences and publication form.

2. Excitation of Characteristic X Rays by Nuclear Radiations from Radioisotopes

Every energetic ionizing radiation from a radioisotope causes the ionization of inner shells of atoms in passage of the radiation in matter. Then, the vacancy of an inner shell is filled by an outer-shell electron, and the characteristic X ray or the Auger electron is emitted from the ionized atom. The fraction of characteristic X-ray emission has a constant value which depends only on atomic number (Z) and is called fluorescent yield.

The probability of the inner shell ionization is greatly different from one to another depending on the kind of incident radiation, its energy, and the atomic number of target atoms. The ionization by electromagnetic radiations is well known as the process of photoelectric effect and the cross section has also been well investigated. The ionization and production of characteristic X rays by electrons are also familiar phenomena in the conventional X-ray technique. Although the energy of beta rays is continuously distributed and mostly much higher than that of the electrons used in the conventional X-ray technique, the production of X rays by beta rays was studied by several researchers in the relation with monoenergetic electrons, when beta-emitting isotopes became easily available. The studies of X-ray production by alpha rays are not many and problems are still left, whose discussion in detail will be given in the next chapter(3.).

In this chapter, fundamental formulae and theoretical relations of X-ray intensities from a target bombarded by radiations are presented.

2.1 Excitation by Gamma and X Rays

The number of characteristic X-ray photons emitted from a sample irradiated by monochromatic X rays or gamma rays is calculated by using the photoelectric cross section as follows (cf. Fig. 1).

The primary radiation of intensity I_1 (number of quanta per second) making an angle ϕ_1 with the sample surface, as shown in Fig. 1, is attenuated to $I_x = I_1 \exp[-\mu_1 \rho x \operatorname{cosec} \phi_1]$ at depth x from the surface, where μ_1 is the mass absorption coefficient of sample matrix for the primary radiation, ρ is the density of sample matrix. In a thin layer of thickness dx at this depth, a certain fraction $dI_x = I_x M_i \mu_{\tau i}(1 - 1/Ji)$ dx cosec ϕ_1 is absorbed by ionization of a particular shell (for example K shell) of an element i to be measured. Mi is the mass of element i per unit volume in the sample, $\mu_{\tau i}$ is the photoelectric mass absorption coefficient of element i, and Ji is the jump ratio of $\mu_{\tau i}$ at the absorption edge. The fraction $\omega_i g_i$ of dI_x leads to a secondary radiation of interest (for example K_α radiation). ω_i is the fluorescent yield and g_i is the probability of a particular electron transfer in a series (K_α or K_β, etc.). The intensity of the secondary radiation (characteristic X rays) emitted by the thin layer dx into an unit solid angle in direction of an angle ϕ_2 with the sample surface, $\omega_i g_i dI_x/4\pi$, is then reduced to $(\omega_i g_i dI_x/4\pi) \cdot \exp[-\mu_2 \rho x \operatorname{cosec} \phi_2]$ before reaching the sample surface. μ_2 is the mass absorption coefficient of sample matrix for the secondary radiation. Thus the contribution of the layer dx to the intensity of characteristic X rays of element i per steradian is given by

$$dI_2 = I_1 \exp[-(\mu_1 \operatorname{cosec} \phi_1 + \mu_2 \operatorname{cosec} \phi_2)\rho x] M_i \mu_{\tau i} \times \left(1 - \frac{1}{J_i}\right) \omega_i g_i dx \operatorname{cosec} \phi_1 \cdot \frac{1}{4\pi}. \quad (2.1)$$

Integration of Eq. (2.1) for x from zero to the sample thickness d gives

$$\left.\begin{aligned} I_2(d) &= I_1 K_i M_i \frac{1}{4\pi} \frac{1-\exp[-\mu\rho d]}{\mu\rho} \quad , \\ K_i &= \mu_{\tau i}\left(1 - \frac{1}{J_i}\right) \omega_i g_i \operatorname{cosec} \phi_1 \quad , \\ \mu &= \mu_1 \operatorname{cosec} \phi_1 + \mu_2 \operatorname{cosec} \phi_2 \quad . \end{aligned}\right\} \tag{2.2}$$

In the case of sufficiently thick sample,

$$\left.\begin{aligned} I_2(\infty) &= I_1 \frac{K_i}{4\pi} \frac{W_i}{\mu} \quad , \\ W_i &= M_i/\rho \quad . \end{aligned}\right\} \tag{2.3}$$

W_i is the weight fraction of element i in the sample. The expression $(1/4\pi)\cdot(K_i W_i/\mu)$ gives the theoretical X-ray yield of thick target in a particular backward geometry (X rays per primary radiation quantum per steradian).

In the above consideration, matrix enhancement effects and multiple scatter effects are neglected but they are usually very small. And the above formulae are only valid for completely homogeneous samples.

On the other hand, the intensity of scattered radiations (single scatter) is similarly obtained by substituting the product of the scattering mass absorption coefficient of sample matrix and the sample density, $\mu_s\rho$, for $\mu_{\tau i}(1 - 1/J_i)\omega_i g_i M_i$. In the substituted equations, μ_2 is the mass absorption coefficient for the scattered radiation.

The ratio of the photoelectric absorption to scatter given by $\mu_{\tau i}/\mu_s$ and the value of $\mu_{\tau i}$ itself become the largest when the energy of primary radiation is just above the absorption edge, and they

decrease with increase of primary-radiation energy. The same tendency can be seen also in the intensity ratio of characteristic X rays to scattered rays, even if the effect of μ is taken into account.

2.2 Excitation by Beta Rays

It is known that the intensity of beta rays having a continuous energy spectrum attenuates nearly exponentially with thickness of absorber and the mass absorption coefficient is nearly independent of the atomic number of the absorber. For example, $\mu_\beta = 17/E_m^{1.14}(cm^2/g)$ (Al)[1], where E_m is the maximum energy of the beta-ray spectrum in MeV.

On account of the above property, the intensity of the characteristic X rays excited by beta rays can be described approximately by the formulae of the same shapes as Eqs. (2.1), (2.2), and (2.3), where $\mu_1 = \mu_\beta$ and $K_i = \varepsilon_{K_i}\omega_i g_i$ cosec ϕ_1. ε_{K_i} is the mean cross section of K shell ionization of element i, in unit of cm^2/g, in the case where the ionization is assumed to be produced uniformly along the range of beta-rays (this assumption has been experimentally confirmed[2]), and it is related to the total number of K shell ionization of element i produced in a thick target by a quantum of beta rays, n_K;

$$\varepsilon_{K_i} = n_K/R_m, \tag{2.4}$$

where R_m is the maximum range of beta rays. And n_K is expressed by

$$n_K = N_i \int_{E_K}^{E_m} N_\beta(E')dE' \int_{E_K}^{E'} \sigma_{K_e}(E)\left(\frac{dR}{dE}\right)dE , \tag{2.5}$$

neglecting the indirect ionization by bremsstrahlung produced in the target by beta rays (correction may be necessary for higher Z elements), where

E, E' : the energy of beta particle,

E_m : the maximum energy of beta rays,

E_K : the energy of K absorption edge of element i,

$N_\beta(E')$: the normalized energy distribution of beta rays,

$R(E)$: the range of beta particle with energy E, (g/cm^2),

$\sigma_{K_e}(E)$: the atomic cross section of K shell ionization of element i by electrons of energy E, (cm^2),

N_i : the number of atoms of element i per gram.

The K shell ionization cross section is given by the modification[3] of Bethe's non-relativistic formula;

$$\sigma_{K_e} = (7.92 \times 10^{-20}/E_K E) \ln E/E_K, \tag{2.6}$$

where E and E_K are given in keV unit. In the case of monoenergetic electrons of initial energy E_o, the calculation of Eq. (2.5) is performed straightforwardly, if the range-energy relation of Thomson-Whiddington[4] is employed;

$$E_o^2 - E^2 = cR(E),$$

where c is a constant but varies with E_o. Then,

$$n_K = 1.58 \times 10^{-19} \cdot \frac{C}{c} Ni \left[U_o \ln U_o - (U_o - 1) \right], \tag{2.7}$$

where $U_o = E_o/E_K$, and C is the correction factor for the effect of electron backscattering from the target ($C < 1$ but $C \simeq 1$ especially for low Z element).

For beta rays with continuous and higher energy, a simple approximation formula of σ_{Ke} given by Voyvodic[5] can be used conveniently:

$$\frac{N_o}{A} \sigma_{Ke} = 10^6 \cdot Z^{-4}, \quad (cm^2/g), \tag{2.8}$$

where N_o is Avogadro's number and A is the atomic weight of target element. On the other hand, the range-energy relation for beta rays is in general written as

$$R(E) = aE^n - b \ , \tag{2.9}$$

where a, b and n are constants determined experimentally: for example[6], taking E in MeV and R in mg/cm^2,

$E > 0.7$ MeV : $a = 0.543$, $b = 0.160$, $n = 1$,

$0.8 > E > 0.15$ MeV : $a = 0.407$, $b = 0$, $n = 1.38$.

Here, suppose that $E_m \gg E_K$. The integration of Eq. (2.5) can be performed simply using Eqs. (2.8) and (2.9):

$$n_K = 10^6 \cdot Z^{-4} \cdot a \cdot \bar{E}^n \ , \tag{2.10}$$

where

$$\bar{E}^n = \int_0^{E_m} E^n N_\beta(E) dE \ . \tag{2.11}$$

Although scattered beta rays can be usually eliminated by using a foil filter or a magnetic field, bremsstrahlung produced in a sample target causes a serious interference in many cases of characteristic X-ray measurement. The higher the beta energy, the more serious the problem. The intensity of bremsstrahlung also can be expressed by the formulae of the same shapes as Eqs. (2.1), (2.2), and (2.3), provided that $\varepsilon_B \rho$ is substitutes for $\mu_{\tau i} (1 - 1/J_i) \omega_i g_i M_i$, where ε_B is the bremsstrahlung production cross section in cm^2/g unit in the sample matrix. The values of ε_B of various elements and various beta energies have been obtained experimentally[7].

2.3 Excitation by Alpha Rays

Since alpha rays with a uniform energy pass straight for a definite range in matter until they stop, they do not have a mass absorption coefficient such as in X or gamma rays and also in beta rays. Therefore, the intensity of characteristic X rays excited by alpha rays must be expressed by a different form from Eqs. (2.1), (2.2), and (2.3).

In the same geometry as in gamma and X rays (Fig. 1), the yield of X rays (the number of characteristic X-ray photons per alpha quantum per steradian) is given by

$$Y(E_0) = \frac{N_i}{4\pi}\omega_i g_i \int_{(R_0-Rd)\geq 0}^{R_0} \exp\left[-\mu_2 \frac{\sin\phi_1}{\sin\phi_2}(R_0-R)\right]\sigma_K[E(R)]dR \qquad (2.12)$$

where

E_0, E : energy of alpha particle incident on a slab of material, and after losing some of its energy, (MeV),

R_0, R : range of alpha particle of energy E_0, E, in the target material, (g/cm^2),

$Rd = d \operatorname{cosec} \phi_1$: the maximum amount of target material that can be traversed by the incident alpha particles, (g/cm^2),

$\sigma_K(E)$: the atomic cross section of K shell ionization of element i by alpha particle of energy E, (cm^2),

and the other symbols are the same as described already. The integral is performed along the path of incident alpha particles. A range-energy relation of alpha particles is required for the calculation.

A comprehensive description concerning the cross section of inner shell ionization is given by Merzbacher and Lewis[8] with the summary of experimental works at the early time. The inner shell ionization by alpha particle impact is described by the Coulomb interaction between

the incoming alpha particle and the inner shell electron of target atom. The calculation of the cross section is made with the Born approximation for inelastic collision, substituting plane waves for the Coulomb wave function for representation of the incident and scattered particle states, and further approximating the initial state of the bound electron with hydrogenic wave functions with an effective charge.

The cross section for the K shell is written as

$$\sigma_K = 8\pi z^2 a_o^2 Z_K^{-4} \eta_K^{-1} f_K \ , \tag{2.13}$$

$$f_K = \int_{\theta_K}^{\infty} dW \int_{\frac{W^2}{4\eta_K}}^{\infty} \frac{dQ}{Q^2} \mid F_{WK}(Q) \mid^2 \ , \tag{2.14}$$

$$\mid F_{WK}(Q) \mid^2 dW = \frac{dW}{1-\exp[-2\pi/k]} \frac{2^7 Q(Q+\frac{1}{3}k^2+\frac{1}{3})}{\{(Q-k^2+1)^2+4k^2\}^3}$$

$$\times \exp\left[-\frac{2}{k}\arctan\left(\frac{2k}{Q-k^2+1}\right)\right] , \tag{2.15}$$

where $W = k^2 + 1$,

z : electric charge (atomic number) of incident particle; $z = 2$ for alpha particle,

a_o : the Bohr radius of hydrogen, 5.2915×10^{-9} cm,

Z_K : the effective nuclear charge seen by an electron in K shell, $Z_K = Z - 0.3$; Z = atomic number of target atom,

$\eta_K = \frac{mE}{MZ_K^2 Ry}$: a dimensionless measure of the energy of the incident particle; m = electron mass, M = atomic mass (g/g mol) of incident particle, Ry = Rydberg constant (13.60 eV),

θ_K : the screening factor defined against the "ideal ionization potential of the K-shell without outer screening" (Z_K^2Ry); suitable values are given in Ref.9: $\theta_K = \frac{E_K}{Z_K^2 Ry} - \frac{Z_K^2}{4}(\frac{1}{137})^2$.

The results of the calculation of f_K is tabulated in Ref. 10. f_K is a function of η_K and θ_K. f_K, therefore also σ_K, increases with η_K (therefore with E), having a maximum near $\eta_K = 1$ (the velocity of incident particle equaling the rms K-shell electron velocity) and then descending slowly. The dependence of σ_K on target atomic number is great, and it is expected that the lower the target atomic number, the higher the efficiency of K-shell ionization production.

Though the number of experimental works on K X-ray production by alpha rays is not many, comparatively many works have been made by protons in various energies. The data of cross sections for different projectiles can be compared or converted to each other because $\sigma_K Z_K^4/z^2$ in the above theory is defined only by η_K in the same target and independent of kinds of projectiles.

Many of experimental results agree with the theory in general shape of the energy dependence but not necessarily in absolute value. For example, experimental cross sections in low energy region evidently fall much lower than the theoretical values. In these region, the semi-classical theory given by Bang and Hansteen[11], in which the deflection of the projectile in the Coulomb field of the target nucleus is taken into account, would be useful because the Coulomb-deflection of incident particle by target nucleus is of importance in low bombarding energy. Additional correction for the effect of the binding of the K-shell electron to the projectile has been introduced by Brandt et al[12].

Independently of the above theories (the Born approximation), Garcia[13] has introduced a new approach based on the binary-encounter-impulse approximation, which appears to agree well with experiment for protons and alpha particles. In this theory, the interaction between the incident particle and the bound electron is treated as the collision of the incident particle with a free electron whose momentum distribution is established by the nucleous of the target atom. Garcia et al have also published a review paper[14] on the inner shell ionization by the bombardment of charged particles including ions heavier than alphas.

The efficiency of characteristic X-ray excitation by alpha particles is not high compared with that by beta rays, except for very low Z elements. The X-ray yield for alpha particles roughly corresponds to that for far less energy electrons, for usual metal elements. On the other hand, however, a remarkable advantage of alpha ray bombardment is that both of production of bremsstrahlung (except the case of higher energy alpha particles from accelerators) and back scattering of the primary radiations are almost negligible, so that the high signal-to-noise ratio would be expected in the measurement of characteristic X rays. In practice, the application to the low Z through very low Z elements for which the efficiency of X-ray production is fairly good may be advantageous.

3. Fundamental Measurements of Characteristic X Rays Excited by Alpha Particles

Absolute measurements of characteristic X-ray yields or cross sections due to K-shell ionization by alpha particle bombardment[15)-18)] are not many even including an early work[15)] using a Geiger counter (in early works[15)16)] the total X-ray production without X-ray absorption was obtained and the cross section was not obtained) and also more recent study[18)] using high energy alpha particles from an accelerator. Only the two of them[15)17)] treat low Z elements (Mg, Al). There are a few more works[12)13)19)-26)] for low Z elements ($Z \leq 13$) using protons, but most of them are done with low energy protons ($Ep < 200$ keV) and very limitted[19)-21)] is the number of data for the protons the velocity of which is in the same region as that of alpha particles from radioisotopes.

The theoretical calculation by use of the Born-approximation may be difficult to apply to low Z elements, because the assumption underlying the approximation, that the electron orbits will not be polarized much by the approaching particle, breaks down for the low Z atom in which the electrons are not strongly bound. The problem must be more serious for alpha particles than for protons. Whether the binary-encounter approximation agrees with experiment for such a low Z element or not, is also a problem.

In this chapter, descriptions are given of experiments made for measurements of the X-ray yields and cross sections for low Z elements with alpha particles from a radioisotope, and the results are compared with those of calculation and the data for protons. Also comments are given for comparison with the X-ray production by electrons and photons.

3.1 ^{241}Am Source

The alpha-ray source used is a ^{241}Am source made by RCC (Amersham) to the special order (the same type as ^{210}Po disc source[27]). ^{241}Am is deposited onto a platinum plate which is mounted on an aluminum source holder. The active diameter is about 10 mm. The outer diameter and height of the source holder are 18 mm and 3.5 mm, respectively. The front of the source is covered by a mica window of somewhat thicker than 1 mg/cm^2. To employ the source safely in vacuum, a nickel meshes of 70% transmission has been additionally attached.

The source emits, besides alpha particles [original energy 5.49 MeV (86%), 5.44 MeV (13%)], low energy gamma rays, internal conversion electrons (ca. 21 to 58 keV), and accompanying characteristic X rays (NpL, M), and furthermore X rays excited from the platinum plate and the nickel meshes. The fractions of the X and γ rays measured by a Si(Li) detector are shown in Table 1. The radioactivity measured by comparing the intensity of 59.56 keV gamma rays with that of a ^{241}Am reference source (IAEA 10 μCi) was 2.16 mCi (±2.3%).

The number of emergent alpha particles was directly measured in a definite geometry in vacuum by using a silicon PN junction detector [(1) Toshiba M8811A (3 mm^2), (2)M8810A (20 mm^2), or (3) Mitsubishi SD-031-30 (7.1 mm^2)]. The result was 4.28×10^6 (±5%) alphas per steradian, which agreed within the error with the activity measured for gamma rays. The alpha particle energy spectrum taken by the detector (1) is shown in Fig. 2 (curve A). The gentle slope in the low energy side is due to energy loss in the window and the source itself. The width of the distribution in FWHM is 0.52 MeV, and the mean energy $\overline{E}_0$ is 3.93 MeV. To change the energy of alpha particles incident to a target, Mylar

films of 6 μm (0.89 mg/cm^2) were put in the collimated beam (cf. next section). The energy spectra with Mylar films are shown in Fig. 2 (curves B and C). The mean energies and the distribution widths are 2.97 MeV and 0.64 MeV for the case of one sheet of Mylar, and 1.88 MeV and 0.78 MeV for the case of two sheets of Mylar, respectively. As is seen in Fig. 2, the number of alpha particles after passing through Mylar films decreases by small extent because the alpha particles with near zero energy are stopped in the films. The ratios of total alpha particles with and without Mylar films are 0.983 and 0.871 for one and two sheets of Mylar, respectively.

3.2 Apparatus and Measuring Geometry

The experimental layout is shown in Fig. 3. The source and a sufficiently thick target are arranged in vacuum (< 0.2 mmHg) which is separated from the counter by a thin film window with nickel meshes of 38 % optical transmission. Incident alpha particles to a target are collimated by a lead collimator covered with brass and aluminum plates, and also X rays from the target to the counter are collimated by a frame of the counter window. Both the incident angle of alpha particles to the target and the take-off angle of X rays from the target to the counter are 45 degrees with the target surface, for the axes of the beams.

The proportional counter used for measuring characteristic X rays is a gas-flow type counter which is operated with PR gas (90 % argon plus 10 % methane) at one atmosphere. Two kinds of films were used for the window : (a) 0.138 mg/cm^2 stretched polypropylene film for the lower energy X rays, and (b) 0.808 mg/cm^2 aluminized Mylar film for the higher energy X rays. Fig. 4 shows the intrinsic detection efficiencies

calculated for these two detectors. The values of mass absorption coefficients used for the efficiency calculation were taken from Refs. 28 and 29 for the energies lower and higher than 1 keV, respectively. The errors of the detection efficiencies due to uncertainty in mass absorption coefficients are considered to be within 10% at most. Output pulses from the detector were fed through a preamplifier to a 400 channel analyzer (TMC 401D) for pulse height analysis.

A magnet was located between the source and the target to exclude the conversion electrons of ^{241}Am from the beam of primary radiations. The pole area is 20 mm × 25 mm, the pole gap 10 mm, and the magnetic field about 2000 gauss, which is sufficiently strong to remove the conversion electrons but does not affect the passage of the alpha particles. The contribution of X and γ rays emitted from the source to excitation of X rays was evaluated by absorbing alpha particles with 6 sheets of 6 μm Mylar films over the source collimator.

3.3 Measurements of X-Ray Yields

The KX rays of C, F, and Mg were measured with the detector (a) for thick disc targets of graphite, teflon, and magnesium, respectively. Similarly, the KX rays of Mg, Al, Si, S, Cl, Ca, and Ti were measured with the detector (b) for discs of magnesium, aluminum, silica, sulfur, sodium chloride, calcium carbonate, and titanium, respectively.

Figs. 5 and 6 show pulse-height spectra of C KX rays and F KX rays produced by the ^{241}Am source without Mylar, measured with the detector (a). In both spectra the contribution of X and γ rays from the source was found to be insignificant, and therefore the background subtraction was not necessary. Pulse-height spectra of the higher Z elements, measured with

the detector (b), with and without 6 sheets of Mylar against the primary radiations are shown in Fig. 7, where the excitation of characteristic X rays by the γ and X rays can be apparently seen.

A total net peak area was obtained by summing up counts of channels in a peak region above the continum background. The peak area in a spectrum measured with 6 sheets of Mylar gives the count of the γ- and X-ray-excited X rays; it was corrected for absorption of the soft X-ray components of the primary radiations (especially Np M) by the Mylar films (cf. 4.2). The observed count of alpha-ray-excited X rays, N_{obs}, was given by substracting the corrected count of the γ- and X-ray-excited X rays from the peak area with 0, 1, or 2 sheets of Mylar films.

The experimental thick target yield of KX rays (photons per alpha per steradian), Y_{exp}, was obtained from N_{obs} by the formula

$$Y_{exp} = \frac{N_{obs}}{I_o \Omega_t \Omega_d \epsilon_d} \quad , \tag{3.1}$$

where

I_o : the number of alpha particles incident on the target per steradian in the counting time,

Ω_t : the solid angle of target as viewed from the center of the source (0.0597 sr),

Ω_d : the solid angle of detector as viewed from the center of the target [0.135 sr for the case of detector (a), and 0.171 sr for the case of detector (b)],

ϵ_d : the efficiency of X-ray detection with correction for transmission of the meshes.

This formula is based on the fact that the emission of KX rays is

isotropical.

The experimental thick target yields of KX rays produced by alpha rays are listed in Table 2. In the case of compound target, the yield listed is one multiplied by the ratio of the pure element yield to the compound yield which are both calculated theoretically by using Eqs. (2.12) through (2.15) (the procedure of the theoretical calculation is described later).

The quoted errors for the results in Table 2 were derived from (1) the statistical variations (two times the standard deviation) in the determination of peak area, and (2) the uncertainty in the estimation of the denominator of Eq. (3.1) which was assessed at 10% from the situation of agreement between theory and experiment in the gamma- and X-ray-excited X rays for the same ^{241}Am source (cf. 4.2, Fig. 18). These were treated as random errors and combined in the usual manner.

Fig. 8 is a plot of the thick target yields for the alpha rays of $\overline{E}_o$ = 3.93 MeV versus the characteristic X-ray energy.

3.4 Discussion

3.4.1 Calculation of theoretical yields

The theoretical thick target yields drawn in Fig. 8 were calculated by two methods : (1) directly using Eq. (3.2) rewritten from Eq. (2.12), taking the mean energy (3.93 MeV) for E_o, and (2) integrating Eq. (3.2) for all the alpha-energy distribution by Eq. (3.3);

$$Y(E_o) = \frac{N_i}{4\pi}\omega_i \int_o^{Ro} \exp\left[-\mu_2(Ro - R)\right]\sigma_K\left[E(R)\right]dR, \qquad (3.2)$$

$$\overline{Y(E_o)} = \int_o^{E_m} Y(E_o)N_\alpha(E_o)dE_o, \qquad (3.3)$$

where $N_\alpha(E_o)$ is the normalized energy distribution of alpha particles, and E_m is the maximum energy of the distribution. The theoretical yield ratio of pure to compound mentioned above was calculated by the method (2). The calculation of Eq. (3.2) was carried out by means of a computer using the cross section obtained from Eqs. (2.13) through (2.15), numerical values of the alpha range, the mass absorption coefficients, etc.

The range-energy relations used were obtained by the following procedure:

(1) atomic stopping cross sections for alphas, ϵ_α, were derived from the graphs of atomic stopping cross sections for protons, ϵ_p, in Ref. 30, using the relation

$$\epsilon_\alpha(E_\alpha) = k\epsilon_p \quad (Ep = E_\alpha/3.97), \tag{3.4}$$

where k = 4.0 for $E_\alpha \geq 1.6$ MeV and the values of k for $E_\alpha \leq 1.6$ MeV are given in Ref. 30 (Table 2d),

(2) tentative ranges were given by

$$R(E) = R(E_1) - \int_E^{E_1} \frac{dE}{\epsilon_\alpha(E)} \quad , \quad (\text{atoms/cm}^2), \tag{3.5}$$

where experimental values of R at 7.68 MeV in Ref. 30 (Table 7) were chosen for $R(E_1)$,

(3) thus obtained tentative ranges were adjusted by shifting in parallel so as to cross the origin in a graph of range versus energy,

(4) the adjusted ranges were plotted versus Z and smoothed curves were drawn for various energies,

(5) the values on the smoothed curves, after conversion of the unit from atoms/cm^2 to mg/cm^2, were plotted versus energy, and finally, the numerical values were read every 0.05 MeV from the graph.

The obtained range-energy relations are shown as examples in Fig. 9. The range in compounds were computed by the Bragg-Kleeman Rule[31] that the range in mg/cm^2 unit is approximately proportional to the square root of the atomic weight of substance, A ;

$$\frac{R}{R_o} = \frac{\sqrt{A}}{\sqrt{A_o}} , \tag{3.6}$$

in which the effective atomic weight of a compound or a mixture is given by

$$\sqrt{A} = \frac{\Sigma\ n_i A_i}{\Sigma\ n_i \sqrt{A_i}} , \tag{3.7}$$

where n_i is the atomic fraction of the element whose atomic weight is A_i.

The mass absorption coefficients of characteristic X rays for pure elements were adopted from Ref. 28, and that for a compound was obtained by calculating a weighted average using weight fractions of component elements. For the K-shell fluorescent yields, theoretical values estimated by Walters and Bhalla[32] were used, which appear to be comparatively accurate in the low Z region.

3.4.2 Comparison with theory and previous proton data

As seen in Fig. 8, the theoretical yield curves give estimates close to the points of experimental data on the whole. Strictly speaking, however, the curves lie significantly below the carbon data and above the others. The fairly good agreement between the two curves shows that the yield for alpha rays having the energy distribution of Fig. 2 can be represented by that for an alpha ray whose energy is equal to the mean energy.

Thereupon, the experimental yields are plotted against the mean energies in Fig. 10, where the experimental yields for protons[21] are also plotted for comparison. There is no published data of thick target yields for alpha particles to be compared in this energy domain and for low Z elements. To compare data for alphas and protons, the following relations were taken into account. First of all, for alphas and protons incident on the same target,

$$\sigma_{K_\alpha}(E_\alpha) = 4\,\sigma_{Kp}(Ep = E_\alpha/3.97), \tag{3.8}$$

from Eqs. (2.13) to (2.15). On the other hand, as described already in Eq. (3.4),

$$\frac{dE}{dx}(E_\alpha) = 4\,\frac{dE}{dx}(Ep = E_\alpha/3.97), \tag{3.9}$$

for $E_\alpha \geqq 1.6$ MeV. From Eq. (3.9),

$$dR(E_\alpha) \simeq dR(Ep = E_\alpha/4) \tag{3.10}$$

is obtained, where dR is the incremental decrease in range for the particle after traversing a thickness dx of material. Then, using Eqs. (3.8) and (3.10) into Eq. (3.2), the relation between yields for alphas and protons is given as

$$Y_\alpha(E_\alpha) \simeq 4\ Yp\ (Ep = E_\alpha/4). \tag{3.11}$$

The relation of Eq. (3.11) was used to plot the proton data in Fig. 10.

It should be noted that , although a significant discrepancy between the experiment and the theory is seen in Fig. 8, the agreement between the data for alphas and protons is fairly good, in Fig. 10, for the three targets at E_o = 3.93 MeV.

In the lower alpha energies, however, the alpha data for carbon come obviously above the proton data, while those for magnesium and aluminum still agree with the proton data, respectively.

Since the uncertainties in both mass absorption coefficients and fluorescent yields (especially the latter) may be large in low Z elements (for example $Z \leq 12$), considerable errors in calculation of the theoretical yields might be involved for such elements. Therefore, one can not conclude the failure of the theory itself directly from the discrepancy between theory and experiment. However, at least, the fact that the yield of C KX rays for 2 to 3 MeV alphas is significantly higher than that for corresponding protons appears to be a positive evidence of breakdown of the theories (cf. 3.4.3).

3.4.3 Ionization cross section

The K-shell ionization cross section is calculated from data of the thick target yield by using Eq. (3.12)[8] which is derived by differentiation of Eq. (3.2).

$$\sigma_K = \frac{4\pi}{\omega_i N_i} \left[\frac{dY}{dE} \frac{dE}{dR} + \mu_2 Y \right] . \qquad (3.12)$$

The calculations were carried out at alpha energies of round numbers by interpolating or extrapolating data of Table 2. Values of stopping power, $\frac{dE}{dR}$, were taken from slopes of the range-energy relations described already (cf. Fig. 9). For ω_i and μ_2, the same values as used in the calculation of Eq. (3.2) were employed. The results were listed in Table 3.

The errors for the tabulated values are as follows. For carbon, since the second term in Eq. (3.12) is dominant, the error in σ_K is estimated from uncertainties in μ_2 and ω_i (possibly $< 50\%$ in total) while

the error in the measurement may be about 10%. Conditions are different for the other elements; the first term is larger or comparable compared with the second term, and the uncertainty in μ_2 is not so large, thus the resulting errors of σ_K/ω_i may be within 30% (but only for sulfur at the lowest alpha energy, somewhat larger due to the count error : 40%), and the error of ω_i used are considered to be 10% at most.

Fig. 11 shows a comparison of the determined K-shell ionization cross sections with theoretical calculations in the Born approximation[8] and with previous data by proton impact[21]. Here, to reduce all data to one graph, $\theta_K Z_K^4 \sigma_K/z^2$ and η_K/θ_K^2 are adopted as ordinate and abscissa, respectively, since the former is a common function of the latter approximately independently of kinds of projectile and target[8]. But as shown in Fig. 11, it is noted that there is some small difference between the two theoretical curves for different values of θ_K. In this connection, the values of θ_K given by the formula described in section 2.3 are 0.64, 0.70, 0.71 and 0.75 for C, Mg, Al and S, respectively. Previous data by proton impact were recalculated from the original data by using the same values of μ_2 and ω_i as used for the data of alphas (cf. Table 3).

Similarly, Fig. 12 shows a comparison of the same experimental data with the theory based on the binary-encounter-impulse approximation[13)14)]. Here, E_K is the binding energy of K electrons and λ is the mass ratio of projectile to proton. The quantity of $E_K^2\sigma_K/z^2$ is practically a universal function of $E/(\lambda E_K)$. Distinguishable difference in the theory between alphas and protons arises only for $E/(\lambda E_K) < 100$ [at $E/(\lambda E_K) = 76$, $E_K^2\sigma_K/z^2$ for alphas is 10% higher than that for protons[13)]].

In Figs. 11 and 12 the agreement between the present data for alpha particles and the previous data for proton impact is fairly good for

magnesium and aluminum, but the difference in carbon data is considered to be a sign of substancial discrepancy between the cross sections for alpha particles and protons, corresponding to the difference in thick target yields for the two projectiles. Hitherto, some studies have been made on projectile charge dependence of the cross section concerning target atoms of higher Z than magnesium. The difference in the carbon data described above is considered to be similar to that in the existing data of the projectile charge dependence; the relative difference in cross section between two different-charge projectiles seems to increase with decreasing Z of target (cf. Ref. 14). Further investigation is required to theoretically fully understand charge dependence of the cross section.

The agreement between the experimental data and the two kinds of theoretical curves is not so bad, except the lower part of the graph, when taking account of the uncertainty in the absolute values of cross sections. Of the two curves, the binary encounter approximation seems to give, on the whole, an estimate closer to experimental data than by the Born approximation, as is already pointed out[13)14)]. The upward deviation of alpha particle data for carbon from the curve of the binary encounter approximation near the peak resembles that of previous alpha data for iron, nickel and copper[14)]. These would be explained in the future by modification of the theory of the ionization cross section itself, variation of the fluorescent yield, or the satellite structure in the X-ray spectrum.

3.4.4 Discussion for application

From the practical point of view, the situation that the production of X rays of a very low Z element by alpha rays does not much decrease with alpha-ray energy down to 2 MeV is clearly advantageous for the

application, because an alpha-ray source with a sufficiently thick window which is desirable for safety can be used and the interference due to X rays of higher Z elements in a sample is decrease by use of lower energy alpha rays. The efficiency of X-ray excitation of higher Z elements (for example $Z \geq 12$) decreases rapidly with alpha-ray energy, so that a thinner-window source may be needed to excite X rays of such a higher Z element. The energy dependences of thick target yields of KX rays for Mg, Al, ans S in the energy range of 2 ∿ 4 MeV were found to be approximately $E^{2.9}$, $E^{3.2}$, and $E^{3.8}$, respectively. The Z dependences of the yields for Mg (Z = 12) through Ca (Z = 20) were $Z^{-7.1}$, $Z^{-5.8}$, and $Z^{-4.8}$ for E = 2, 3, and 4 MeV, respectively.

Finally, the obtained thick target yield of Ti for 4 MeV alpha particles almost equals to that for 20 keV electrons calculated by the formula $\omega_i n_k/4\pi$ using Eq. (2.7) without absorption of X rays (the absorption is less than 10% since $ZE_o/E_k < 100$[3]). The yield for alpha rays increases rapidly with decreasing Z, while the yield for electrons without absorption correction increases only by a factor of 2 or 3 for lower Z. As a result, the yields of Al and C for 4 MeV alpha rays become 6 and 34 times larger than the quantities $\omega_i n_k/4\pi$ of respective elements for 20 keV electrons. (When the absorption of X rays is taken into account in calculation of the yields, the values of the ratios will become larger than the above). Moreover, it should be noted that the yield of very low Z elements such as carbon is hardly increased even if the electron energy is increased, because the X-ray absorption coefficient is very large and the ionization cross section itself decreases with increase in electron energy. The KX-ray yields of the elements of $Z \leq 13$ for 4 MeV alpha rays are larger than the quantities $\omega_i/4\pi$. This means

that the yield for the alpha rays in such a low Z region is larger than the yield for gamma or X rays, because the latter is somewhat less than the quantity $\omega_i/4\pi$ at most. In particular the yield of C KX rays for the alpha rays turns out to be more than 200 times $\omega_i/4\pi$.

4. Characteristics of Radioactive Sources

The experimental investigation of X-ray production by alpha particles from radioisotopes has been described in detail in chapter 3. However, no pure alpha-ray emitter can be utilized in practice. Actual alpha-ray emitters usually are accompanied by gamma rays, internal conversion electrons, and characteristic X rays. The contribution of these radiations to the X-ray production and the background in measurement may be an important problem in application of alpha-ray emitters. It relates also to the form of sources ; for example, the window material and thickness, the backing metal, etc. Contrarily, the gamma and X rays from alpha-decay isotope sources may be usable for some analyses. The characteristics of X-ray production and background are presented for a few typical sources of alpha rays and low energy gamma and X rays in this chapter, to clarify applicability of radioactive sources to the spectroscopic analysis of in particular low Z elements.

4.1 Alpha-Ray Sources

4.1.1 Contribution of conversion electrons

The ^{241}Am alpha-ray source used in the experiment of chapter 3 is again taken up to a subject of investigation as a typical alpha-ray source accompanied by conversion electrons and gamma and X rays. By using the same source and apparatus as in chapter 3, the contributions of the accompanying radiations to the X-ray production and the background in measurement were evaluated. Fig. 13 shows the results of X-ray yields which include that for all the primary radiations (alphas, electrons, and gamma and X rays) and unfolded one for each component of radiations. The top curve without both the magnet and Mylar films shows the yield for the total primary radiations. The next curve with the magnet but without Mylar shows the yield for the radiations except the conversion electrons. Therefore, the difference of the two gives the yield for the conversion electrons.

The main energy of conversion electrons from ^{241}Am extend from 21 to 58 keV but the electrons of near 38 keV are the most in number[33]. Total rate of the electron emission is estimated at about 75 % per disintegration from the decay scheme[34] (if the Auger electrons are included, it increases somewhat). When taking into account a decrease in number of the electrons due to absorption by the source window and the source itself (25 $\sim$ 50 % transmission), the measured X-ray yield of Ti, for example, agrees roughly with the theoretical one using Eq. (2.7) for 38 keV electrons and also the previous experimental data of electron-excited X rays[35].

The contribution of the conversion electrons to the background in measurement can be seen in Fig. 14. When the magnetic field was set

against the beam of ^{241}Am radiations, the continuum background due to the electrons was eliminated, resulting in decrease of the background by a factor of about 10, while the net peak area changed little. It should be noted that, as is evident in these data, the contribution of the conversion electrons to the background is much larger than that of the other radiations, though the X-ray yields is considerably less than the sum yields for the other radiations.

Elimination of the background due to the conversion electrons can be made also by means of a film absorber instead of a magnetic field. Fig. 15 shows the background reduction by 4 sheets of 6 μm Mylar (ca. 3.6 mg/cm^2 in total) in the apparatus of Fig. 3 excepting the magnet. Mylar films of 3.6 mg/cm^2 can absorb electrons of energy lower than ca. 45 keV[36].

However, such a absorber reduces also the energy of alpha particles. The energy reduction in alpha particles results in remarkable decrease in X-ray production except the case of very low Z elements such as carbon. The X-ray yields with various thickness of Mylar film absorbers are shown in Fig. 16. The data with 6 sheets of Mylar (ca. 5.3 mg/cm^2 in total) means the yields for the gamma and X rays. It is clear that the thickness of absorber or source window can not be so thick to obtain the high peak to background ratio for aluminum for example, because the X-ray production by the gamma and X rays is very low for such a low Z element and the source of background except the conversion electrons is almost the gamma and X rays.

After all, to effectively utilize an alpha-ray source emitting rather high energy conversion electrons such as ^{241}Am for a low Z element such as aluminum, the use of a magnet is indispensable to exclude the electrons.

However, it is undesirable from the viewpoint of geometrical efficiency.

Other transuranium isotopes, ^{238}Pu, ^{242}Cm, and ^{244}Cm, which have lately become to be available, seem to be advantageous in this point, because the energies of conversion electrons are lower and the rate of the emission is smaller; the main energies are 24, 22, and 22 keV, respectively, the maximum energy equally 39 keV, and the emission rate 28, 26, 23 %, respectively[34]. These conversion electrons will be almost absorbed by a source window of 2 mg/cm^2 or smaller thickness.

4.1.2 Contribution of soft X rays in ^{210}Po

^{210}Po is the sole available isotope which is virtually regarded as a pure alpha emitter. The emission rate of gamma and X rays and conversion electrons are extremely low. Nevertheless, the background observed in characteristic X-ray measurements was found to be due to the accompanying X rays. Using a measuring chamber shown in Fig. 17 with a 10 mCi ^{210}Po alpha-ray source (the same type as the ^{241}Am source used, but the deposited disc was silver and the window was a mica foil of 1.2 mg/cm^2), the count of scattered rays was measured by setting a polyethylene target of 4 mm thickness as a scatterer at the sample position. The count in the Mg or Al KX-ray channel was about one hundredth of the KX-ray count of each pure element. And the scattered ray count was exponentially attenuated with Mylar films placed on the source by a rate whose attenuation coefficient was about 1800 cm^2/g. This is considered to be due to the characteristic X rays of Pb, especially M and NX rays, from ^{210}Po, which are excited by ejection of inner shell electrons from the electronic cortege of the nucleus in the act of alpha-decay in a manner described by Migdal's theory (the intensities of K, L, M, and NX rays become higher

in this order)[37]. In this connection, the Pb X rays caused by internal conversion of 803 keV gamma rays are considerably weaker than those described above. The ratio of Al KX rays to scattered rays also was decreased with an increase in Mylar thickness. These facts shows that the X rays from a sample are produced mainly by the alpha rays and the X-ray production by alpha rays is more rapidly decreased than the scattered rays by an increase in Mylar thickness.

It was revealed by recent studies[38)39)] that for pure alpha or proton bombardment a main background source in the low energy X-ray spectra is the bremsstrahlung from the secondary electrons produced in the target by the impinging ion. The production of secondary electrons is performed through the same process that produces the inner shell ionization followed by a characteristic X ray. Therefore, the ratio of the background to characteristic X-ray count must be almost equal to the cross section ratio. It comes to about one thousandth for the ratio of carbon background to aluminum X rays[38]. The value is smaller by one order of magnitude than the background ratio in the ^{210}Po source.

As a conclusion it can be said that in the use of alpha-emitting isotopes the largest source of the background in characteristic X-ray measurement for low Z elements is conversion electrons if they are emitted, and the next one is X rays or low energy gamma rays, and in comparison with these the bremsstrahlung background due to both alpha rays and their secondary electrons is considerably low (though the background due to the bremsstrahlung and nuclear excitation will be noticeable in the higher-energy region of alpha particles generated by an accelerator).

4.2 X- and Gamma-Ray Sources

4.2.1 Photon-excited X rays in ^{241}Am source

^{241}Am can be used as a gamma-ray source or an LX-ray source by changing the thickness of source window. Fractions of emergent gamma and X rays are shown in Table 1 for both a thin ideal source and the source used in the experiments of chapter 3. The thick target yields of KX rays produced by gamma and X rays from the latter source are discussed in the following. To eliminate alpha rays, 6 sheets of 6 μm Mylar films (ca. 5.3 mg/cm^2 in total) were used. Then, only the Np Mα X rays are significantly (by 42 %) attenuated by the absorber, while the other gamma and X rays are hardly influenced. The same experimental apparatus as in chapter 3 was used. The yields for pure elements were obtained in a similar manner as in chapter 3 :

$$Y_{exp} = \frac{N_{obs}}{3.7\times10^{7} A \left(\sum_j r_j\right) T\Omega_t\Omega_d \varepsilon_d} , \qquad (4.1)$$

where N_{obs} is the X-ray count observed with 6 sheets of Mylar, A is the measured radioactivity of the source (mCi), r_j is the fraction of the j-th gamma or X ray per disintegration in the source with Mylar films, and T is the counting time (sec). The other symbols Ω_t, Ω_d, and ε_d are the same as in Eq. (3.1). The results are shown in Fig. 18. The errors attached to the experimental values were obtained similarly as in the case of alpha-excited-X-ray yields, by assuming uncertainty of the denominator of Eq. (4.1) to be 10%.

The theoretical thick target yield for each photon component of the source was calculated by Eq. (4.2) derived from Eqs. (2.2) and (2.3).

$$Y_j = \frac{r_j}{4\pi \left(\sum_j r_j\right)} \frac{\mu_{rj}}{\mu_{1j} + \mu_2} \omega \left(1 - \frac{1}{J}\right), \qquad (4.2)$$

where

ω : the fluorescent yield,

J : the jump ratio of the photoelectric mass absorption coefficient at the absorption edge,

μ_{rj} : the photoelectric mass absorption coefficient of the pure element for the j-th gamma or X ray,

μ_{1j} : the total mass absorption coefficient of the pure element for the primary radiation (j-th gamma or X rays),

μ_2 : the total mass absorption coefficient of the pure element for the secondary radiation (KX rays of the element).

Curve lines in Fig. 18 are the calculated X-ray yields for respective photon components and the sum of them (total yield).

The curve of total yield fits well the experimental points within the quoted errors. Therefore, the assumption on the uncertainty mentioned above can be regarded as reasonable. The calculated X-ray yields for photon components reveals that the largest contribution is made by Np Lα and Np Lβ X rays in the energy range higher than 2.8 keV and by Np Mα rays in the range lower than 2.4 keV, while 59.6 keV gamma rays make little contribution in these range, though the photon fraction is the largest.

4.2.2 Utility of Np LX rays from ^{241}Am source

The practical utility of the LX rays from ^{241}Am to excitation of X rays of higher Z elements than titanium was examined[40] by using a commercially available ^{241}Am photon source. The source used is a modified

AMC6[41] made by RCC(Amersham). ^{241}Am of 100 mCi as oxide mixed with aluminum and pressed into a pellet is sealed in a stainless steel capsule of 10.8 mm dia. and 5 mm height, the window of which is aluminum of 0.125 mm thickness. The output intensities of the LX rays and 59.6 keV gamma rays are reduced to about 19 % and 61 % of a thin source, respectively, mainly due to self-absorption in the pellet[42]. (This source is called as a ^{241}Am LX-ray source in the following). The arrangement of source, sample, and detector shown in Fig. 19 was used for the experiments.

The observed pulse-height spectra of produced X rays and scattered gamma rays from thick samples of pure elements are shown in Fig. 20. The peak area count of Kα rays of each element is plotted against atomic number of element as the curve A in Fig. 21. The curve B in the same figure shows the peak area count obtained with the source covered by a nickel foil of 140 mg/cm^2 which absorbs entirely the ^{241}Am LX rays, therefore it means the intensity of X rays excited only by the gamma ray of 59.6 keV. The difference between the two curves indicates what is produced by the LX rays. For elements of $Z \leq 35$, the intensities of Kα rays excited by the LX rays (curve A minus curve B) are about 5 times larger than those by the gamma ray (curve B).

To estimate the magnitude of background of pulse-height distribution continuum due to matrix element other than an element to be analyzed in the X-ray spectroscopic analysis, the ratio of the continuum background by an interfering element to the Kα peak count in FWHM of the element of interest was taken for various element combinations and for the ^{241}Am source with and without nickel filter.

The results are shown in Table 4. The background per cent in analysis of an element of $Z \leq 35$ (such as Ti, Fe, and Zn) is decreased to 1/3 ∿ 1/5

by use of the LX rays compared with the case where the LX rays are not used, while for an element of Z > 35 (Mo) the background by the source without the LX rays is lower than that by the LX-ray source. The background for the ^{241}Am LX-ray source is 3 to 5 times as low as that for a ^{147}Pm beta-ray source[43], in the region of Z $\leq$ 35. Even in comparison with a ^{109}Cd X-ray source which emits Ag KX rays and is regarded as a nearly monochromatic X-ray source, the background caused by aluminum matrix for an element of Z $\leq$ 35 proved to be only 1.5 times higher. These background is due to the pulse-height distribution continuum produced in the detector by the scattered rays and the characteristic X rays of matrix element. (The pulse-height distribution characteristics in detectors will be discussed later. cf. 5.2). When the atomic number of matrix element is higher than that of the element to be measured, a large contribution to the background is caused by the pulse-height distribution continuum related with the KX-ray peak of matrix element (cf. Fig. 20).

To conclude, the use of the LX rays from ^{241}Am is very useful to excite KX rays of elements of the 4th period in the Mendeleieff table, particularly elements of Z = 26 $\sim$ 35. X-ray analysis with high count rate and low background is possible by using a proportional counter of argon containing methane. Whenever an atomic number of matrix element is low, even trace element analysis with high sensitivity would be possible. For elements of Z > 35, however, the source without the LX rays (i.e. gamma-ray source) is rather recommended, because scattering of the LX rays interferes with the measurement of fluorescent X rays.

Sealed sources of other transuranium nuclides with long half life, ^{238}Pu and ^{244}Cm, also have property similar to the ^{241}Am LX-ray source, since they emit U LX rays and Pu LX rays, respectively. Moreover, as

regards the background, these sources are more advantageous than the ^{241}Am LX-ray source, since they have no significant gamma -ray component.

4.2.3 Tritium X-ray sources

The so-called tritium targets, ^{3}H/Zr and ^{3}H/Ti, can be used as soft X-ray sources to excite KX rays of low Z elements. The X-ray excitation characteristics were examined[44], by using two sources of the following specifications (made by RCC, Amersham). The ^{3}H/Zr source contains tritium of 3 Ci incorporated in a thin layer of zirconium plated onto a tungsten disc of 12 mm dia. and 0.5 mm thickness, and emits, besides weak beta rays, Zr LX rays (Lα : 2.04 keV), W LX rays (Lα : 8.40 keV), and bremsstrahlung. The ^{3}H/Ti source contains tritium of 6 Ci incorporated in a thin layer of titanium plated onto the same disc as the above, and emits Ti KX rays (Kα : 4.51 keV) more strongly than bremsstrahlung. Measurement of KX-ray intensities of Mg (Z = 12) through Ni (Z = 28) was made with the measuring chamber shown in Fig. 17. The distance between sample and detector window was adjusted to 6 mm where the maximum intensity of excited X rays was obtained.

The observed total KX-ray counts for thick targets of pure elements are shown in Fig. 22. Here, powder briquette of ammonium salt for Cl, and oxides for Ca and Ti were used as samples, and KX-ray counts for the compounds were divided by weight fractions of objective elements to roughly obtain counts for the pure elements. A sheet of 0.95 mg/cm^{2} Mylar used absorbs the beta rays completely and the X-ray component of the lowest energy such as Zr LX rays in some degree. Fig. 22 shows that the difference between with and without Mylar, viz. the contribution of these weak radiations to X-ray excitation is very small in the region of $Z \geq 20$ but is not

so small in the lower Z region. The atmosphere of the measurement was helium at 1 atm. If a measurement were made in vacuum, somewhat higher count rate would be gained in particular for low Z elements. On the other hand, however, scattering of beta rays and soft X rays would be a problem in measurement in vacuum. In fact, as shown in Fig. 23, a tritium source with no absorber in vacuum caused a high background in the low energy region and a thin filter over the source was needed to reduce the background in application (cf. 7.1.1). Tritium sources with thin absorber can be recognized as a favorable source for excitation of X-rays of light elements (usually called for $Z \leq 22$) and somewhat higher Z elements.

5. Characteristics of X-Ray Detectors

In X-ray spectroscopic analysis using radioactive sources, the so-called non-dispersion analysis or the recently-called energy dispersive analysis is made instead of the crystal dispersion analysis on account of the comparatively lower intensity of primary radiations from sources, and for the sake of positive application of small size sources and simultaneous analysis of multielements.

Scintillation counters have been used in portable X-ray analyzers and industrial analyzers for analysis of a specific element in a sample, usually with the foil filter method such as a balanced filter, because of the high counting efficiency, the high count rate capability, and ease of the usage, though the energy resolution of detector itself is considerably low. For simultaneous analysis of multiple elements, however, X-ray detectors with better energy resolution are required. So, proportional counters and semiconductor detectors become an object of choice. Scintillation counters are ruled out also for measrement of low Z elements such as aluminum and silicon, because of their low-energy limitation due to thermal noise in the photomultiplier.

For use of the detectors in practical X-ray analysis, the stability of their characteristics comes into question besides the energy resolution, detection efficiency, etc. Inexpensiveness is also desirable property, as far as the performance is not lowered. In analysis for trace amounts of elements, the continuum background in pulse-height distribution due to X rays (or gamma rays) of higher energy than those of the element to be measured is desired to be as low as possible.

In this chapter, operating characteristics concerning the usage and

the construction are examined for proportional counters, and pulse-height distribution characteristics relating to the continuum background are discussed for both proportional counters and semiconductor detectors.

5.1 Operating Characteristics of Proportional Counters

The examinations of various kinds of counter characteristics described in this section were made by measuring Mn KX rays from a ^{55}Fe source with one of the following gas flow counters. The pulse height distributions were observed by automatically scanning the level of window in a single-channel pulse-height analyzer.

Counter A : the inner diameter of the cathode tube made by brass is 30 mm and the length 100 mm (inside surface plated with gold); the diameter of the tungsten center wire is 0.03 mm; the aperture of the Mylar window 17 mm × 13 mm, the thickness 6 μm. (this counter is the same as in Fig.17).

Counter B : the inner diameter of the aluminum cathode tube is 45 mm and the length 400 mm; the diameter of the tungsten center wire 0.1 mm; the Mylar window 35 mm × 25 mm, the thickness 6 μm.

Counter C : the inner diameter of the brass cathode tube is 35 mm and the length 300 mm; the diameter of the tungsten center wire 0.05 mm; the Mylar window 30 mm × 20 mm, the thickness 6 μm. (this counter was fabricated for use in a practical analyzer, cf. 7.1.2.)

The windows of all the counters are situated at the middle of the counter tubes.

5.1.1 Counting gases

A gas mixture of 90% argon and 10% methane is most easily available as a counting gas in the proportional region of radiation counters (PR gas or P-10 gas). Also an argon containing carbon dioxide of several per cent is used. The use of argon as the main component in counting gas is considered to be suitable for measurement of soft X rays of low Z elements on account of high detection efficiency for the X rays and low

efficiency for higher energy X (or gamma) rays.

Fig. 24 shows the experimental results[45] of gas gain and resolution for both Ar-CH_4 and Ar-CO_2 mixtures of various ratios at atmospheric pressure. Measurements were made using the counter A. The resolution in Ar-CO_2 was apparently worse than that in Ar-CH_4, though the gas gain was nearly equal between the two gas mixtures in the same ratio. The minimum in resolution was obtained at 5 ∿ 15 % of CH_4 mixing. Ar-CH_4 mixtures were superior to Ar-CO_2 not only in the minimum value in resolution but also in ranges of both the gas mixing ratio and the applied voltage where the resolution is kept in good values. Increase in CH_4 mixing ratio causes decrease in both the gas gain and the detection efficiency. So, the CH_4 mixing of about 10 % is considered most appropriate for measurement of soft X rays.

The deterioration in resolution arises generally at both too low and too high applied voltage, since the recombination of electrons of primary ionization will remarkably increase near the cathode at too low voltage and the space charge effect in the vicinity of the anode wire will occur at too high voltage (in high gas gain) (cf. 5.1.6). However, the steep rise in the resolution curves (deterioration) against applied voltage, seen in low mixing ratios of CH_4 and in most of CO_2 mixtures in Fig. 24, does not seem to be due to such effects. Because the applied voltage is not so low and the gas gain is not so high (compare the cases of 10 % CH_4 and 10 % CO_2, for example). The deterioration is presumably caused by lack of the quenching action in proportional counter.

Even the minimum value of resolution in Fig. 24 is somewhat larger than the best value expected in proportional counters (semiempirically 16.5 % at 5.9 keV). The reason is probably the unevenness in diameter of the

center wire.

5.1.2 Effects of impurity gases

A specification of constituents in commercially available PR gas is Ar 90 %, CH_4 10 % (±1 %), and as impurities N_2 0.07 %, O_2 0.005 %, CO_2 0.005 %, and H_2O further less. To find permissible levels of the impurity gases, measurements were made with the counter A, adding a small amount of high purity N_2, O_2, CO_2, and C_3H_8 separately to the PR gas. The results are shown in Fig. 25[45].

The maximum permissible levels of N_2, O_2, and CO_2, to restrain decrease in gas gain within 10 % (nearly equivalent to the variation due to 1 % error in CH_4 mixing), were 0.37 %, 0.45 %, and 1.0 %, respectively. Addition of a small amount of N_2, CO_2, and C_3H_8 did not cause any significant change in resolution. However, the addition of O_2 by 0.45 % caused a 3.3 % change in resolution. Since any change in resolution cannot be compensated by measuring circuits as in gain variation, the change may have to be checked more severely. If a limit of resolution change is set at 1 %, the maximum permissible level of O_2 becomes about 0.2 %. It is to be noted that these permissible levels are considerably higher than the impurity concentrations in the PR gas described above.

5.1.3 Effects of gas flow-rate

When the flow rate of PR gas was varied in the counter A placed in the air atmosphere, the considerable variation in pulse height was observed as shown in Fig. 26 (curve A)[45]. This is considered to be due to diffusion of air into the counting gas through the Mylar window or the other parts (an end of the counter has a small opening for holding the center wire).

The counter C was employed in vacuum. The counter has the airtight structure at both ends of the tube, and the window of 6 μm Mylar is protected by tungsten wires of 0.1 mm diameter stretched at 3 mm intervals. In advance to experiments, a 2 atm. pressurized gas was poured into the counter immersed in water, to inspect pin holes in the window and also leaks at the connecting parts in the gas-flowing pipes. The results of pulse-height variation of the counter in the atmosphere and in vacuum, against the flow-rate of PR gas, are shown in Fig. 26. The flow-rate dependence of gas gain in the counter C is obviously less than that in the counter A. This indicates the importance of air-tightness in flow counters. The negative gas pressure dependence of the counter C in vacuum is considered to be due to the pressure increase along with the flow-rate on account of flow resistance at outlet.

No significant change in resolution, however, was found in all the cases. This may be of course because of smallness of the amount of O_2 diffusion.

5.1.4 Effects of gas temperature and pressure

An increase in counting-gas density due to change in gas temperature or pressure causes a decrease in gas gain in a proportional counter. The relative pulse-height increase in the counter B with PR gas (operated at 2400 V) was about 8.5 % per 1 % increase of temperature of the atmosphere (absolute temperature)[45]. Since the temperature dependence of gain in the electronic circuits used was slight, the observed value was considered to be almost due to the gain change in the counter.

Campbell[46] derived theoretically the relationship between the mean gas gain, the applied-voltage dependence, and the temperature dependence:

$$\ln \bar{A} = \frac{V}{\bar{P}} \frac{\partial \bar{P}}{\partial V} - \frac{T}{\bar{P}} \frac{\partial \bar{P}}{\partial T} , \tag{5.1}$$

where $\bar{A}$ is the mean gas gain, V the applied voltage, $\bar{P}$ the mean output pulse height, and T the absolute temperature. From the experimental data on voltage dependence of pulse height in Fig. 24, an approximation equation can be obtained at a fixed temperature and pressure:

$$\ln \bar{P} = a + bV , \tag{5.2}$$

where a and b are constants. $\bar{A}$ is of course proportional to $\bar{P}$. Then, from Eqs. (5.1) and (5.2), Eq. (5.3) is derived.

$$\frac{\partial}{\partial V} \left(\frac{T}{\bar{P}} \frac{\partial \bar{P}}{\partial T} \right) = 0 . \tag{5.3}$$

This shows that the temperature dependence of pulse height is almost constant against the applied voltage. Strictly speaking, however, $\ln \bar{P}$ appears to be a function which is convex downwards (cf. Fig. 24); then $\frac{\partial}{\partial V} \left(\frac{T}{\bar{P}} \frac{\partial \bar{P}}{\partial T} \right)$ has a small positive value. Therefore, the relative temperature dependence of gas gain may slightly increase with the applied voltage.

Incidentally, putting both the values of $\frac{T}{\bar{P}} \frac{\partial \bar{P}}{\partial T} = 8.5$ described above and $\frac{V}{\bar{P}} \frac{\partial \bar{P}}{\partial V} = 17.6$ previously measured into Eq. (5.1), the mean gas gain of the counter B at 2400 V is obtained as 8.9×10^3.

The above temperature coefficient of 8.5 is nearly equal to the data 8.7[46] which was measured by Campbell in a counter of argon containing 2.5 % carbon dioxide. The coefficient of pressure dependence must have the equal value but opposite sign to the temperature coefficient, because the change in gas gain is caused by change in gas density. In practice, the values are too large to measure characteristic X rays in the spectroscopic analysis. When the temperature and pressure of counting gas are not held

constant at definite values, electronical control of the overall gain may be required in a measuring system including the detector, amplifier, and high-voltage power supply.

A change in counting-gas density causes a change in detection efficiency also. When the detection efficiency without window absorption is 0.5, the relative change in the efficiency due to 1 % density change becomes about 0.7 %. The higher the efficiency, the less the efficiency change. As the detection efficiency without window absorption is near unity for X rays of low Z elements, the efficiency change scarecely becomes a problem for most cases using a proper size counter.

5.1.5 Effects of counter length

To avoid effects of the distortion in electric fields at both ends of the counter, field adjusting electrodes or long size counters have often been used. Some experiments[45] were made to know the practical necessary length in a proportional counter, by inserting two insulator discs with a center hole of 5 mm dia. into the counter B and changing the distance between two discs. A ^{55}Fe source was placed at a distance of 3 mm above the counter window.

As a result, no change was observed in pulse-height distributions until the distance between two discs was reduced to 150 mm. At 100 mm, the pulse-height decrease was about 10 %, while no appreciable change in the resolution was observed. When the distance was shortened to 40 mm, the pulse height decreased rapidly exponentially with the lapse of time, reaching equilibrium at the half value after 40 min, and the resolution deteriorated from 20 % to 30 %. These are considered to be due to the accumulation of electric charge on the surface of the insulator discs.

In similar experiments using the two insulator discs covered with aluminum foil having a center hole of 10 mm dia., on the contrary, the pulse height increased by 10 % at the distance of 100 mm (no appreciable change in the resolution). This is considered to be due to effect of the intensified electric fields at both ends of the center wire. Also in this case, no change in the pulse-height distribution was observed for the distance larger than 150 mm.

After all, the length of 150 mm is judged as the necessary and sufficient for the soft X-ray proportional counter, when a source of radiations is located just above the counter window. In this connection, the absorption of Mn KX ray by a PR gas of thickness 75 mm is about 98 %.

5.1.6 Effects of high gas gain and high count rate

The non-proportionality of pulse height to energy of an entering radiation at a high gas-gain has been early recognized and considered to be probably associated with space charge within an avalanche which reduces the effective field at the anode wire[47]. Later, there have been several reports of count-rate dependent shifts of pulse-height distributions[48)49)]. Spielberg[49)] has reported that the shift obtained with a stainless steel anode wire is much larger than that with a tungsten wire of the same diameter (50 μm) in the counter operated at a gas gain of 2.2×10^3 with a PR gas detecting 1.78 keV X rays, and that at least part of the shift appears to be due to absorbed gases, perhaps debris from counter avalanches, on the wire surface, which are momentarily released during the electron collection process, and are subsequently capable of capturing electrons during succeeding avalanches, thereby reducing the average pulse height.

The relationship between the pulse height shift and the gas gain or

the count rate was examined quantitatively by using the counter A (the center wire was replaced by 50 μm dia. tungsten) with a 1 atm. PR gas. Mn KX rays were detected at various count rates by the counter, the output of which was, through a cathode follower and an amplifier (Kobe Kogyo LA-2) with rise time 0.8 μs, fed to a single channel analyzer. The results are shown in Figs. 27 and 28. The latter is obtained from the former by calculating the number of total ion pairs per second (from the count rate, the number of primary ionization per radiation, and the gas gain). From Fig. 28, the pulse-height shift is proved to depend on the rate of production of total electric charge. From Fig. 27, to restrain the pulse-height shift within 2 % at the count rate of 1000 cps for example, the gas gain has to be less than about 5000. If the energy of radiation comes to the half, the limit will be raised up to twice (the count rate 2000 cps or the gas gain 10,000).

The deterioration in the energy resolution also must be caused by the same process. However, observation was not made, as the change in the resolution was comparatively small to detect accurately.

5.2 Characteristics of Pulse-Height Distribution in proportional Counters

5.2.1 Experimental equipment

The pulse-height distribution of a proportional counter for a monochromatic X or gamma ray consists of a full energy peak (totally absorbed peak or simply called as photo-peak) and an energy degraded part which extends widely at the lower energy side of the full energy peak, as is seen for instance in Fig. 20. The latter, as a background, often interferes with small peaks of lower energy X rays. So, such a degraded pulse-height distribution is desired to be as low as possible.

To clarify the characteristics of the degraded pulse height distribution, a series of experiments was made using a proportional counter placed in a pressurizing vessel whose inside gas pressure can be changed from vacuum to up to 10 atm. A 1 mCi ^{109}Cd (22.2 keV, Ag KX) and a 100 mCi ^{241}Am (59.6 keV, γ) were used as sources of nearly monochromatic and rather high energy X- or gamma-ray for simplicity of data analysis. The arrangement of source, collimator, and counter is shown in Fig. 29. The nickel foil and the aluminum plate were used for elimination of lower energy X and gamma rays from ^{241}Am source.

5.2.2 Emission of secondary electrons

The observed pulse-height responses of the counter at various pressure of a PR gas are shown in Fig. 30. The fraction of photo-peak clearly decreased with decreasing gas pressure. This is considered to be due to increase in escape of photo-electrons from the gas region to the outside (namely cathode cylinder). A total count of all pulses produced by absorption of the primary radiation in the counting gas must be almost proportional to gas pressure (in all range for ^{241}Am, and at low pressure for ^{109}Cd), for smallness of a fraction of the absorption. The observed total count (corrected for lack of data near zero channel), however, deviated from the proportionality considerably to plus side. This is undoubtedly due to secondary electrons generated by interaction of the primary radiation with the collimator or the filter and the cathod cylinder. The emission of secondary electrons must be almost independent of gas pressure, because the attenuation of the primary radiation in the gas is small. Then, the net total count due to interaction between the primary radiation and the counting gas was obtained by subtracting a constant count from the

observed total count, so as to get the proportionality of the total count against the gas pressure (in all range for ^{241}Am, and at low pressure for ^{109}Cd). The ratio of the constant to the primary radiation intensity was 0.76×10^{-3} for 59.6 keV (^{241}Am) and 3.6×10^{-3} for 22.2 keV (^{109}Cd). Theoretically, the probability of secondary electron emission from the surface of cathode etc. to the counting gas region can be roughly calculated by

$$P_{S.E.} = \left(\mu_\tau + \frac{1}{4} \mu_s \right) R \quad , \tag{5.4}$$

where μ_τ and μ_s are the mass absorption coefficients of photoelectric effect and scattering for the cathod material, respectively, and R is the electron range in the same material (g/cm^2). The calculation for aluminum agrees fairly well with the above value : 0.70×10^{-3} for 59.6 keV (^{241}Am) and 2.1×10^{-3} for 22.2 keV (^{109}Cd).

5.2.3 Escape of photoelectrons

The fraction of photoelectron escape including fluorescent X-ray escape was obtained by

$$f_{e,exp} = \frac{N_T \mu_\tau / (\mu_\tau + \mu_c) - N_P}{N_T \mu_\tau / (\mu_\tau + \mu_c)} \quad , \tag{5.5}$$

where N_T is the corrected total count described above, N_P is the observed full-energy-peak total count, and μ_τ and μ_c are the photoelectric and Compton mass absorption coefficients of the counting gas, respectively. The results are shown in Fig. 31. The straight lines drawn as inversely proportional to gas pressure seem to fit well the experimental data. Assuming that the generation of photoelectrons is uniform along the passage of the primary radiation and the diffusion of the electrons is isotropic,

the fraction of electron escape may be roughly theoretically estimated by

$$f_{e,\,theor} = \frac{kR}{\rho t} = \frac{kR}{\rho_0 t}\,\frac{P_0}{P}\,\frac{T}{T_0}\,, \tag{5.6}$$

where k is the proportional constant, and R, ρ, t, P, and T are the electron range (g/cm^2), the density, the thickness, the pressure, and the absolute temperature, respectively, in the counting gas; suffix 0 means the standard temperature and pressure of the gas.

The proportional constant k means what fraction of electrons diffused outwards is lost from the depth R under the detector surface. If the fraction of escape in Fig. 31 is assumed to consist of electron escape only, the value of k becomes about 0.6. It seems to be reasonable when taking into account that photoelectrons are ejected from gas molecules in directions perpendicular to the beam of the primary radiation but they are diffused isotropically. And the escape of the fluorescent X rays is considered to be insignificant, since the pulse-height distribution due to the fluorescent X-ray escape must concentrate around a position of the photopeak energy minus the fluorescent X-ray energy.

5.2.4 Discussion

In comparison with photoelectric processes as discribed above, multiple processes for Compton-scattered rays may be almost negligible, since the probability of the single process is far less than that of photoelectron escape etc. After all, the degraded pulse-height distribution except the portion of Compton electrons is attributed to both the photoelectron escape from the gas and the secondary electron emission from outside of the gas. The relative value of the secondary electron count to the theoretical photopeak count without escape was comparable with the

value of photoelectron escape fraction at any pressure for both 59.6 keV and 22.2 keV photons. If a higher Z material is used for the cathode, only the former will increase. When energy of the primary radiation is lowered, the fraction of photoelectron escape must decrease proportionally with electron range while the contribution of secondary electrons may not so much decrease or rather increase (for energy lower than 10 keV) with decreasing electron range because the photoelectric absorption coefficient increases. However, when a low Z material such as Mylar or beryllium is used at the part of the counter window, the emission of secondary electrons is surely reduced.

5.3 Characteristics of Pulse-Height Distribution in Semiconductor Detectors

5.3.1 Evaluation of the valley background

The effective thickness of recent semiconductor detectors for low energy photons, Si(Li) and Ge(Li), are usually larger than 2 mm; that is, far larger in the value of ρt than that in proportional counters. Then, foe example, using Eq. (5.6), the photoelectron escape fraction must be less than 0.8 % and 0.1 % for 59.6 keV and 22.2 keV photons, respectively, for silicon detectors. The fluorescent X-ray escape is distinguishable from the electron escape because of the good energy resolution. The secondary electron emission from a thin layer of the insensitive silicon also may be small in relative value to the full energy peak count. Therefore, unless other origins cause degradation of pulse height, a very low background in detectors must be expected.

Fig. 32 shows the pulse height responses of a Si(Li) detector for the collimated 59.6 keV gamma ray from a 100 mCi ^{241}Am source with 0.3 mm brass and 0.5 mm Al absorbers. The solid line is the response for the

beam with collimation to the center part of the detector and the broken line is that to the edge part of the sensitive area. Compton scattered rays may be produced not only inside the detector but also outside the detector (source itself and surroundings). The peaks of lower energy gamma rays are originated from ^{241}Am itself.

Assuming that the valley background is continuing from zero energy to the full energy at a horizontally constant level (except the components of Compton electrons, Compton scattered rays, and small gamma ray peaks), the ratio of the valley background to the full energy peak count was calculated for evaluation of the valley level:

$$r_B = i_B(E_1) \cdot E_2 / i_P(E_2) \qquad (5.7)$$

where $i_B(E_1)$ is the intrinsic efficiency of valley background generation per unit energy interval at energy E_1, and i_P is the intrinsic photo-peak efficiency at energy E_2. Here, E_2 means the energy of the primary radiation, and E_1 is adopted as a representative point of the valley. For convenience, the value of E_1 was taken on $0.6\,E_2$ (cf. Fig. 32, and it is used also in the figure of merit described later; cf. 5.4.1). The adopted energy is near the minimum point of the valley.

Experimental results of several semiconductor detectors are shown in Table 5. Data with collimation were obtained using a lead collimator having a hole of diameter 1 mm and length 10 mm, and the 100 mCi ^{241}Am source with an absorber of 0.3 mm thick brass plus 0.5 mm thick Al. The collimation was made to the center of each detector. The background due to the higher energy gamma rays from impurity nuclides in ^{241}Am was measured separately with a second absorber composed of lead (1 mm), brass (0.3 mm) and aluminum (0.5 mm), and it was subtracted from the

response without the second absorber (this subtraction was necessary for Ge(Li) detectors). Data without collimation were obtained using a 10 μCi ^{241}Am source (IAEA standard gamma-ray source).

5.3.2 Origin of the valley background

In Table 5, the values of r_B with collimation are always smaller than those without it. However, the values are still much larger than those which are expected from the photoelectron escape and the secondary electron emission. The contribution of multiple Compton scattering is also considered to be not so large. The source of this high valley background may be something inherent in semiconductor detectors. Goulding and Jaklevic[50)51)] have found the existense of similar high background in top-hat type Si(Li) detectors and have explained it by charge collection loss due to the surface potential distribution. And they have shown that the detector background could be remarkably reduced by a guard-ring structure and the anti-coincidence method. Further study may be required to know if the source of the background is the same as explained by Goulding and Jaklevic in other types of semiconductor detectors.

As seen in Fig. 32 (spectrum of broken line), when the collimation was directed to an edge part of the sensitive area of Si(Li) detector, the photo-peak count decreased to about half the value, but the valley background changed little. When the collimation was shifted still more outside the edge of sensitive area, the photo-peak count decreased rapidly but the valley background decreased slowly (no appreciable change in the energy resolution was observed). From the experiments, it is evident that the surrounding outside of the sensitive area is a source of the valley background. Here, the diffusion of charge carriers generated from the

insensitive region into the sensitive region may play an important role because the diffusion length is much larger than the electron range; about 1 mm in good silicon or germanium. The output pulses due to the carrier diffusion must be slower in rise time than the normal pulses, so that they may be distinguished by the difference of pulse shape. At any rate, the background produced from the surroundings of the sensitive region is the reason why data without collimation in Table 5 are larger than those with collimation.

5.4 Comparison of Figure of Merits of Proportional Counters and Semiconductor Detectors

5.4.1 Figure of merit of detectors

The concentration (or mass) of the element to be determined in X-ray analysis is obtained from the net peak count of the X rays (the peak total count minus the underlying background continuum). In the case where the background count is much larger than unity, the detection limit of the concentration (or mass), W_D, according to Currie[52], is expressed as

$$W_D \simeq 2k\,\sigma_0/A, \tag{5.8}$$

where σ_0 is the standard deviation of the net peak count when the net peak is negligibly small, k is a constant of the probability distribution corresponding to a certain value of risk, and A is the net peak count per unit concentration (or mass) of the element (namely, calibration coefficient or sensitivity factor). The value of σ_0 is generally proportional to the square root of the background count, $\sqrt{B}$ (approximately in most cases).

In order to lower the detection limit, it is necessary to increase the ratio $A/\sqrt{B}$. For detectors, A is the intrinsic peak efficiency at energy E_1 of the X rays, $i_p(E_1)$, multiplied by the geometrical efficiency, θ ; B is the product of the intrinsic efficiency of background per unit energy interval at energy E_1, $i_B(E_1)$, the width used for background estimation, $\Gamma(E_1)$, and the geometrical efficiency, θ. Then, the figure of merit (FOM) for detector is derived as

$$FOM(E_1) = \frac{A}{\sqrt{B}} = \sqrt{\frac{\theta \cdot i_p^2(E_1)}{\Gamma(E_1) \cdot i_B(E_1)}} \quad , \tag{5.9}$$

which is the same form as Cooper's[53].

In the actual X-ray analysis, the chief background originates in the scattered rays from the sample. And the largest value of the ratio $A/\sqrt{B}$ may be obtained at the point where the lower energy side tail of the broad scattered-ray peak almost disappears, as the efficiency of X-ray excitation decreases with energy of the X ray (in the case of excitation by mono-energetic photons). In the comparison of the FOM, supposing the second X ray (or gamma ray) of energy E_2 instead of the scattered ray, the valley count produced by the second X ray at energy $E_1 = 0.6\,E_2$ is taken for calculation of $i_B(E_1)$. Then, $FOM(E_1)$ means the detector figure of merit for the detection of the first X ray in the presence of the second X ray. For convenience, the width of FWHM (full width at half maximum) is taken as the value of $\Gamma(E_1)$. The geometrical efficiency, θ, is asymptotically proportional to the sensitive area of detector, S, when the distance between detector and source of X rays is sufficiently large. Using S instead of θ, the modified FOM becomes

$$FOM(E_1) = \sqrt{\frac{S}{\Gamma(E_1)} \cdot i_p(E) \cdot \frac{i_p(E_1)}{i_B(E_1)}} \quad . \tag{5.10}$$

In Eq. (5.10), it should be noted that the ratio of detector area to resolution is important if the intrinsic efficiencies of peak and background remain constant.

5.4.2 Comparison of figure of merits

Using ^{241}Am (59.6 keV) and ^{109}Cd (22.2 keV) as sources of the second X ray of energy E_2, the valley background of these sources was observed for several semiconductor detectors and proportional counters. The experimental procedure for the ^{241}Am sources (100 mCi and 10 μCi) was already described (cf. 5.3.1). The same data as used in Table 5 are utilized here again. For the ^{109}Cd source (1 mCi), an absorber of nickel (150 mg/cm^2) plus aluminum (0.5 mm) was used to estimate the background due to the higher energy gamma rays (mainly 88.2 keV), in the same manner as in the ^{241}Am source. The collimator used for ^{109}Cd was a brass one shown in Fig. 29. The data of the proportional counter in 5.2 also are used for evaluation of FOM.

Present interest is mainly in the general comparison between different kinds of detectors and in the evaluation of the detector background but not in the FOM value of individual measuring system, so the theoretical value of detector resolution in the present-state-of-the-art is adopted for $\Gamma(E_1)$, and the value of $i_p(E_1)$ is theoretically calculated by Eq. (5.11).

$$i_p(E_1) = (1 - f_e) \frac{\mu_\tau}{\mu_\tau + \mu_c} [1 - \exp\{-(\mu_\tau + \mu_c)\rho t\}], \quad (5.11)$$

where f_e is the theoretical photoelectron escape fraction (cf. 5.3.1). For the same reason, the FOM of Eq. (5.10) is calculated by taking S on unity. The results are shown in Table 6.

Of the FOM's for E_1 = 36 keV in Table 6, those of Ge(Li) detectors with collimation (No.5 and 6) are remarkably large [3 to 4 times the FOM's in Si(Li)]. It is seen from Table 6 that the main cause is the high peak efficiency in Ge(Li) (the valley background efficiency is not low compared with that in Si(Li) detectors). Without collimation, however, the FOM's in Ge(Li) are not so large on account of the high background. Although the actual energy resolution in Ge(Li) detectors used is worse than the value in Table 6 because of large size, the present discussion is made by using the semitheoretical resolution for the reason described already.

In measurement of low energy X rays with a Ge(Li) detector, the escape peak resulting from escape of Ge KX rays interferes occasionally with a peak to be measured. It is for this reason that the FOM calculation of Ge(Li) detectors was unsuccessful for the ^{109}Cd source.

The reason why the FOM of the Ar(CH_4) proportional counter (No.7) is extremely small for E_1 = 36 keV is evidently the very low peak efficiency. For E_1 = 13 keV, the value of peak to background efficiency-ratio in the Ar(CH_4) proportional counter is nearly equal or larger than that in Si(Li). However, the FOM is still smaller than that of Si(Li) because of the lower peak efficiency and the lower resolution. In the counter with the same counting gas of higher pressure (cf. Fig. 33), the FOM becomes almost equal to that of the Xe(CH_4) proportional counter. And these FOM's are about half that of Si(Li). The window area of proportional counters is usually 5 to 10 cm^2 while the sensitive area of high resolution Si(Li) detectors is less than 1 cm^2. Therefore, in the overall FOM which includes the window area, the value of a proportional counter becomes larger than that of a small Si(Li) detector, for the low energy X rays.

6. Quantitative Analysis by X-Ray Spectroscopy

Generally, the count of characteristic X rays of an element to be analyzed depends on not only the quantity of the element but also of the matrix elements. So, the dealing of the matrix effect is the main problem in the quantitative analysis. Such circumstances are the same in the energy dispersive analysis as in the wavelength dispersive analysis. Of course, however, advantageous analysis may be performed by the different techniques for different cases.

Methods of the calibration including the correction of matrix effect are given, in this chapter, in two typical cases of the energy dispersive analysis. One is the analysis of thin specimens in which the matrix correction is of second importance and the standardization technique for calibration is a problem. A simple semitheoretical method of calibration is thus proposed. The method will be advantageously applicable to multi-element analysis with a semiconductor detector. The other case is the analysis of sufficiently thick specimens, for which approximation formulae to treat the matrix effect are derived in general form. These two cases deal with gamma- or X-ray excited X rays for simplicity of theoretical formulae. However, in particular, the approximation formulae for thick specimens must be applicable also to alpha-excited X rays (For beta-excited X rays, the same formulae as those in gamma- or X-ray excited X rays can usually be used, as mentioned already. cf. 2.2).

Problems of accuracy, precision, and detection limit are discussed in relation of the above calibration methods.

6.1 Calibration in Thin Specimen Analysis

6.1.1 Proposal of new method

In the analysis for a specimen considerably thinner than the saturation thickness excited by gamma or X rays, the relationship between the count rate of the fluorescent X rays of an element of interest (element i) and the amount of the element is comparatively simple, and the determination of multielements can be made semitheoretically by the simple proposed method of calibration[54] without troublesome preparation of any thin specimen standard (preparation of thin specimen standards of satisfactory quality is difficult, because it must be uniform in thickness and the absolute mass quantity of the element per unit area must be known).

The count rate of the X rays of element i is expressed by modifying Eq. (2.2):

$$I_i(m_i) = k_i m_i C_i,$$

$$C_i = \frac{1 - \exp\left[-\sum_j \mu^i(j) m_j\right]}{\sum_j \mu^i(j) m_j} \qquad (6.1)$$

where k_i is the i-dependent constant including the source intensity, the geometrical factor, the cross section of the fluorescent X-ray generation, and the detection efficienty; m_i is the mass thickness of the element (g/cm^2). The last factor C_i is correction for the matrix absorption. The effective total mass absorption coefficient of an element j in a multi-element specimen, $\mu^i(j)$, for both the primary radiation and the fluorescent X ray of the element i, is expressed as

$$\mu^i(j) = \mu_1(j)\operatorname{cosec}\phi + \mu_2^i(j)\operatorname{cosec}\phi_2, \qquad (6.2)$$

where suffix i represents the characteristic X rays of the element i; $\mu_1(j)$ and $\mu_2^i(j)$ are the total mass absorption coefficients (cm^2/g) of an element j for the primary and the secondary radiations, respectively; ϕ_1 and ϕ_2 are the angles of primary and secondary radiations with respect to the specimen surface. Here, the matrix enhancement effect is neglected because it is small, compared with the matrix absorption effect.

For a sufficientry thick specimen of the pure element, the fluorescent X-ray count rate in Eq. (6.1) becomes

$$I_i(\infty) = k_i/\mu^i(i) \ . \tag{6.3}$$

Combining Eqs. (6.1) and (6.3), m_i can thus be determined by Eq. (6.4).

$$m_i = \frac{I_i(m_i)}{I_i(\infty)} \ \frac{1}{\mu^i(i)} \ \frac{1}{C_i} \tag{6.4}$$

This equation shows the principle of the proposed method.

Measurement of the saturation X-ray count rate, $I_i(\infty)$, with a thick target of pure element provides the basis for quantitative determinations. It is not necessary, however, to measure the value by experiment for each element for analysis. Since $I_i(\infty)$ is a monotonous function of the atomic number or the fluorescent X-ray energy, the value for an arbitrary element can be obtained by interpolation of the several pure elements. This technique can not be applied, however, when a thick target specimen of pure element is not available (for instance, rare-earth elements). $I_i(\infty)$ can be also obtained by theoretical calculation from that of another element, because $\mu^i(i)$ in Eq. (6.3) is determined as described below and the unknown factor (the product of source intensity and geometrical factor) in k_i is given by measurement of a single-element thick target

using the X-ray generation cross section, etc. Needless to say, the procedure of measurement and interpolation described first is both simpler and desirable, as long as it can be applied.

Another important factor in the determination with Eq. (6.4) is the effective total mass absorption coefficient in the pure element specimen (i=j), $\mu^i(i)$. The values of $\mu_1(i)$ and $\mu_2^i(i)$ in Eq. (6.2) are known from a table of mass absorption coefficients. The effective values of cosec ϕ_1 and cosecϕ_2 are experimentally obtained as follows. Using foil of known thicknesses for two elements and thick targets of the same elements, whose atomic numbers are somewhat separate from each other, their $\mu^i(i)$'s are first determined by Eq. (6.5) which is derived from Eqs. (6.1) and (6.3).

$$\mu^i(i) = \frac{1}{m_i} \ln \frac{I_i(\infty)}{I_i(\infty) - I_i(m_i)} \quad . \tag{6.5}$$

Then, from the two values of $\mu^i(i)$ obtained and the total mass absorption coefficients in a table, cosecϕ_1 and cosecϕ_2 are derived by solving the simultaneous equations composed of two Eq. (6.2)'s.

6.1.2 Matrix absorption correction

The correction factor for matrix absorption, C_i, can be taken as unity if the specimen is sufficiently thin. When thick, the quantity $\exp(-\sum_j \mu^i(j)m_j)$ in C_i (cf. Eq. (6.1)) is determined by measuring the relative intensity of the X-rays of a pure target of element i with and without the specimen in front of the target (this technique is the same as Giauque and Jaklevic's[55]).

Measurement of the matrix absorption is not necessary for each element for analysis. The amount of absorption can be calculated from

one element to another[56], because the total mass absorption coefficient of X rays is simply dependent on the X ray energy. For instance,

$$\mu_2^i(j) = \mu_1(j)\, f_i \,, \qquad (6.6)$$

$$f_i = (E_1/E_i)^n \,,$$

where E_1 and E_i are the energies of primary radiation and characteristic X ray of element i, respectively; n becomes 2.80[57], if E_1 and E_i are both larger than the K absorption edge of element j or both lie between the K and L absorption edges of element j. Therefore,

$$\sum_j \mu^k(j)\, m_j = \frac{\mathrm{cosec}\phi_1 + f_k \mathrm{cosec}\phi_2}{\mathrm{cosec}\phi_1 + f_i \mathrm{cosec}\phi_2} \sum_j \mu^i(j)\, m_j \,. \qquad (6.7)$$

As usually f_k and $f_i \geq 1$, and cosec ϕ_1 and cosec $\phi_2 \simeq 1$, Eq. (6.7) takes a value of near f_k/f_i.

Substituting the values of $I_i(\infty)$, $\mu^i(i)$, and C_i thus obtained into Eq. (6.4), the fluorescent X-ray count rate is converted to the quantity of the element per unit area in the specimen.

6.2 Calibration in Thick Specimen Analysis

6.2.1 Derivation of basic formulae with Taylor expansion

In the analysis of a thick specimen (thicker than saturation thickness), the accurate determination of an element is generally not easy because the correction for matrix components is not made experimentally. General formulae of calibration including matrix correction are derived in the following, in the case of gamma- or X-ray excited X rays.

The count rate of the X rays of the element i is given from Eq. (6.3):

$$\left.\begin{aligned} I_i &= k_i W_i/\mu^i \ , \\ \mu^i &= \sum_j \mu^i(j) W_j, \quad \sum_j W_j = 1, \quad (j \text{ includes } i) \end{aligned}\right\} \tag{6.8}$$

where W_i and W_j are the weight fractions of element i and j in a specimen, k_i and $\mu^i(j)$ are the same as in thin specimens, respectively (cf. 6.1.1). The matrix enhancement effect is neglected as in the previous section.

Executing the Taylor expansion of Eq. (6.8) at W_{jo},

$$I_i = I_{io} + \frac{k_i}{\mu^i_o}\{ \triangle W_i + W_{io} \sum_j \frac{-\mu^i(j)}{\mu^i_o} \triangle W_j \}$$

$$\times \left[1 + \sum_{n=1}^{\infty} \{ \sum_j \frac{-\mu^i(j)}{\mu^i_o} \triangle W_j \}^n \right] , \tag{6.9}$$

where the suffix o denotes the value at the expansion point;

$\triangle W_i = W_i - W_{io}$, $\quad \triangle W_j = W_j - W_{jo}$.

Since in usual cases,

$$\sum_j \frac{\mu^i(j)}{\mu^i_o} \triangle W_j = \frac{\sum_j \mu^i(j) \triangle W_j}{\sum_j \mu^i(j) W_{jo}} < 1 \ , \tag{6.10}$$

then the series in Eq. (6.9) converges, and Eq. (6.9) becomes

$$I_i = I_{io} + \frac{k_i}{\mu^i_o}\{ \triangle W_i + W_{io} \sum_j \frac{-\mu^i(j)}{\mu^i_o} \triangle W_j \}$$

$$/ \{1 - \sum_j \frac{-\mu^i(j)}{\mu^i_o} \triangle W_j \} . \tag{6.11}$$

Changing the form of Eq. (6.11),

$$\triangle W_i = - W_{io} + \frac{\mu^i_o}{k_i} I_i \{ 1 - \sum_j \frac{-\mu^i(j)}{\mu^i_o} \triangle W_j \} , \tag{6.12}$$

or

$$\frac{W_i}{W_{io}} = \frac{I_i}{I_{io}} \left\{ 1 - \sum_j \frac{-\mu^i(j)}{\mu^i_o} \triangle W_j \right\} . \qquad (6.13)$$

It should be noted that these are not approximate but correct formulae in so far as the condition of Eq. (6.10) is realized.

6.2.2 Two kinds of general calibration formulae

In practice, the determination of the element of interest has to be made by using data of X-ray count rates alone without any knowledge of W_j. So, the transformation of Eq. (6.12) is performed by substituting I_j for ΔW_j as follows. First, for ΔW_j in Eq. (6.12), the same formula [but $i \rightarrow j$, $j \rightarrow k$ in Eq. (6.12)] is substituted.

$$\triangle W_i = -W_{io} + \frac{\mu^i_o}{k_i} I_i \left[1 + \sum_j \frac{\mu^i(j)}{\mu^i_o} \left\{ -W_{jo} + \frac{\mu^j_o}{k_j} I_j \left(1 + \sum_k \frac{\mu^j(k)}{\mu^j_o} \triangle W_k\right) \right\} \right]$$

$$= -W_{io} + \frac{\mu^i_o}{k_i} I_i \left\{ 1 + \sum_j \frac{\mu^i(j)}{\mu^i_o} \frac{\mu^j_o}{k_j} (I_j - I_{jo}) \right.$$

$$\left. + \sum_j \frac{\mu^i(j)}{\mu^i_o} \frac{\mu^j_o}{k_j} I_j \sum_k \frac{\mu^j(k)}{\mu^j_o} \triangle W_k \right\} . \qquad (6.14)$$

Again for ΔW_k in Eq. (6.14), the same formula as Eq. (6.12) is substituted, repeating this,

$$\triangle W_i = - W_{io} + W_{io} \frac{I_i}{I_{io}} \left[1 + \sum_j C_{ij} (I_j - I_{jo})/I_{jo} \right.$$

$$\left. + \sum_j \sum_k C_{ij} C_{jk} (I_j/I_{jo})(I_k - I_{ko})/I_{ko} \right.$$

$$+ \sum_j \sum_k \sum_\ell C_{ij}C_{jk}C_{k\ell}(I_j/I_{jo})(I_k/I_{ko})(I_\ell - I_{\ell o})/I_{\ell o}$$

$$+ \cdots\cdots\cdots\cdots] \ ,$$

$$C_{ij} = \mu^i(j)W_{jo}/\mu^i_o \ . \qquad (6.15)$$

Of course $C_{ij} < 1$ because $\sum_j C_{ij} = 1$. The series in Eq. (6.15) converges rapidly if $(I_j - I_{jo})/I_{jo}$ etc. $\ll 1$. The correction for matrix components is performed by changing the slope in calibration line, in Eq. (6.15).

On the other hand, a more simple calibration formula can be utilized if $\sum \mu^i(j)\triangle W_j/\mu^i_o \ll 1$. Then, Eq. (6.11) becomes

$$\frac{I_i - I_{io}}{I_{io}} = \frac{\triangle W_i}{W_{io}} + \sum_j \frac{-\mu^i(j)}{\mu^i_o}\triangle W_j . \qquad (6.16)$$

The second term in the right side implies the matrix absorption effect. When the relation $\triangle W_i = -\sum_{j\neq i} \triangle W_j$ is put into the second term, Eq. (6.16) becomes

$$\frac{I_i - I_{io}}{I_{io}} = \sum_j a_{ij}\triangle W_j \ ,$$

$$a_{ii} = \frac{1}{W_{io}} \ , \qquad (6.17)$$

$$a_{ij} = \frac{\mu^i(i) - \mu^i(j)}{\mu^i_o} \ , \quad (j \neq i) \ .$$

Using the inverse matrix $[b_{ij}]$ of the matrix $[a_{ij}]$,

$$\triangle W_i = \sum_j b_{ij}(I_j - I_{jo})/I_{jo} \ . \qquad (6.18)$$

The meaning of this linear combination formula is that the correction for the effect of other elements is made by parallel shift without changing the slope of calibration.

6.3 Accuracy, Precision, and Limit of Quantitative Analysis

6.3.1 Accuracy

The accuracy in the determination of concentration (or mass) depends on the uncertainty of the calibration coefficient (error in standardization) and the systematic error of the measured count rate. In the case of Eq. (6.4) for thin specimens, the calibration coefficient is the product of the three factors in the denominator. When the recommended procedure is performed (i.e., the measurement of thick targets of several pure elements and interpolation for $I_i(\infty)$, the calculation of $\mu^i(i)$ from measurement of both thick targets and thin sheets of two kinds of pure elements, and the absorption measurement using a thick target backing and calculation for C_i), the total error of the calibration coefficient for an arbitrary element is considered to be, general speaking, about several per cent, in which the uncertainty of mass absorption coefficient of a table in literature may be a few to several per cent. The calculation of Eq. (6.7) for matrix absorption may cause a larger error in a bad case. The best result must be obtained when the thick target (and foil) of the same kind as the element to be analyzed is directly employed for $I_i(\infty)$, $\mu^i(i)$, and C_i. Then the error of the calibration coefficient results only from the error of its measurement (maybe less than 1 %).

In the cases of Eqs. (6.15) through (6.18) for thick specimens, the errors in calibration coefficients C_{ij}, a_{ij}, or b_{ij} come from both the uncertainties in concentration values of standard specimens used for

determining the coefficients and the errors in measurement of them. The former is usually serious while the latter is comparatively easily reduced, for instance, by repeating the measurement.

6.3.2 Precision

The precision, i.e. the variation in repeated measurements of concentration (or mass), $\triangle W_i$, is related to the variation of the count rate, $\triangle I_i$;

$$\triangle W_i = \triangle I_i / \frac{dI_i}{dW_i} = \triangle I_i / A_i . \tag{6.19}$$

A_i is the calibration coefficient for I_i; in the case of Eq. (6.4), A_i is the denominator itself, and in the case of Eq. (6.17) or (6.18), A_i is a_{ii} or $1/b_{ii}$ for the relative count rate [a_{ij} or b_{ij} $(j \neq i)$ can be almost neglected because they are usually much smaller than a_{ii} or b_{ii}, respectively]. To get better precision, the variation of the count rate is desired to be as small as possible, and the value of the calibration coefficient A_i as large as possible.

When the count rate I (abridging I_i) is obtained from

$$I = S/t = (T - B)/t , \tag{6.20}$$

where S is the net count of the peak, T the total count of the peak, B the background count under the peak, and t the counting time, the standard deviation of I is expressed by those of S, T, and B;

$$\triangle I = \sigma_I = \sigma_S/t = \sqrt{\sigma_T^2 + \sigma_B^2}/t \tag{6.21}$$

For example, if the paired observations of a sample and a blank are made

with a single channel analyzer, σ_S for the count statistics becomes $\sqrt{S + 2B}$. If in a multi-channel spectrum datum the summing channel method with linear background subtraction is used as Eq. (6.22), σ_S for the count statistics becomes Eq. (6.23);

$$T = \sum_{i=\ell+1}^{r-1} y(i) , \quad B = \frac{m}{2n} \left[\sum_{i=\ell-n+1}^{\ell} y(i) + \sum_{i=r}^{r+n-1} y(i) \right] \tag{6.22}$$

$$m = r - \ell - 1 ,$$

$$\sigma_S = \sqrt{S + B\left(1 + \frac{m}{2n}\right)} , \tag{6.23}$$

where $y(i)$ is the count of the i-th channel, m the number of channels for the summing interval, n the number of channels for averaging the neighboring channel counts, and ℓ and r indicate the left hand and right hand channels just outside the summing interval. The other procedure of data reduction gives of course the other estimate of error. Besides the statistical error described above, an error proportional to the count rate is often observed, for instance, owing to gain fluctuation of a measuring system. Then, ΔI is given as $a \cdot I$ (a: the coefficient of relative variation).

6.3.3 Limit of detection etc.

For the limit of detection and quantitative determination, general expressions presented by Currie[52] are considered to be the most reasonable. They are given by the following equations:

$$L_C = k_\alpha \sigma_0 , \tag{6.24}$$

$$L_D = L_C + k_\beta \sigma_D , \tag{6.25}$$

$$L_Q = k_Q \sigma_Q , \tag{6.26}$$

where L_C, the critical level, is the number of count which an observed signal must not exceed in order to yield the decision "not detected" with a probability of $1-\alpha$. The detection limit, L_D, is the true mean of a signal whose distribution of possible outcomes intersects L_C such that a given fraction, $1-\beta$, of them will be greater than L_C. The determination limit, L_Q, is defined as the true mean of a signal whose relative standard deviation is $1/k_Q$. The quantities σ_o, σ_D, and σ_Q are the standard deviations associated with zero, L_D, and L_Q net counts, respectively, and k_α and k_β are abscissas of the standardized normal distribution corresponding to the probability levels $1-\alpha$ and $1-\beta$.

For example, the values of L_C, L_D, and L_Q of the net count S are obtained in the case of the summing-channel method, as follows[58]: σ_o, σ_D, and σ_Q are given by putting $S = 0$, L_D, and L_Q, respectively, into Eq. (6.23), and then, they are substituted into Eqs. (6.24) to (6.26), and setting $k_\alpha = k_\beta = k$, thus,

$$L_C = k\sqrt{B\left(1 + \frac{m}{2n}\right)}, \tag{6.27}$$

$$L_D = k^2 + 2k\sqrt{B\left(1 + \frac{m}{2n}\right)}, \tag{6.28}$$

$$L_Q = \frac{k_Q^2}{2}\left\{1 + \sqrt{1 + 4\left(1 + \frac{m}{2n}\right)B/k_Q^2}\right. . \tag{6.29}$$

In the X-ray spectroscopic analysis, B is usually much larger than unity. The value of $\alpha\,(=\beta)$ may be set on 0.05; then $k = 1.645$. In such a case, the detection limit becomes almost twice the critical level, and it is proportional to $\sqrt{B}$. On the other hand, k_Q may be set on a certain value larger than unity from the definition (for example 10).

In the case when the least-sequares curve fitting with a standard peak shape and polynomials as the background is used for data reduction,

σ_o is expressed as follows[59]: for the fitting of a gaussian function and zero- or first-order polynomials,

$$\sigma_o^2 = 2\sqrt{\pi}\sigma b / [1 - 2\sqrt{\pi}(\sigma/n)], \tag{6.30}$$

and for the fitting of a gaussian function and second- or third-order polynomials,

$$\sigma_o^2 = 2\sqrt{\pi}\sigma b / [1 - 4.5\sqrt{\pi}(\sigma/n) + 60\sqrt{\pi}(\sigma/n)^3 - 360\sqrt{\pi}(\sigma/n)^5], \tag{6.31}$$

where σ in the right side is the standard deviation of peak gaussian, b the cout of background per channel, and n the number of channel in which the fitting is made. It is to be noted that σ_o is proportional to the square root of the background count, also in this case. And on the analogy of the summing-channel method, the detection limit will be approximately twice the critical level.

7. Construction and Performance of an X-Ray Analyzer

Taking up cement raw material mixtures as a typical object of the X-ray spectroscopic analysis of low Z elements, an industrial X-ray analyzer which could determine the four main components, i.e., lime, silica, alumina, and ferric oxide simultaneously was completed[60)61)]. Here, the lower Z elements aluminum (Al_2O_3, ca. 3 %) and silicon (SiO_2, ca. 14 %) must be accurately analyzed in the sample containing a large amount of the higher Z element calcium (CaO, ca. 44 %). For this purpose, the use of an alpha-ray source was especially needed.

To complete the practical analyzer, in addition to choice of sources, development was made of (1) an industrial-use gas flow proportional counter for soft X-ray detection, (2) a vacuum-sealed measuring head in which the sample is exchangeable without air inflow, and (3) the pulse-height stabilization by automatic gain control.

The analyzer may be the world first X-ray analyzer with radioisotope for analyzing light elements in manufacturing process. It was installed together with a process-control computer in October 1964 in new Kanda Cement Factory of Ube Industries, Ltd., where it has been operated 24 hours daily over more than ten years to control the mixing ratio of cement raw materials.

7.1 Measuring Head

7.1.1 Choice of sources

As is evident from the studies of chapters 3 and 4, the excitation of X rays by alpha rays becomes more advantageous for lower Z elements. So, to excite with high intensity and good S/N ratio the lower Z elements aluminum and silicon under the existence of the higher Z element calcium in high concentration, the use of an alpha ray is considered to be most desirable. However, an alpha-ray source accompanied by emission of rather high energy conversion electrons is ruled out for the reason described in 4.1. And the source window is necessary to be sufficiently thin not to diminish the advantage.

An α-ray source of 10 mCi ^{210}Po, the PDC-10 made by RCC(amersham), was chosen because of its small size(high specific superficial activity) and the commercial availability(at that time), though the half life is not long(138 d). Polonium is electrodeposited on the tip of 0.9 mm platinum wire which is encased in a brass tube of 4.8 mm dia. and 25 mm long. The end window of 2 mm dia. over the active surface of the source was replaced by an aluminum foil of 1.5 mg/cm^2 thickness (later, a titanium foil of the same thickness was adopted), so that the source could be used safely in vacuum.

For the determination of a small content of iron component, the use of ^{210}Po source alone is insufficient, because the efficiency of X-ray excitation by α rays is low for such a rather high Z element. X rays or γ rays adequately higher in energy than the X-ray absorption edge of iron is most desirable. Thus, a soft X-ray source of ^{3}H/Zr, TRT-2 made by RCC, was adopted. Tritium of 3 Ci is absorbed in a thin layer of zirconium melted onto a tungsten disc of 11 mm dia. and 0.5 mm thick. The surface

of the source was covered with a thin aluminum foil (or mica, ca. 1.5 mg/cm^2) to absorb the ß particles and very soft X-rays such as Zr LX rays. This filter reduced the background in the pulse-height range where the Si and Al KX-ray peaks must arise (cf. 4.2.3, Fig. 23).

Both the ^{210}Po and $^{3}H/Zr$ sources were used two pieces respectively and arranged as shown in Fig. 34.

7.1.2 Detector

A gas-flow proportional counter was adopted as the soft X-ray detector, for geometrical and intrinsic efficiencies and because of the sufficient energy resolution, considering the first half of studies of chapter 5. As a matter of fact, Si(Li) detectors were not yet available at the time of construction of the analyzer. However, a proportional counter has rather better pulse-height distribution characteristics than those of Si(Li) detector, for soft X rays, as is seen in the comparison of the detector figure of merit, though it has some demerits such as less energy resolution and temperature (or pressure) dependence.

The counter used is the same one as described as "counter C" in 5.1. The cathode shell is a brass cylinder of 35 mm inner dia. and 300 mm long (later, a length of 150 mm was found sufficient to avoid the end effect). The anode is a 0.05 mm dia. tungsten wire, the ends of which are welded to nickel lead wires and led outside through hermetic seals. The window (30 mm × 20 mm), a Mylar film of 6 μm thickness, is coated with evaporated aluminum on the inner surface. The frame, strung with tungsten wires of 0.1 mm dia. at intervals of 3 mm, is placed on the window to make the window vacuum-resistant.

As the flow gas, argon gas containing 10 % methane, i.e., PR gas,

is preferable when the counting efficiency, the resolution and the applied voltage range with good resolution are concerned. The gas was made to flow at a rate of 100 cm^3/min at atmospheric pressure. The decrease of pulse height, as the flow rate was increased from 50 to 300 cm^3/min, was within 2 %. However, the 1 % change of the gas temperature or pressure caused a change of the pulse height by nearly 9 %, so stabilization of the pulse height had to be devised by some means. Incidentally, variation of the counting efficiency due to variation of gas density was negligible.

The gas amplification factor was several thousands at the applied voltage of 2000 volts. The energy resolution almost agreed with the theoretical value: 17 %, 23 %, and 36 % FWHM for the KX rays of Fe, Ca, and Al, respectively. The calculated counting quantum efficiency was 69 %, 93 %, 57 %, and 41 % for the Fe, Ca, Si, and Al Kx rays, respectively.

Two counters of the same dimension are used: one with a filter of 1.5 mg/cm^2 aluminum on the window (the Si KX ray alone is almost absorbed by this filter), and the other with no filter.

7.1.3 Arrangement of source, sample, and detector

Radioisotope sources, sample to be analyzed, and X-ray detectors could be arranged so that the geometrical efficiency might become maximum, if necessary, as the scattering of the primary radiations was slight. However, for the convenience of practical use, the source holder and detectors were arranged to be taken out separately. The source holder can be pulled out along the guide rail and the detector can be taken out with their common base plate. The arrangement is shown in Figs. 34 and 35.

The sample size was decided so as to be as small as possible in the range where X-ray emission and its S/N ratio decreased only slightly,

for convenience of sample preparation described later (cf. 8.1.1). The sample is contained in the holder, made of iron and plated with silver to reduce the background. The sample holder at the measuring position can be rotated at 1 rpm on a ring gear fitted with a magnet. The inner surface of the measuring head facing the sources is masked with an acrylic resin plate.

To avoid the loss of primary (α and X) and secondary (KX) radiations in their passage, the measuring room in the measuring head is kept at about 0.1 mmHg vacuum.

An acrylic resin window is provided for viewing the interior of the measuring room.

7.1.4 Sample exchange mechanism

Even when the sample is being taken out for renewal, the measuring room in the head is kept evacuated not to damage the delicate film window of both the sources and the counters and at the same time to speed up the analysis, by the mechanism explained below.

The sample holders are set in two holes diametrically opposed on a circular turntable. Both holders are moved by turning the table (with a handle), which is stopped by a stopper operating against the turntable, at the position where one holder comes just over the sources and the other holder comes over the base support (the bottom of the sample-exchange room) (cf. Fig. 35).

Pulling the lever slightly lifts the sample holder with the base support to isolate the exchange room from the vacuum system by O-ring seals both at the top and the bottom of the holder, and to admit air into the room. Thus the sample can be exchanged with another by opening

the lid of the room. After this, reversed manipulation of the lever evacuates the room and removes the O-ring seals, whereby the renewed sample becomes ready to be put into the measuring room.

The air filling and evacuation of the sample exchanging room are automatically made through electromagnetic valves linked with the lever operation. The evacuation of the measuring room is made through a buffer tank to reduce sudden pressure variation.

Fig. 36 shows, on the right, an outside view of the measuring head mounted on a table under which two rotary pumps, two electromagnetic valves, and a buffer tank are arranged. On the front panel two sets of gas flow meters, a vacuum gauge, manual valves of the vacuum system, and electric switches are arranged. A control box connected to a computer is seen at the right corner on the table.

7.1.5 Pulse-height spectrum

The pulse-height spectra of a cement raw mixture sample, processed by the method described later (cf. 8.1.1), were obtained by scanning a narrow channel of the pulse height analyzer, as shown by the solid lines in Fig. 37. To check the performance of the measuring head, using samples of pure elements, i.e. iron plate, processed calcium oxide, and aluminum plate individually, the spectra were also obtained as shown in Fig. 37 (broken lines). Although the peaks are well separated, their tails (containing scattering rays and escape peak) are overlapped by other peaks. Therefore, the count, taken in a channel for one element, may include the count of other elements as the background, the amount of which can be roughly estimated by the percentage obtained as follows. When the Fe channel was set wide enough to cover most part of the Fe peak,

the ratio of the tail count of CaO to the peak count of Fe, denoted by CaO/Fe-ch., was about 6 %. Likewise, in other channels, Al/Ca-ch. = 3.6 %, CaO/Si-ch. = 0.9 %, and CaO/Al-ch. = 0.5 % (for Al-ch., the aluminum filter was used). The values of Si-channel and Al-channel are sufficiently small. If the ^{3}H/Zr source alone is used, the values in Si-channel and Al-channel must be much inferior to the above values : at best several per cent[44].

7.2 Measuring Circuit

7.2.1 Method of spectrometry

Peaks in pulse-height distribution of KX rays from Fe, Ca, and Si (or Al) are sufficiently separated as shown in Fig. 37. Therefore, when the pulse-height channel is adjusted to catch a particular peak, the counting can be made selectively. On the other hand, KX rays of Al produced from a sample containing both Al and Si can be measured separately from Si KX rays by use of the counter with aluminum filter. However, the count in the channel set in the usual manner to catch Si KX rays , in the counter without filter, includes the count of Al KX rays also. To obtain the count which relates almost solely to the Si content but not to the Al (or Mg) content, a special channel setting is devised for the overlapping peak of the Si, Al and Mg KX rays with the counter without filter (cf. 8.1.2). The lower level of this channel is set so that the count-increase of Al or Mg KX rays in the channel is canceled by the count-decrease of Si KX rays due to the absorption in the sample. The same idea may be applied also to the Al channel setting with the counter with aluminum filter, to reduce the influence of Mg content to the Al content determination.

All the channels are arranged in parallel to analyze those elements at the same time, using single-channel pulse-height analyzers.

7.2.2 Blockdiagram

Fig. 38 shows a blockdiagram of the measuring circuits which have five sets of single-channel pulse-height analyzers(PHA) as the main element. The four PHA's correspond the four main components in cement raw materials. The fifth channel is provided for spare, and can be utilized for obtaining the sum content of silica and alumina, or determination of magnesia (for which Dolby's method[62] may be useful).

Another important point of the circuits is an automatic control feed back loop provided for each proportional counter to stabilize the pulse height. Details of the loop is described in the next section (cf. 7.2.3).

All the circuits, made by Kobe Kogyo Corp., are transistorized in current-coupling type, except the nuvista tube at the top of the preamplifier and the decatrons in the electronic timer. The circuits are composed of the following module sets, most of which except the pulse-height stabilizer are standard modules (at that time) used in gamma-ray spectrometers, etc., with some modifications :

PA : charge sensitive preamplifier,

LA : linear amplifier including signal distributor(four outputs),

PHA : single-channel pulse-height analyzer,

PHS : pulse-height stabilizer,

S : binary-coded decimal system scaler,

T : electronic timer,

HV : high voltage supply,

LV : low voltage supply,

AS : auto-scanner of level of pulse-height analyzer*,

RM : counting rate meter*,

R : recorder*,

(* provided for examination of pulse-height spectrum).

A binary-coded decimal scaler , consisting of binary scale transistor circuits, is used because of the long-term reliability and the convenience in visual checking of the counts.

The modules assembled on a rack are shown on the left in Fig. 36. In the bottom, spare modules are preserved.

7.2.3 Pulse-height stabilizer

After the success in a preliminary experiment for pulse-height stabiliztion[63], the method of de Waard[64] was adopted. Furthermore, the investigation were made for design of the circuit, by means of the statistical method in automatic control theory.

To detect the pulse-height variation, the channel level of the PHA in the feed-back loop is scanned in the small range, the center of which is set at the level of the mean pulse height of a prominent peak (for which the Ca KX-ray peak is chosen on account of sufficient height and almost symmetrical shape), in the sine wave of a.c. line frequency (60 Hz). The output is, through a flip flop, fed to the positive or negative rate-meter circuit, according to the phase of the scanning cycle (cf. Fig. 39). The difference between the outputs of the two rate-meters, which is proportional to the deviation of the mean pulse height, becomes the correcting signal to the controller circuit, which is the integral action circuit with a transistor-chopper amplifier. The output is supplied to HV to control the gas gain of the proportional counter.

The conditions to be satisfied for the feed-back loop, derived from the theoretical treatment, are as follows : (1) since the response speed depends almost on the band width of the closed-loop transfer function alone, only the integral action is necessary and enough, and the time constant of the rate-meter circuit is desired to be rather small ; (2) the maximum permissible value of the band width is proportional to the counting rate to restrain the fluctuation of the pulse height, resulting from the statistical variation of the counting rate, within a permissible limit; (3) the maximum permissible value of the gain constant in the integral-action control is proportional to the band width, therefore from (2), to the counting rate (so, for the rate-meter circuit, the method taking the difference of the positive and negative rate-meters is preferable to that taking the ratio of the two rate-meters).

The actual circuit of the pulse-height stabilizer was made so as to satisfy the above conditions. The random variation in pulse height is restrained at the sacrifice of the speed of the response depending on the counting rate. In practice, no quick variation on the gain may occur. Stationary errors in pulse height are suppressed by the high gain of the chopper amplifier. During the change of the position of the sample holders by turning the table, the output is held unchanged by automatically switching off a relay at the entrance of the chopper amplifier.

The important problem in relation to the pulse-height stabilization is stability of the discrimination level of the pulse-height analyzer because it is the basis of control in the feed-back loop and on the other hand PHA used for analysis is outside the control loop, though it is the most important element for analysis. Prior to the construction of the analyzer, the stability test on the nine sets of PHA (including spares)

was made. The result showed the small temperature dependence which was comparable with that of a good vacuum tube PHA. The variations of lower and upper levels were within about 0.1 % and 0.15 %, respectively, against the level full range per 10^{o}C in $10^{o}$to 40^{o}C.

Setting the permissible limit of pulse-height variation to 0.3 % in the relative standard variation, the actual variation in short and long time was sufficiently small compared with this limit. And the response speed was about 10 sec at the counting rate 100 cps.

8. Applications

First, the quantitative analysis of the main four components in cement raw material mixtures is described as a performance test of the analyzer of chapter 7. Description is given of (1) the sample preparation using the fusion method to eliminate the microscopic heterogeneity effects including the problem of particle size in powder samples, (2) the channel setting to minimize the influence of the elements other than that of interest in an overlapping peak, (3) the calibration considering the correction for matrix effect and the content correlation between components, and (4) the final results of analysis. The accuracy and precision rather better than that in conventional fluorescent X-ray analysis were obtained. The use of the analyzer is considered to be favorable, for it is simple in princilpe, easy in practice, speedy in measurement, and economical.

Second, the qualitative and quantitative analysis of air-pollution samples is presented as a typical example of multi-elements analysis in thin specimens by application of the proposed calibration method. A thin specimen has the advantage that the matrix effect is almost negligible or can be easily corrected. Besides, the fluorescence to scatter ratio is greater than that in a thick specimen when the X-ray energy of the element of interest is considerably lower than that of the primary radiation (X or γ rays) and the atomic numbers of matrix elements are low[65]. In this analysis, a high resolution semiconductor detector system was needed to analyze adjacent multi-elements (more than 10). Comparing the results with those in neutron activation analysis, the agreement was fairly good. The proposed X-ray method is considered to be advantageous because of

(1) the capability of simultaneous analysis of the main multi-elements including the elements which are difficult or impossible to be determined by neutron activation analysis, (2) the simplicity and rapidity of analysis, and (3) the complete non-destructive analysis. It will be useful hereafter for the analysis of pollution or environmental samples and so on.

8.1 Analysis of Cement Raw Mixture

8.1.1 Sample preparation

The intensity of a fluorescent X ray produced from a powder sample is, as is generally known, much influenced by the microscopic heterogeneity, due to the differences in the grain sizes and the mineralogical characteristics, especially for light elements. In the case of the mixture of various kinds of minerals such as cement raw materials, elimination of the heterogeneity effect is still difficult by long time pulverization, and separate calibration lines are often required for samples which come from different mines.

To avoid these problems, a fusion technique[66)67)] was developed. The sample is mixed in a platinum crucible with an equal amount of the flux $Li_2B_4O_7$ and heated to be fused in an electric furnace at 1400°C during ca. 5 min (the process up to this point is the same as Andermann's[68)]), and then the fused sample is poured into an iron ring (26 mm inner dia., 3mm high) which is placed on a stainless steel plate heated at an appropriate temperature, thus a flat glass-like disc with an iron ring is made, without regrinding. This procedure requires about 10 min. Thus processed samples have good quality also in point of the rigidity and the stability.
At the time of measurement the iron ring is masked by the edge of the sample holder (cf. Fig. 34).

41 specimens collected from cement manufacturing factories were prepared by the above method for the analysis by X-rays. On the other hand, those specimens were analyzed by the ordinary method of chemical analysis in the laboratory of the factory.

8.1.2 Channel setting

The channel setting for the determination of Fe and Ca contents is quite easy because their peaks are well separated, but for the determination of Si a special channel setting has to be devised for the overlapping peak of the Si, Al and Mg KX rays, as is mentioned already.

The principle of the method[63] is shown in Fig. 40. Suppose that the X-rays of the element A to be analyzed is strongly absorbed by the lower Z element B. When the content of element B alone increases by a small quantity, the peak of B becomes of course higher while the peak of A becomes lower because of the increase of absorption in the sample. Therefore, if the lower level of the channel is set at the appropriate level, the count increase of element B is canceled by the count decrease of element A (cancel effect).

This effect was experimentally confirmed on the relation between the Si and Al contents, and between the Si and Mg contents. Three samples were prepared by addition of pure reagents to a base sample in which the contents of Al_2O_3 and MgO were small: (1) the content of Al_2O_3 alone was so increased as to become the highest concentration in cement raw mixtures, (2) the content of MgO alone was similarly increased, and (3) both the Al_2O_3 and MgO were increased (but the SiO_2 was fixed). Measurements were made by changing the lower level of the channel, the upper level of which was fixed at a valley level between the Si and Ca KX-ray peaks.

Fig 41 shows a result of the experiment: the increase in Al KX-ray count due to the increase in Al_2O_3 content, in the channel for Si KX-ray counting, is canceled barely at a rather high level, while the effect of MgO is canceled at a lower level. And the total effect of both Al_2O_3 and MgO seems to be the superposition of the effects of respective components. The cancel level for both Al_2O_3 and MgO was almost just the center of Si

KX-ray peak. With this level setting, the deviation is restrained within ± 1 % in the counting rate, even though the effects of the two components are not completely canceled, since the variation of Al_2O_3 and MgO contents in actual samples are usually less than the change in the experiment described above.

Also for the Al_2O_3 analysis, a similar experiment was done with the detector with aluminum filter. Thus decided channels were used in the following analyses. The channels are shown in Fig. 42, together with other additional channels which were used in experiments for derivation of matrix coefficients. [A 200 channel pulse-height analyzer was used in the following (8.1.3 & 8.1.4) instead of single channel analyzers].

8.1.3 Calibration coefficients for matrix effects

Since the range of concentration variation of each component in actual samples is not large, the linear equations Eqs. (6.17) and (6.18) are considered to be usable as the matrix correction formula. Here, Eq. (6.17) is transformed into Eq. (8.1), using the count rate including the background (I_B) ; $I_j + I_{jB} \rightarrow I_j$.

$$\frac{I_i}{I_{io}} = \sum_j a_{ij} W_j + a_{io} , \tag{8.1}$$

$$a_{ij} = \left(1 - \frac{I_{iB}}{I_{io}}\right) \frac{\mu^i(i) - \mu^i(j)}{\mu^i_o} , \quad (j \neq i) ,$$

$$a_{ii} = \left(1 - \frac{I_{iB}}{I_{io}}\right) \frac{1}{W_{io}} ,$$

$$a_{io} = 1 - \left(1 - \frac{I_{iB}}{I_{io}}\right)\left\{1 + \sum_{j \neq i} \frac{\mu^i(i) - \mu^i(j)}{\mu^i_o} W_{jo}\right\} ,$$

where the suffix o means the reference sample; all the a_{ij}'s are different from those in Eq. (6.17). In the case of a sample prepared by the fusion method, Eq. (8.1) is slightly modified: i.e., the value of $\mu^i(j)$ for the ignition loss component becomes zero, and the term of the flux is added in a_{io}. Corresponding to Eq. (6.18),

$$W_i = \sum_j b_{ij} \frac{I_j}{I_{jo}} + b_{io} , \qquad (8.2)$$

$$b_{io} = - \sum_j b_{ij} a_{jo} ,$$

where $[b_{ij}]$ is the inverse matrix of $[a_{ij}]$.

Special samples to determine the calibration coefficients (a_{ij} and b_{ij}) were prepared by mixing and fusing pure reagents alone, according to an orthogonal array in the design of experiments. The content of a component to be measured was changed at 9 levels within a small range of the same extent as in actual raw mixtures, while the contents of the other components were changed at 3 levels in a large range enough to obtain small values of $a_{ij}(j \neq i)$. Each sample was measured for 10 min with the channels shown in Fig. 42. The values of a_{ij} and a_{io} were obtained statistically by calculating partial regression coefficients. The results are shown in Table 7. The attached errors indicate the 95 % cofidence intervals. The number j is assigned to each component from high to low Z element: 1 = Fe_2O_3, 2 = CaO, 3 = SiO_2, 4 = Al_2O_3, 5 = MgO, and 6 = ignition loss component.

As is mentioned already, the value of a_{ii} is desired to be as large as possible from the viewpoint of precision. On the other hand, small values are favorable for $a_{ij}(j \neq i)$ because of small correction. The following facts are found from Table 7: (1) in the Fe-channel, only a_{12}

is significant among a_{1j}'s($j \neq 1$) and it shows the absorption effect due to CaO, and the background fraction I_{iB}/I_{io} is considerably large, (2) in the Ca-channel, all a_{2j}'s($j \neq 2$) except that of ignition loss show the absorption effect and it should be noted that their effects are comparatively large since a_{22} is not large as a main component coefficient (owing to the large mean content and the background), (3) in the Si-channel, a_{34} and a_{35} are relatively small, so it means that the channel setting works well, and (4) No.6 channel is the best among Al-channels. On the whole the values are considered to be valid.

Then, the values of b_{ij}'s were obtained by calculating the inverse matrix of a_{ij}'s. Since there was no channel to measure the ignition loss component, the product of the a_{j6} and mean of W_6 was added to the constant term b_{io}. On the analogy of the discussion for a_{ij}, the value of b_{ii} is desired to be as small as possible, and still smaller values are favorable for $b_{ij}(j \neq i)$.

Apart from the above matrix coefficients, a calibration line was obtained for each component, in the usual method, by calculating the simple regression coefficient directly from the data of 41 specimens of cement raw mixtures, neglecting the matrix effect (using No. 1, 2, 3, and 6 channels for Fe_2O_3, CaO, SiO_2, and Al_2O_3, respectively).

8.1.4 Quantitative analysis

Each of the 41 specimens was measured for a sufficiently long time (10 min, 2 times) to examine the accuracy and precision of the analysis, with No. 1, 2, and 3 channels employing the counter without filter and No.6 and 8 channels by the counter with aluminum filter. The count ratio of the specimen to the reference was converted to the weight fraction by using

the two kinds of calibration coefficients described in the preceding section (8.1.3), partial regression coefficients and simple regression coefficients. Comparing them with the values of chemical analysis, the deviations in weight per cent (standard deviation) of the 41 specimens were calculated. The results are shown in Table 9, in which also the statistical errors of the count, the deviations of the count ratio from the calculated one, etc., are shown for comparison. The calculated count ratio was obtained from the calibration coefficients and the values of chemical analysis. Figs. 43 through 46 are the graphs of the simple correlation between the data(count ratio) of No.1, 2, 3 and 6 channels and the values of chemical analysis for Fe_2O_3, CaO, SiO_2, and Al_2O_3, respectively.

The standard deviations for the determined values by the calibration lines of simple regression show fairly good values. The results are apparently better than Andermann's[68] with single calibration lines in the conventional X-ray fluorescence analysis using an apparatus with an X-ray tube, and also better even in comparison with his data with separate calibration lines (except SiO_2). On the other hand, the deviations of the determined values by the multiple regression calibration using the partial regression coefficients (matrix coefficients) are almost equal to those by the simple regression coefficients except that of CaO. The deviation of CaO is considerably larger than that by the simple regression coefficient. Even though the correction is made for the ignition loss, the deviation is still larger.

It is very interesting to search the origin of this paradoxical fact. As described previously in 6.3.2, the deviation in the determination with a linear combination formula depends almost solely on the main term (term

of a_{ii} or b_{ii}). Though the deviations in determined values of CaO are much different between the simple and the multiple regression methods, the deviations in the count ratio agree each other between the two calibrations, in the calcium channel (cf. Table 9). Suppose the case where no error exists in the calibrations. Then,the count-ratio deviations must be due to the error in the measurement itself but not to the sample side (chemical analysis, sample preparation, etc.). Because they have similar values between the two methods where the calibration coefficients are much different in magnitude. And the counting error is attributed to the instrumental one such as change in the excitation, detection, and geometrical efficiencies, for the statistical error of count is one-third as large as the count-ratio deviation (cf. Table 9). However, it is considered that the error in the calibration is not so negligibly small in particular for the partial regression coefficient (cf. Table 7). And in that case, the error in the sample side also becomes necessary to be taken into account.

At any rate, the cause of larger value in the weight per cent deviation is apparently related to the smaller value of the main coefficient in calibration. It is worthy of notice that the value of the simple regression coefficient A_2 is much larger than that of the partial regression coefficient a_{22}. The reason is explained by the following fact.
First, there is a clear negative correlation between the content of CaO and that of the other component except the ignition loss(only for the ignition loss, a positive correlation). Fig. 47 shows an typical example between the CaO and the SiO_2. Second, the a_{2j}($j \neq 2, 6$) has a relatively large negative value, as is mentioned already. Therefore, when the content of CaO increases, the matrix absorption effect decreases

so that the excess increase of the Ca KX-ray count arises. The ignition loss component also has similar effect because of the positive correlation and the positive matrix coefficient. The effect of excess increase of the count is incorporated in the value of the simple regression coefficient. The fact was quantitatively confirmed by calculation.

From the above discussion, it can be said that the quantitative analysis by the matrix coefficients also works well. However, the analysis with the simple regression coefficient is more simple and advantageous for the routine use, as the content deviation from the regression line in the inter-component correlation is usually small. Since the statistical errors of count were much less than the observed (the count-ratio deviation), the counting time in practice will be able to reduce to less than 5 min, so the measurement becomes sufficiently rapid. At the time of the experiments, the activity of the ^{210}Po source used was less than half the initial activity (20 mCi in total). If a new source of full activity is used, the counting time can be furthermore reduced. It is concluded that both the analyzer and the method described above have the sufficient utility.

8.2 Air Pollution Analysis

8.2.1 Sample and apparatus

Samples were collected by pumping 220 to 450 m^3 of air through 47 mm dia. Millipore membrane filters (0.8 μm pore size) with a vacuum pump during 2 weeks at various sampling points in the country, according to a project on the analysis of atmospheric pollutants entrusted from the Environmental Agency. The use of the Millipore membrane filter is favorable on account of low blank values of metal elements. The mass thickness of

collected airborne particulate was 0.25 to 2.6 mg/cm^2, and the effective size on the filter was about 43 mm in diameter.

The apparatus used is a Si(Li) X-ray spectrometer with an ORTEC Si(Li) detector, FWHM 186 eV for Mn Kα rays. The sensitive area and depth of the detector are 30 mm^2 and 3.5 mm, respectively, and the window of the cryostat is 1 mil thick beryllium. Main amplifier ORTEC 716A was used in the mode of unipolar with time constant 6 μsec and low count rate. The pulse-height spectra were taken by a Packard 900 series 4096 channel analyzer(using a quarter memory).

For high signal intensity and low background ratio in the X-ray analysis with a Si(Li) detector, a monochromatic X or gamma ray whose energy is 1.5 to 2 times the energy of X ray to be excited is most desirable as the primary radiation. If the maximum energy of X ray to be analyzed is that of Pb Lα ray(10.5 keV), the desirable energy of the primary radiation is 15 to 20 keV. As a source which satisfies almost this condition, a ^{238}Pu X-ray source, PPC.5(30 mCi, disc type) made by RCC, was adopted. The diameter and height of the stainless steel capsule is 10.8 mm and 5 mm, respectively, and the window is 0.125 mm thick aluminum. The principal radiations observed are the 13.61 keV U Lα(28.8%), 17.22 keV U Lß(58.5%) and 20.16 keV U Lγ(14.7%) X rays.

The source and sample were arranged in a broad beam geometry, as shown in Fig. 48.

8.2.2 Qualitative analysis

Fig. 49 shows the X-ray spectrum obtained for a specimen of particulate mass 1.37 mg/cm^2(air sampling volume 422 m^3). The broken line shows the background spectrum obtained with a blank filter of the

same kind. The peak of Au Lα rays is due to fluorescence of the thin gold layer on the surface of Si(Li) detector, which was excited by the scattered photons from the specimen. Similarly, the Ni Kα-ray peak is considered to be due to some constructional material of the detector system. The small peak of Fe Kα rays in the blank filter spectrum is due to fluorescence of the source capsule. The Ar Kα-ray peak originates from argon in the air. No peak is observed which is generated from the filter itself.

As the peaks of airborne particulates, 19 peaks were observed and they were identified to be due to 14 elements, from the positions of peaks in channel number which had been calibrated in 20 eV/channel, as shown in Fig. 49: S(Kα), Cl(Kα), K(Kα), Ca(Kα, Kß), Ti(Kα), V(Kα), Cr(Kα), Mn(Kα), Fe(Kα, Kß), Ni(Kα, Kß), Cu(Kα), Zn(Kα, Kß), Pb(Ll, Lα), and Br(Kα). Thus, except a few elements whose content is very small and its Kα peak overlaps a Kß peak (etc.) of other element, such as Sc, all elements neighboring each other were identified.

8.2.3 Quantitative analysis

The determination of the 14 elements were made by means of the calibration technique proposed in 6.1. Table 10[54] shows the values in the process of the determination in the specimen of Fig. 49. Since many peaks overlap in skirt as seen in Fig. 49, the computation of the net peak count rate $I_i(m_i)$ was made for convenience by a peak shape fitting method where a calibrated gaussian function with exponential tail at low energy side and 3rd order polynomials were used as the peak shape function and background, respectively, and the peak height of gaussian function was determined by the least-squares fitting. The summing-channel method also

can be used but it may give somewhat larger systematic error.

Measurement of $I_i(\infty)$ was made with pure targets of sulfur, titanium, iron and zinc for Kα-series, and further lead for the Lα rays. To avoid the counting loss due to the pulse pile-up in high counting rate, the values of $I_i(\infty)$ for iron and zinc were obtained by reducing the source radiations with a brass mask having small holes and multiplied by the intensity ratio between with and without the mask. For elements other than the five elements, the interpolation was made with a smooth curve as shown in Fig. 50.

The value of $\mu^i(i)$ for each element was calculated from the total mass absorption coefficients of Ref. 28 and the values of cosec ϕ_1 and cosec ϕ_2 obtained with the method described already(cf. 6.1.1) by using the thick target and foil of titanium and copper : cosec ϕ_1 = 1.4 and cosec ϕ_2 = 1.2[54].

Determination of the matrix absorption was made by measuring the intensity ratio of Ti Kα ray from a titanium target between with the specimen and with a blank filter in front of the target. The difference of filter thickness was also taken into account (the relation between the absorption and the filter thickness was measured in advance). The factor of the matrix absorption for the other elements were calculated from the value for titanium by means of Eq. (6.6) and (6.7).

Finally, putting thus obtained count rate and factors for each element into Eq. (6.4), the mass thickness of each element (g/cm^2) was determined. Errors shown in Table 10 are due to the errors (standard deviation) of peak count computed by the peak-shape fitting, which are composed of statistical errors and errors of misfitting. This error of the peak count-rate determination is considered to be the largest error source for the final results

of most elements, because the amounts of elements are small and therefore the numbers of count in their peaks are low, except a few elements such as iron. A more intense source or a larger sensitive-area detector is necessary for improvement in this respect.

The systematic errors in the determination, resulting from the errors of calibration coefficient, are as follows. First, of the three factors of the denominator of Eq. (6.4), the error of $I_i(\infty)$ is caused by the interpolation or extrapolation. The former may be within a few per cent, but the latter may be somewhat larger. Second, the error of calculated $\mu^i(i)$ is considered to be within a few per cent or several per cent at most, including the uncertainty of mass absorption coefficient and the error in estimation of cosec ϕ_1 and cosec ϕ_2. The error for the measured value of $\mu^i(i)$ must be further less. Third, there is the error in the estimation of C_i ; i.e., the error in the calculation by Eqs. (6.6) and (6.7). As the absorption is measured at the energy of Ti Kα ray and the calculation for the other element X ray is made by using Eq. (6.6) with n = 2.80, the matrix element should have the absorption edge of energy lower than both Ti Kα ray and the X ray of the element to be calculated. An actual specimen does not strictly fulfill the condition. However, a test experiment showed fairly good agreement between the observed absorption and the calculated one (cf. Fig. 51). This means that the effective atomic number of the matrix is rather low. At any rate, the error in the calculation of the matrix absorption is not large, compared with the other errors. In this connection, the absorption of Ti Kα rays of 26 specimens showed a clear correlation with the total mass thickness of particulates (cf. Fig. 52). This suggests the possibility of the matrix absorption correction by calculation from the mass thickness without any absorption measurement.

Thus determined values were compared with those of the neutron activation analysis, and the agreement is excellent for manganese and fairly good for vanadium, as shown in Figs. 53 and 54, respectively. Manganese is one of the most sensitive element in the neutron activation analysis and the error of the analysis is considered to be small (maybe less than several per cent). In the X-ray analysis, however, the Mn Kα-ray peak is not so large, as seen in Fig. 49, and is always smaller than the Fe Kα-ray peak. Vanadium is an example whose error is rather large in both analyses. After all, these results shows the validity of the proposed method and the technique can be successfully applied to a broad-beam geometry also and even to a polychromatic primary radiation.

9. Summary

Fundamental and application studies on the excitation of characteristic X rays by alpha particles from radioisotopes were made for low Z elements. The thick target yields of K X rays of carbon through titanium were measured with alpha particles from a ^{241}Am source reduced in energy by foil filters. From these data, atomic cross sections of K-shell ionization for 2 to 4 MeV alpha particles were derived. The obtained thick target yields and atomic cross sections agreed fairly well with previous proton data and also two theories, the Born approximation and the binary-encounter-impulse approximation. However, the small systematic deviation of alpha-particle data for carbon from both the proton data and the theoretical curve appears to be a symptom of substantial discrepancy. The yield of C K X rays does almost not change within 2 to 4 MeV of alpha particles while that of higher Z element decreases rapidly with alpha energy. The X-ray excitation by alpha particles in very low Z elements such as carbon is more efficient than that by other radiations.

In actual alpha-ray sources, interferences of the accompanying gamma rays, internal conversion electrons, and characteristic X rays with the alpha-ray-excited X rays become a problem. The contribution of these radiations to the X-ray production and background were examined for ^{241}Am and ^{210}Po alpha-ray sources with various thicknesses of source window. As a result, it was proved that the largest source of background for low Z elements is conversion electrons if they are emergent and the next one is X rays or low energy gamma rays, and in comparison with these the background directly due to alpha rays is negligibly small. Some transuranium nuclides such as ^{242}Cm and ^{244}Cm whose conversion electron energies are low

were recommended as useful alpha-ray sources. For somewhat higher Z elements, L X rays from alpha-emitting nuclides and bremsstrahlung from tritium sources can be used advantageously.

To realize an industrial X-ray analyzer for low Z elements, operating characteristics of gas flow proportional counters were fully investigated. And it was recognized that they were usable for such an industrial application if only the gas gain was controlled by an appropriate means. The background pulse-height distribution characteristics inherent in detectors were studied for both proportional counters and recent semiconductor detectors. The background in proportional counters was explained by photoelectron escape and secondary electron emission from counter cathode, etc., while semiconductor detectors had large additional background components. When figure of merits relating to the capability of trace element analysis were compared between the two kinds of detectors, proportional counters with large window were advantageous over semiconductor detectors with small sensitive area, in the low energy region.

For quantitative analysis by the X-ray spectroscopy, two calibration methods were given. One is a simple semitheoretical method for thin specimens, in which troublesome preparation of the thin standard specimen is not required. The other is the derivation of linear approximation formulae for matrix-effect correction in thick specimens. These two were applied to the respective examples. Problems of accuracy, precision, and detection limit were also discussed in relation of the above two methods.

An industrial X-ray analyzer which simultaneously analyzes four main elements of low Z in cement raw material mixtures was completed using a combination of ^{210}Po alpha-ray source (together with $^{3}H/Zr$ soft X-ray source) and gas flow proportional counters. The gas gain of the proportion-

al counters was automatically controlled with an electronic feedback loop. The inside of the measuring head was constantly evacuated and the sample was exchangeable without air inflow. The analyzer was the first radioisotope X-ray analyzer to be successful in the world in analyzing multielements of low Z; in actuality, it is used routinely in a manufacturing process during more than ten years.

In applications, two typical examples were described. One was quantitative analysis of the main four components in cement raw material mixtures by using the above apparatus. A calibration formula with matrix correction for thick specimens and a simple regression calibration were compared. The latter, which is simpler, was rather better. Better accuracy and precision than those in conventional fluorescent X-ray analysis were obtained. Usage of the analyzer is advantageous over that of a conventional X-ray analyzer because of ease in the operation, rapidity in measurement, and economy in initial cost.

The other application was the analysis of airborne dust collected on membrane filters. The case is an instance of thin specimens for which analysis must be made of multielements of more than ten; the atomic numbers being adjacent together. Measurement was made with an X-ray source of ^{238}Pu and a high resolution semiconductor detector. The new simple method of calibration for thin specimens described above was successfully applied and 14 elements of sulfur through lead were simultaneously determined. This method is suitable for analysis of pollution or environmental samples, because of the simplicity, rapidity, non-destructiveness, multielement capability, and sufficient sensitivity.

Acknowledgments

The author wishes to express his sincere thanks to Professor Sakae Shimizu of Kyoto University for his suggestion of the problem, continuous encouragement, and advice in preparing the thesis. He is also grateful to Drs. Kenji Motojima, Masatoshi Kobayashi, and Shigemasa Enomoto for their encouragement and advice. He is indebted to Dr. Shoji Bando for comparison with the neutron activation analysis, Masanori Dojo for his assistance in preparation of the spectrum analysis code, and Noboru Tachikawa for his assistance in part of X-ray measurement. For the period of Ube Industries, Ltd., he would like to thank Drs. Hiroshi Imamura and Kaoru Uchida for their cooperation, valuable discussions, and giving the chance to develop an industrial X-ray analyzer.

References

1. Evans R.D.: "The Atomic Nucleus", McGraw-Hill, 628 (1967)
2. Enomoto S.: "Study on X-Ray Spectroscopic Analysis using Radioisotopes", Thesis, Nagoya Univ., 24 (1963)
3. Green M. and Cosslett V.E.: Proc. Phys. Soc., 78, 1206 (1961)
4. Whiddington R.: Proc. Roy. Soc. A, 86, 360 (1912); refered in Ref.3
5. Voyvodic L.: Armour Research Foundation Report ARF 1122-13 (1959)
6. Birkhoff R.D.: "Handbuch der Physik", 34, ed. Flügge S., Springer-Verlag, 135 (1958)
7. Enomoto S.: Ref. 2, 43
8. Merzbacher E. and Lewis H.W.: "Handbuch der Physik", 34, ed. Flügge S., Springer-Verlag, 166 (1958)
9. Hönl H.: Z. Physik, 84, 1 (1933); refered in Ref. 8, 176
10. Khandelwal G.S., Choi B.H., and Merzbacher E.: Atomic Data, 1, 103 (1969)
11. Bang J. and Hansteen J.M.: Kgl. Danske Videnskab. Selskab, Mat.-Fys. Medd., 31, No.13 (1959)
12. Brandt W., Laubert R., and Sellin I.: Phys.Rev., 151, 56 (1966); Brandt W. and Laubert R.: ibid, 178, 225 (1969)
13. Garcia J.D.: Phys.Rev., A1, 280 (1970); A1, 1402 (1970); A4, 955 (1971)
14. Garcia J.D., Fortner R.J., and Kavanagh T.M.: Rev. Mod. Phys., 45, 111 (1973)
15. Bothe W. and Fränz H.: Z. Physik, 52, 466 (1929)
16. Bühring W. and Haxel O.: ibid, 148, 653 (1957)
17. Sellers B., Hanser F.A., and Wilson H.H.: Phys.Rev., 182, 90 (1969)
18. Watson R.L., Lewis C.W., and Natowitz J.B.: Nucl. Phys. A154, 561 (1970)
19. Khan J.M. and Potter D.L.: Phys. Rev., 133, A890 (1964)
20. Ogier W.T., Lucas G.J., Murray J.S., and Holzer T.E.: ibid, 134, A1070 (1964)
21. Khan J.M., Potter D.L., Worley R.D.: ibid, 139, A1735 (1965)
22. Sterk A.A., Marks C.L., and Saylor W.P.: "Advances in X-Ray Analysis", 10, 399 (1967)
23. Der R.C., Kavanagh T.M., Khan J.M., Curry B.P., and Fortner R.J.: Phys. Rev. Letters 21, 1731 (1968)
24. Hart R.R., Reuter F.W.,III, Smith H.P.,Jr., and Khan J.M.: Phys. Rev. 179, 4 (1969)
25. Terasawa M., Inouye T., and Kamei H.: J. Phys. Soc. Japan, 29, 1394 (1970)

26. Terasawa M., Tamura T., Kamada H.: ibid, 33, 1420 (1972)
27. The Radiochemical Centre: "Radioactive Products 1969/1970", 144 (1969)
28. Dewey R.D., Mapes R.S., and Reynolds T.W.: "Progress in Nuclear Energy Series 9, Analytical Chemistry", 9, eds. Elion H.A. and Stewart D.C., Pergamon Press, 321 (1969)
29. McMaster W.H., Ker Del Grande N., Mallet J.H., and Hubbel J.H.: UCRL-50174 Sec. II , Rev. 1 (1969)
30. Whaling W.: "Handbuch der Physik", 34, ed. Flügge S., Springer-Verlag, 193 (1958)
31. Evans R.D.: Ref. 1, 652
32. Walters D.L. and Bhalla C.P.: Phys. Rev., A3, 519 (1971)
33. Wolfson J.L., Park J.J.: Can. J. Phys., 42, 1387 (1964)
34. Lederer C.M., Hollander J.M., and Perlman I.: "Table of Isotopes", 6th edition, John Wiley & Sons (1968)
35. Birks L.S., Seebold R.E., Batt A.P., and Grosso J.S.: J.Appl. Phys., 35, 2578 (1964)
36. Katz L. and Penfold A.S.: Rev. Mod. Phys., 24, 28 (1952)
37. Rubinson W. and Bernstein W.: Phys. Rev.: 86, 545 (1952)
38. Folkmann F., Gaarde C., Huus T., and Kemp K.: Nucl. Instr. & Meth., 116, 487 (1974)
39. Folkmann F., Borggreen J., and Kjeldgaard A.: ibid, 119, 117 (1974)
40. Tominaga H. and Enomoto S.: "Proc. 8th Japan Conf. on Radioisotopes", Maruzen, 257 (1968)
41. Ref. 27, 165
42. The Radiochemical Centre: "Radioactive Low Energy Photon Sources", Technical Bulletin 72/6, 10 (1972)
43. Tanemura T.: Jap. J. Appl. Phys., 5, 51 (1966)
44. Imamura H., Uchida K., and Tominaga H.: "Proc. 5th Japan Conf. on Radioisotopes", 3, Maruzen, 164 (1964)
45. Tominaga H. and Uchida K.: "Proc. 6th Japan Conf. on Radioisotopes", Maruzen, 167 (1965)
46. Campbell A.J.: Brit. J. Appl. Phys., 14, 221 (1963)
47. West D.: Prog. in Nucl. Phys. 3, 18 (1953)
48. Fergason L.: Rev. Sci. Instr., 37, 964 (1966)
49. Spielberg N.: ibid, 38, 291 (1967)
50. Goulding F.S., Jaklevic J.M., Jarrett B.V., and Landis D.A.: "Advances in X-Ray Analysis", 15, 470 (1972)

51. Jaklevic J.M. and Goulding F.S.: IEEE Trans. Nucl. Sci., NS-19, (3), 384 (1972)
52. Currie L.A.: Anal. Chem., 40, 586 (1968)
53. Cooper J.A.: Nucl. Instr. & Meth., 82, 273 (1970)
54. Tominaga H.: ibid, 114, 65 (1974)
55. Giauque R.D. and Jaklevic J.M.: "Advances in X-Ray Analysis", 15, 164 (1972)
56. Tanemura T. and Suita H.: Radioisotopes, 21, 641 (1972)
57. Dewey R.D.: Ref. 28, 309
58. Rogers V.C.: Anal. Chem.: 42, 807 (1970)
59. Tominaga H., Dojyo M., and Tanaka M.: Nucl. Instr. & Meth., 98, 69 (1972)
60. Imamura H., Uchida K., and Tominaga H.: Radioisotopes, 14, 286 (1965)
61. Uchida K., Tominaga H., Imamura H., and Miwa H.: "Radioisotope Instruments in Industry and Geophysics", I, IAEA, 113 (1966)
62. Dolby R.M.: Proc. Phys. Soc. London, 73, 81 (1959)
63. Imamura H., Uchida K., and Tominaga H.: Radioisotopes, 13, 355 (1964)
64. De Waard H.: Nucleonics, 13, (7), 36 (1955)
65. Rhodes J.R., Pradzynski A., Sieberg R.D., and Furuta T.: "Applications of Low Energy X- and Gamma Rays", ed. Ziegler C.A., Gordon and Breach Science Publishers, 317 (1971)
66. Imamura H., Uchida K., and Tominaga H.: Kogyo Kagaku Zashi, 67, 1827 (1964)
67. Imamura H., Uchida K., and Tominaga H.: "X-Ray Analysis, Japan", 2, Nankodo, 99 (1965)
68. Andermann G.: Anal. Chem., 33, 1689 (1961)

Table 1 Fractions of emergent X and gamma rays of the ^{241}Am alpha-ray source, measured with a Si(Li) detector. The fractions are adjusted in such a manner that the value of 59.56 keV gamma ray becomes 0.359*; only the lower energy X and gamma rays are considered to be attenuated significantly in the window and the source itself.

Radiation	Energy (keV)	Fraction measured (per disintegration)	Fraction in thin source * (per disintegration)
Np Mα	3.26	0.015	
Ni Kα	7.48	0.011	
Pt Lα	9.44	0.0077	
Pt Lβ	11.07	0.0087	
Np Ll	11.89	0.0053	0.008
Np Lα	13.95	0.089	0.135
Np Lβ	17.74	0.149	0.184
Np Lγ	20.77	0.039	0.050
γ	26.36	0.021	0.025
γ	59.56	0.359	0.359

* Magnusson L.B.: Phys.Rev., 107, 161 (1957)

Table 2 Experimental thick target yield of K X rays produced by alpha particles (photons per alpha particle per steradian).

Element	Detector	$\bar{E}_0$ = 3.93 MeV	$\bar{E}_0$ = 2.97 MeV	$\bar{E}_0$ = 1.88 MeV
C	a	0.178±0.018(-1)	0.191±0.019(-1)	0.164±0.016(-1)
F*	a	0.143±0.014(-1)	o.118±0.012(-1)	0.584±0.058(-2)
Mg	a	0.611±0.061(-2)		
	b	0.670±0.067(-2)	0.325±0.033(-2)	0.783±0.094(-3)
Al	b	0.456±0.046(-2)	0.204±0.020(-2)	0.444±0.054(-3)
Si*	b	0.286±0.029(-2)		
S	b	0.167±0.017(-2)	0.610±0.067(-3)	0.99 ±0.23 (-4)
Cl*	b	0.114±0.013(-2)		
Ca*	b	0.538±0.097(-3)		
Ti	b	0.302±0.039(-3)	0.50 ±0.35 (-4)	0.30 ±0.39 (-4)

Detector a : polypropylene window.

Detector b : Mylar window.

* : the yield expected for a pure element target, which was calculated from the experimental yield for a compound by multiplying the factor: 2.72, 3.00, 2.10, and 3.04 for teflon, SiO_2, NaCl, and $CaCO_3$, respectively.

Table 3 Calculation of K-shell ionization cross sections from experimental data of thick target yields.

Element	E_α (MeV)	Y (X rays /sr.α)	$\frac{dY}{dE}$ (X rays/ sr.α.MeV)	$\frac{dE}{dR}$ (MeV.cm^2 /mg)	σK (cm^2)
C	2	0.169(-1)	0.401(-2)	0.145(1)	0.616(-17)
μ = 3140 cm^2/g	3	0.191(-1)	0.250(-3)	0.110(1)	0.630(-17)
ω_i = 0.0024	4	0.176(-1)	-0.262(-2)	0.936(0)	0.553(-17)
Mg	2	0.980(-3)	0.161(-2)	0.108(1)	0.367(-19)
μ = 453 cm^2/g	3	0.334(-2)	0.301(-2)	0.862(0)	0.690(-19)
ω_i = 0.0301	4	0.698(-2)	0.403(-2)	0.762(0)	0.105(-18)
Al	2	0.540(-3)	0.918(-3)	0.102(1)	0.161(-19)
μ = 378 cm^2/g	3	0.211(-2)	0.222(-2)	0.824(0)	0.372(-19)
ω_i = 0.0398	4	0.474(-2)	0.274(-2)	0.713(0)	0.530(-19)
S	2	0.125(-3)	0.233(-3)	0.982(0)	0.211(-20)
μ = 228 cm^2/g	3	0.633(-3)	0.819(-3)	0.806(0)	0.657(-20)
ω_i = 0.0818	4	0.177(-2)	0.142(-2)	0.689(0)	0.113(-19)

Table 4 Background per cent due to various matrix elements to K X rays of pure sample of the element to be measured, within FWHM of K_α peak.
Values in parentheses are of the case where the L X rays from the ^{241}Am source are excluded by a nickel filter on the source.

Element to be measured	Atomic number	Matrix element Al	Fe	Mo	Sb
Ti	22	1.5 (7.4)	6.0 (9.0)	4.1 (17.4)	10.4 (35.3)
Fe	26	0.94 (3.4)	—	1.6 (7.0)	1.4 (7.9)
Zn	30	0.54 (1.9)	0.52 (1.2)	1.2 (4.6)	1.1 (5.6)
Mo	42	2.7 (0.90)	1.0 (0.68)	—	4.1 (3.9)

Table 5 Ratio of the valley background to the full energy peak count, r_B, for E_1 = 36 keV and E_2 = 60 keV (^{241}Am).

Detector No.	Type (Manufacturer)	r_B with collimation	r_B without collimation
1. Si(Li) 80 mm^2 × 2 mm t	inverse-T (TMC)	0.086	0.128
2. Si(Li) 80 mm^2 × 3 mm t	inverse-T (KEVEX)	0.058	0.109
3. Si(Li) 30 mm^2 × 3.2mmt	unknown (ORTEC)	0.120	
4. Si(Li) 20 mm^2 × 4 mm t	(JAERI)	0.089	0.108
5. Ge(Li) 200 mm^2 × 4.67mmt	unknown (ORTEC)	0.0064	0.064
6. Ge(Li) 600 mm^2 × 7.0mmt	unknown (ORTEC)	0.017	0.081

Table 6 Figure of merit of detectors.
Parentheses indicate data with collimation.

Detector	$i_B(E_1)^*$ ($\times 10^{-4}$)	$i_p(E_1)^{**}$	$\frac{i_p(E_1)}{i_B(E_1)}$	$\Gamma(E_1)^{***}$ (keV)	FOM (S = 1)
E_1 = 36 keV, E_2 = 60 keV (^{241}Am)					
1. Si(Li) 80 mm^2 × 2 mm	1.15 (0.768)	0.240	2090 (3130)	0.330	38.9 (47.7)
2. Si(Li) 80 mm^2 × 3 mm	1.41 (0.760)	0.331	2350 (4360)	0.330	48.5 (66.1)
3. Si(Li) 30 mm^2 × 3.2 mm	(1.66)	0.348	(2100)	0.330	(47.0)
4. Si(Li) 20 mm^2 × 4 mm	1.82 (1.50)	0.408	2242 (2720)	0.330	52.7 (58.0)
5. Ge(Li) 200 mm^2 × 4.67 mm	10.0 (1.00)	0.985	985 (9850)	0.230	64.9 (205)
6. Ge(Li) 600 mm^2 × 7.0 mm	13.5 (2.64)	0.985	730 (3731)	0.230	55.9 (126)
7. Ar(CH_4) 1 atm 47 mm	0.408 (0.286)	0.00796	195 (278)	2.68	0.760 (0.908)
E_1 = 13 keV, E_2 = 22 keV (^{109}Cd)					
4. Si(Li)	17.2	0.992	577	0.215	51.6
7. Ar(CH_4)	3.79 (2.03)	0.199	525 (980)	1.63	8.0 (11.0)
8. Xe(CH_4) 1 atm 43 mm	5.70	0.848	1480	1.63	27.7

* : valley background efficiency per unit energy interval.

** : theoretical peak efficiency.

*** : theoretical FWHM; for Si(Li), energy per electron-hole pair = 3.8 eV, Fano factor = 0.13, and electronic noise = 100 eV ; for Ge(Li), energy per electron-hole pair = 2.9 eV, Fano factor = 0.08, and electronic noise = 76 eV ; for proportional counters, FWHM = $0.448\sqrt{E}$ (keV).

Table 7 Calibration coefficients for matrix correction, a_{ij}.

Counting channel No.		a_{io}	Fe_2O_3 a_{i1}	CaO a_{i2}	SiO_2 a_{i3}	Al_2O_3 a_{i4}	MgO a_{i5}	Ig. loss a_{i6}
1.	Fe-ch.	103.82	17.56 ±0.91	-0.70 ±0.08	-0.01 ±0.12	-0.09 ±0.12	-0.11 ±0.12	-0.03 ±0.12
2.	Ca-ch.	34.37	-0.18 ±0.05	1.48 ±0.16	-0.53 ±0.05	-0.45 ±0.05	-0.44 ±0.05	0.32 ±0.05
3.	Si-ch.	3.44	-0.48 ±0.20	-0.19 ±0.13	6.93 ±0.63	1.12 ±0.31	-0.54 ±0.23	0.60 ±0.19
4.	Al-ch.	-7.28	-0.77 ±0.11	-0.08 ±0.07	5.52 ±0.20	8.19 ±0.89	1.78 ±0.22	0.75 ±0.11
5.	Mg-ch.	34.49	-0.85 ±0.24	0.47 ±0.15	2.44 ±0.38	15.95 ±0.57	26.51 ±1.26	0.69 ±0.23
6.	Al-ch.	11.14	-0.49 ±0.27	0.07 ±0.18	0.83 ±0.48	23.63 ±2.28	3.71 ±0.55	0.48 ±0.27
7.	Al-ch.	22.12	-0.34 ±0.37	0.13 ±0.24	0.24 ±0.64	21.24 ±3.05	10.20 ±0.73	0.57 ±0.37
8.	Mg-ch.	41.62	-0.33 ±0.38	0.85 ±0.24	0.76 ±0.60	31.76 ±0.90	31.37 ±2.00	0.67 ±0.36
9.	Mg-ch.	32.44	-0.47 ±0.27	1.44 ±0.17	-0.44 ±0.42	13.63 ±0.64	29.17 ±1.42	0.83 ±0.25

Table 8 Calibration coefficients for matrix correction, b_{ij}.

A. Using only the counter without filter.

Component	Constant term b_{io}	Fe-ch. No. 1 b_{i1}	Ca-ch. No. 2 b_{i2}	Si-ch. No. 3 b_{i3}	Al-ch. No. 4 b_{i4}	Mg-ch. No. 5 b_{i5}
Fe_2O_3	-0.0717	0.0573	0.0271	0.0014	0.0006	0.0007
CaO	-0.3394	0.0091	0.6820	0.0405	0.0096	0.0115
SiO_2	-0.0502	0.0037	0.0199	0.1709	-0.0342	0.0061
Al_2O_3	0.0068	0.0031	-0.0016	-0.1278	0.1664	-0.0138
MgO	-0.0153	-0.0005	-0.0121	0.0605	-0.0971	0.0453

B. Using both the counters with and without filter.

	b_{io}	No. 1 b_{i1}	No. 2 b_{i2}	No. 3 b_{i3}	No. 6 b_{i4}	No. 8 b_{i5}
Fe_2O_3	-0.0716	0.0573	0.0270	0.0021	-0.0002	0.0006
CaO	-0.3373	0.0085	0.6802	0.0513	-0.0042	0.0109
SiO_2	-0.0464	0.0039	0.0188	0.1468	-0.0123	0.0043
Al_2O_3	-0.0075	0.0012	0.0010	-0.0053	0.0508	-0.0061
MgO	0.0021	-0.0009	-0.0196	0.0005	-0.0510	0.0376

Table 9 Results of quantitative analysis of cement raw material mixtures.

Deviation of the weight per cent from the chemical analysis (standard deviation)	Fe_2O_3 (%)	CaO (%)	SiO_2 (%)	Al_2O_3 (%)
Multiple regression calibration using b_{ij}	0.050	0.36 0.30*	0.19	0.086
Simple regression calibration	0.045	0.16	0.18	0.095

Deviation of the count ratio from the calculated one (standard deviation)	Fe-ch.	Ca-ch.	Si-ch.	Al-ch.
Multiple regression calibration using a_{ij}	0.0082	0.0044	0.0120	0.0202
Simple regression calibration	0.0092	0.0045	0.0120	0.0173

Main calibration coefficient	Fe-ch.	Ca-ch.	Si-ch.	Al-ch.
Multiple regression, a_{ii}	17.56	1.48	6.93	23.63
Simple regression, A_i	20.23	2.81	6.53	18.27

Statistical counting error for 10 min (relative standard deviation)	Fe-ch.	Ca-ch.	Si-ch.	Al-ch.
	0.0051	0.0015	0.0042	0.0093
Count rate (cpm)	3800	46000	5800	1150

* : corrected for ignition loss.

Table 10 Analysis of airborne particulates in the specimen of Fig. 49. Substruction of the peak count in the blank filter spectrum was not yet made.

Element	$I_i(m_i)$ (counts /2000s)	$I_i(\infty)$ (cps)	$\mu^i(i)$ (cm^2/g)	C_i	m_i determined ($\mu g/cm^2$)
S	48.8 ± 10.0	4.04	290	0.658	32. ± 7.
Cl	12.9 ± 11.4	7.51	250	0.740	5. ± 4.
K	124.5 ± 7.1	21.6	216	0.851	16. ± 1.
Ca	344.0 ± 9.6	38.0	201	0.887	25.4 ± 0.7
Ti	70.5 ± 5.8	86.7	175	0.932	2.5 ± 0.2
V	49.8 ± 5.1	118.	169	0.947	1.3 ± 0.1
Cr	22.7 ± 3.8	157.	160	0.958	0.47 ± 0.08
Mn	57.9 ± 4.6	199.	153	0.966	0.99 ± 0.08
Fe	1870. ± 17.	241.	148	0.973	26.9 ± 0.3
Ni	153.6 ± 6.3	334.	145	0.981	1.62 ± 0.07
Cu	47.4 ± 4.3	386.	145	0.984	0.43 ± 0.04
Zn	254.9 ± 6.4	431.	148	0.987	2.03 ± 0.05
Br	130.7 ± 30.5	626.	175	0.993	0.60 ± 0.14
Pb	299.0 ± 18.6	137.	309	0.991	3.6 ± 0.2

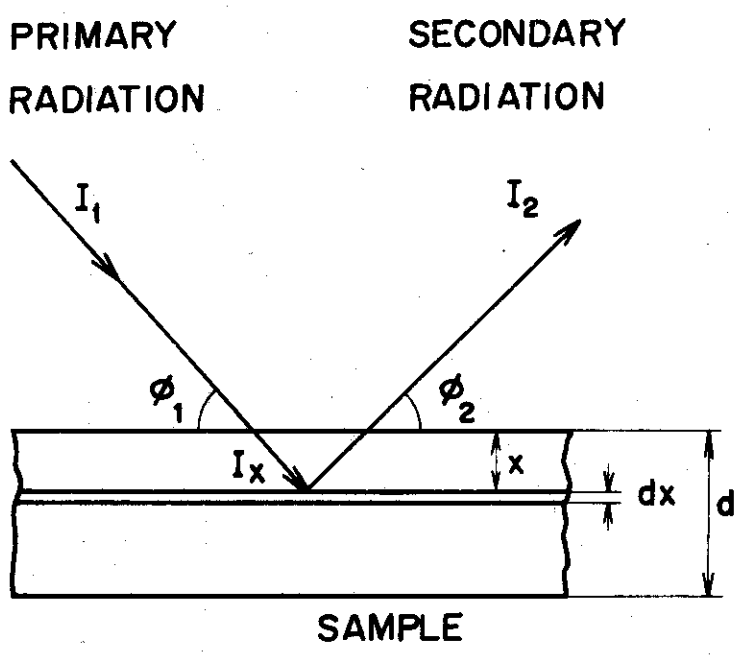

Fig. 1 Geometry of characteristic X-ray production.

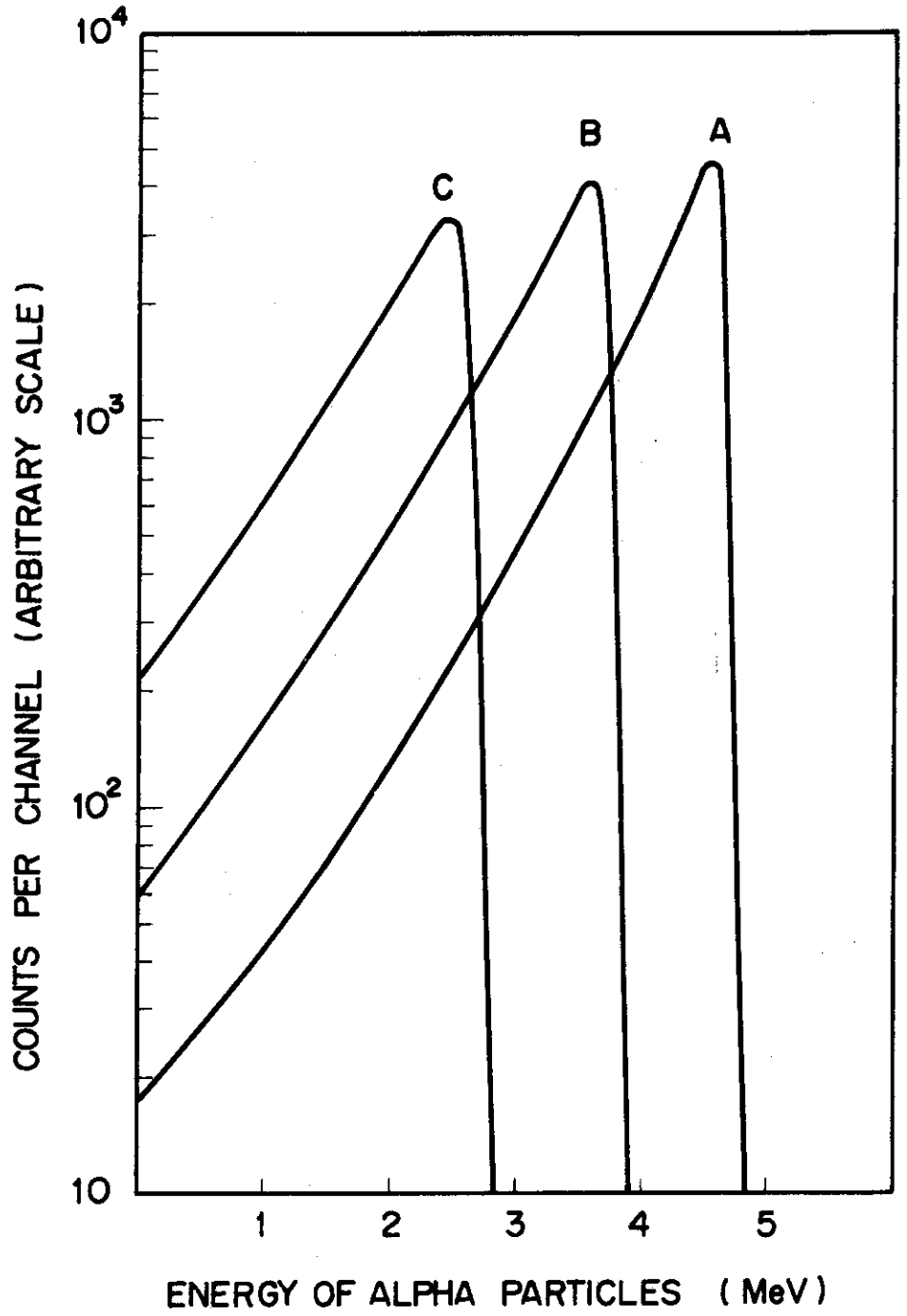

Fig. 2 Energy spectra of alpha particles from the ^{241}Am source with and without Mylar film absorber. A : no absorber, B : one sheet of Mylar, and C : two sheets of Mylar.

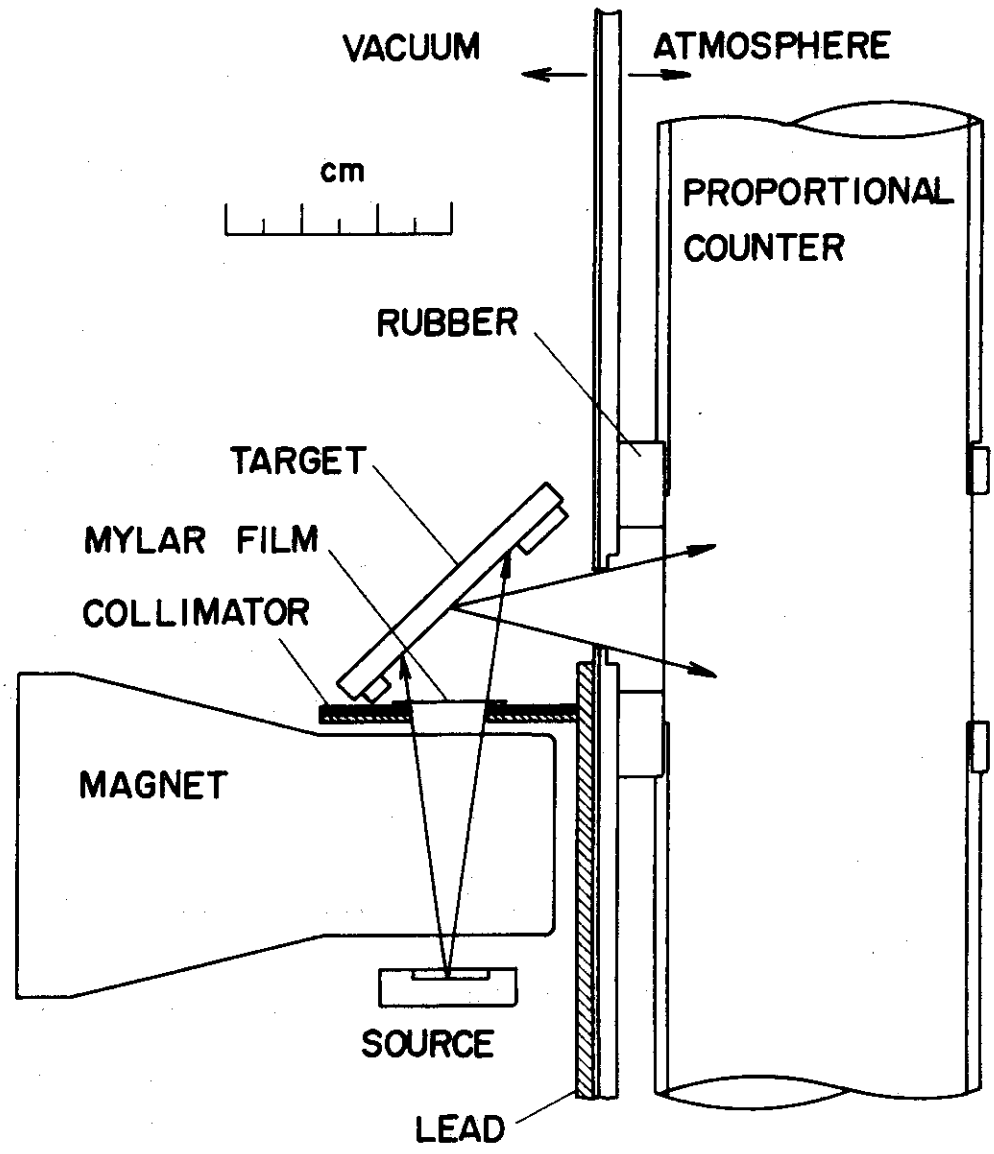

Fig. 3 Experimental layout for the yield measurement of characteristic X rays excited by alpha particles.

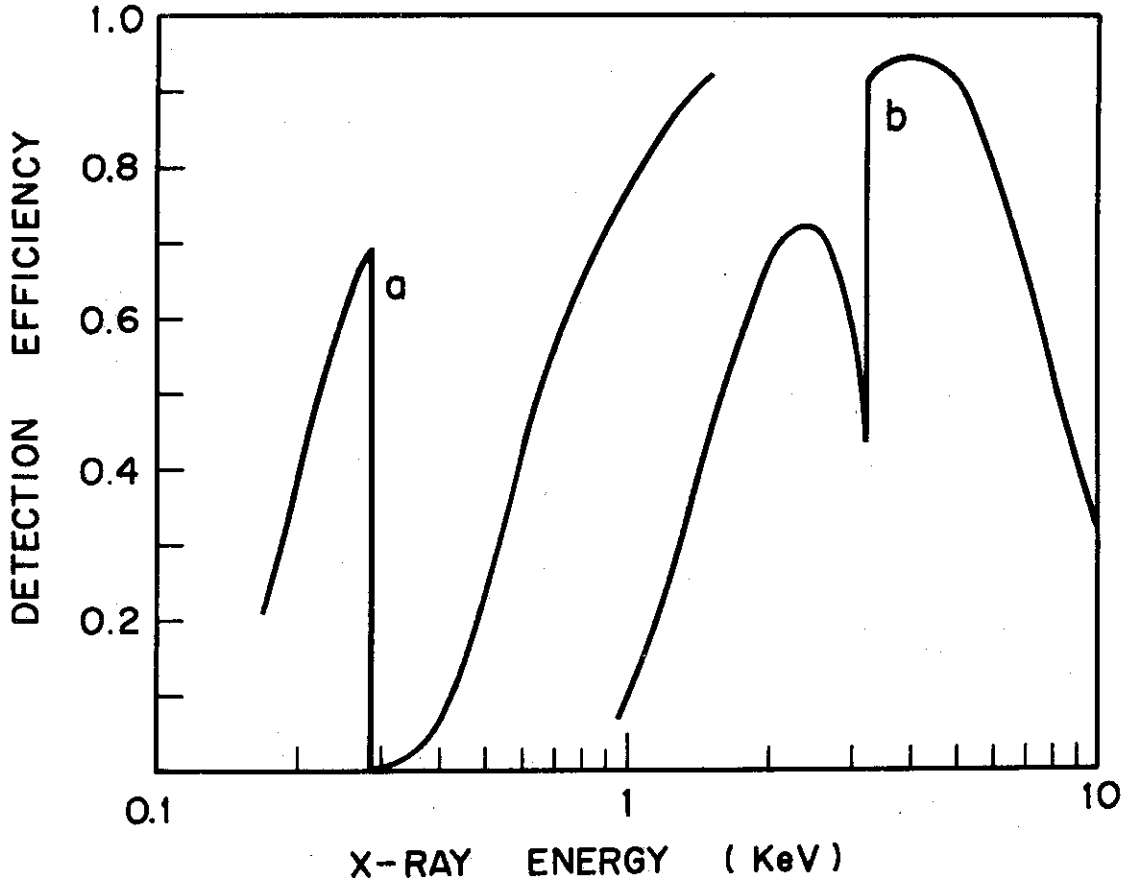

Fig. 4 Detection efficiency of the proportional counter with a polypropylene window (a) or a Mylar window (b).

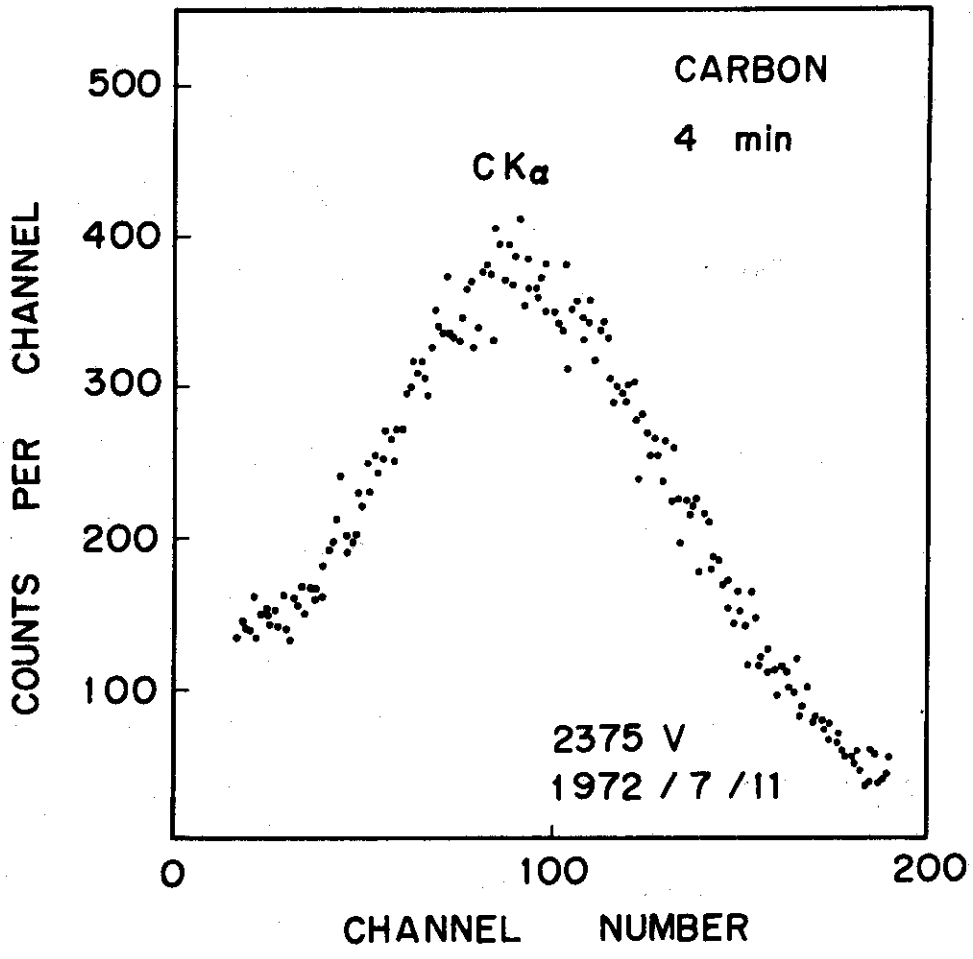

Fig. 5 Pulse-height spectrum of carbon K X rays from a graphite thick target excited by alpha particles of the ^{241}Am source without absorber.

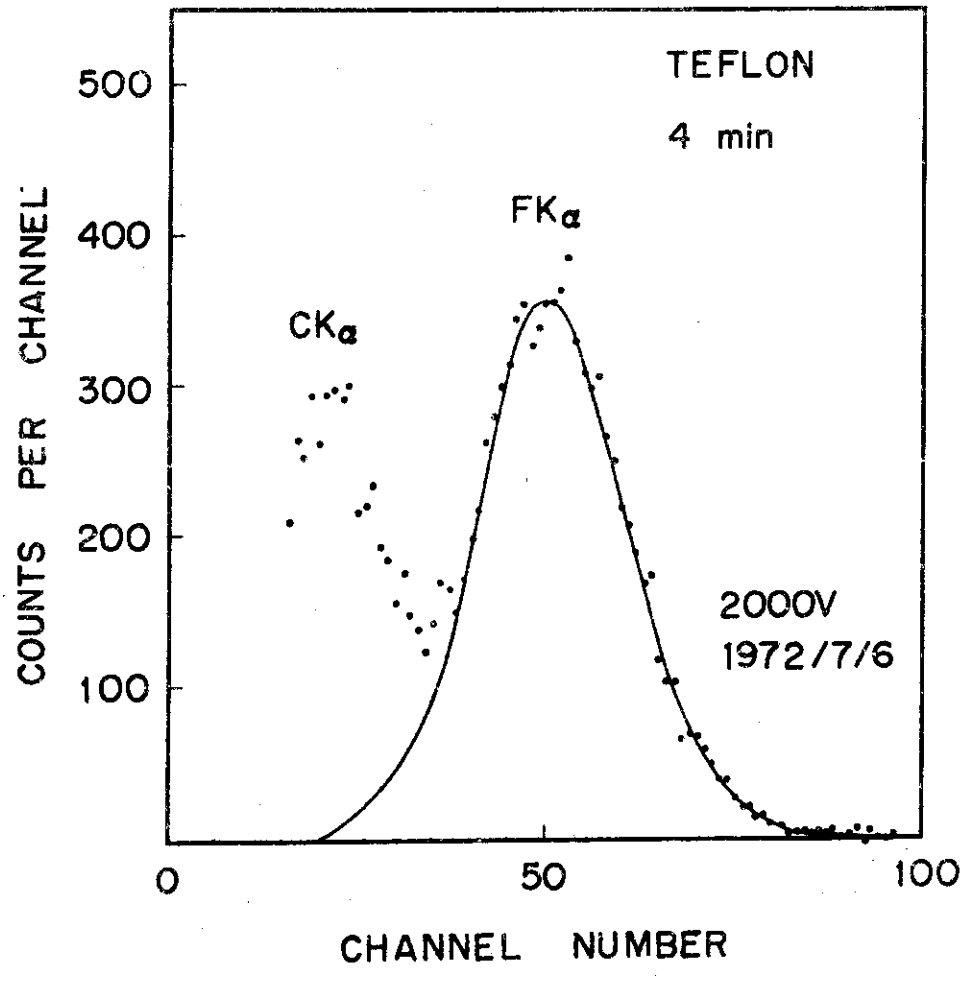

Fig. 6 Pulse-height spectrum of fluorine and carbon X X rays from a teflon thick target excited by alpha particles of the ^{241}Am source without absorber.

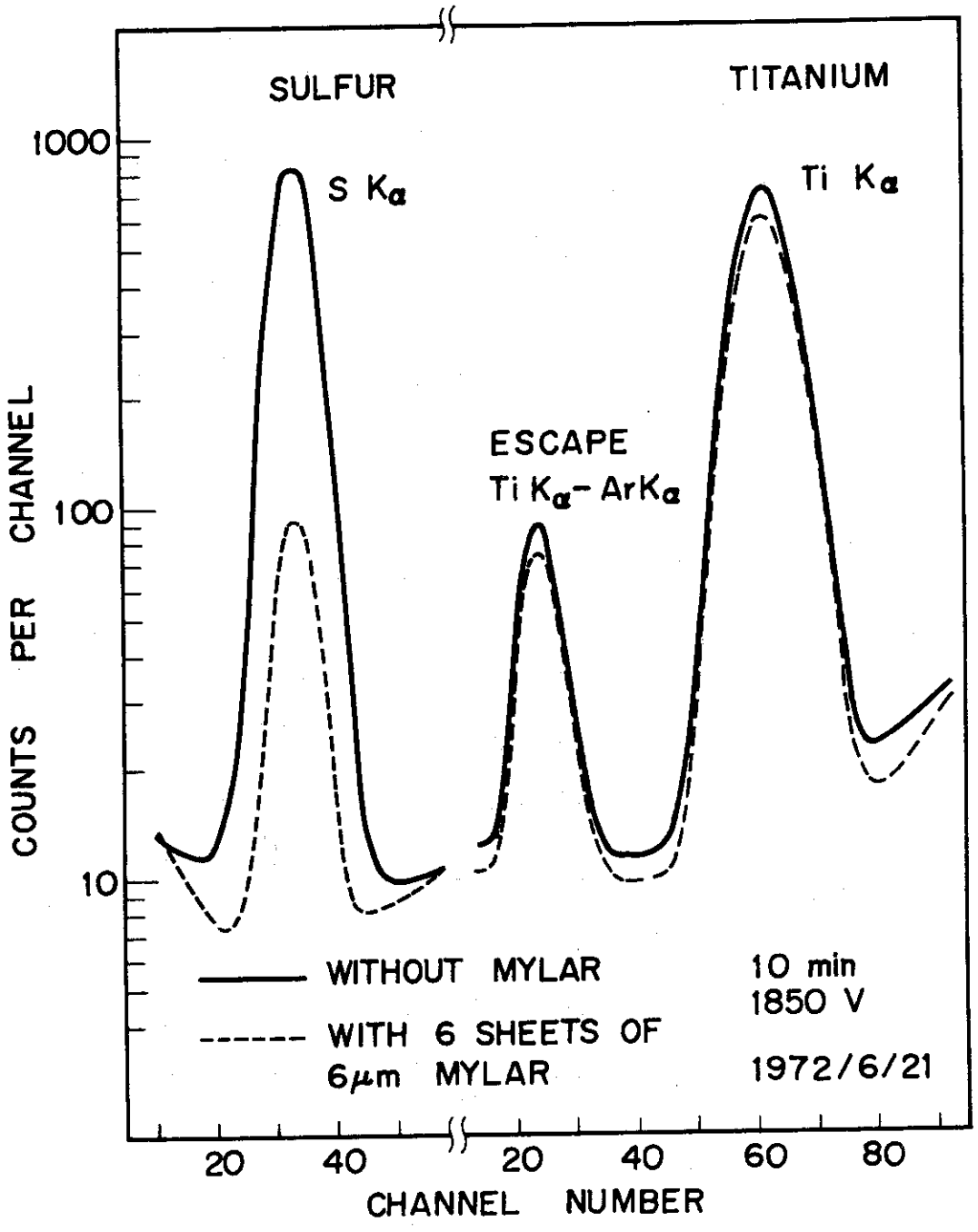

Fig. 7 Pulse-height spectra of sulfur and titanium K X rays excited by the ^{241}Am radiations.

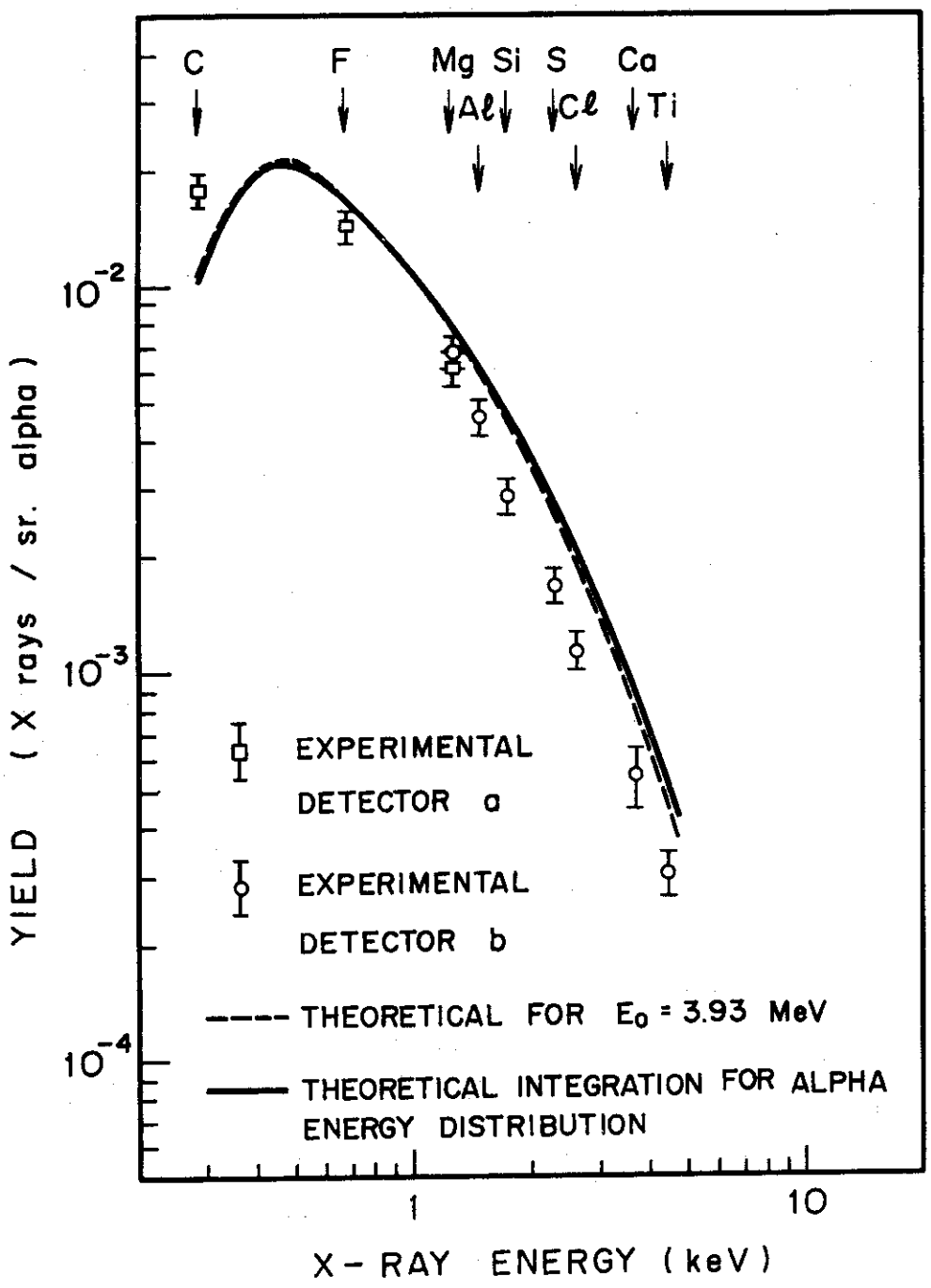

Fig. 8 Experimental thick target yields of characteristic K X rays excited by alpha particles of $\bar{E}_o$ = 3.93 MeV, compared with theoretical calculation by the Born approximation.

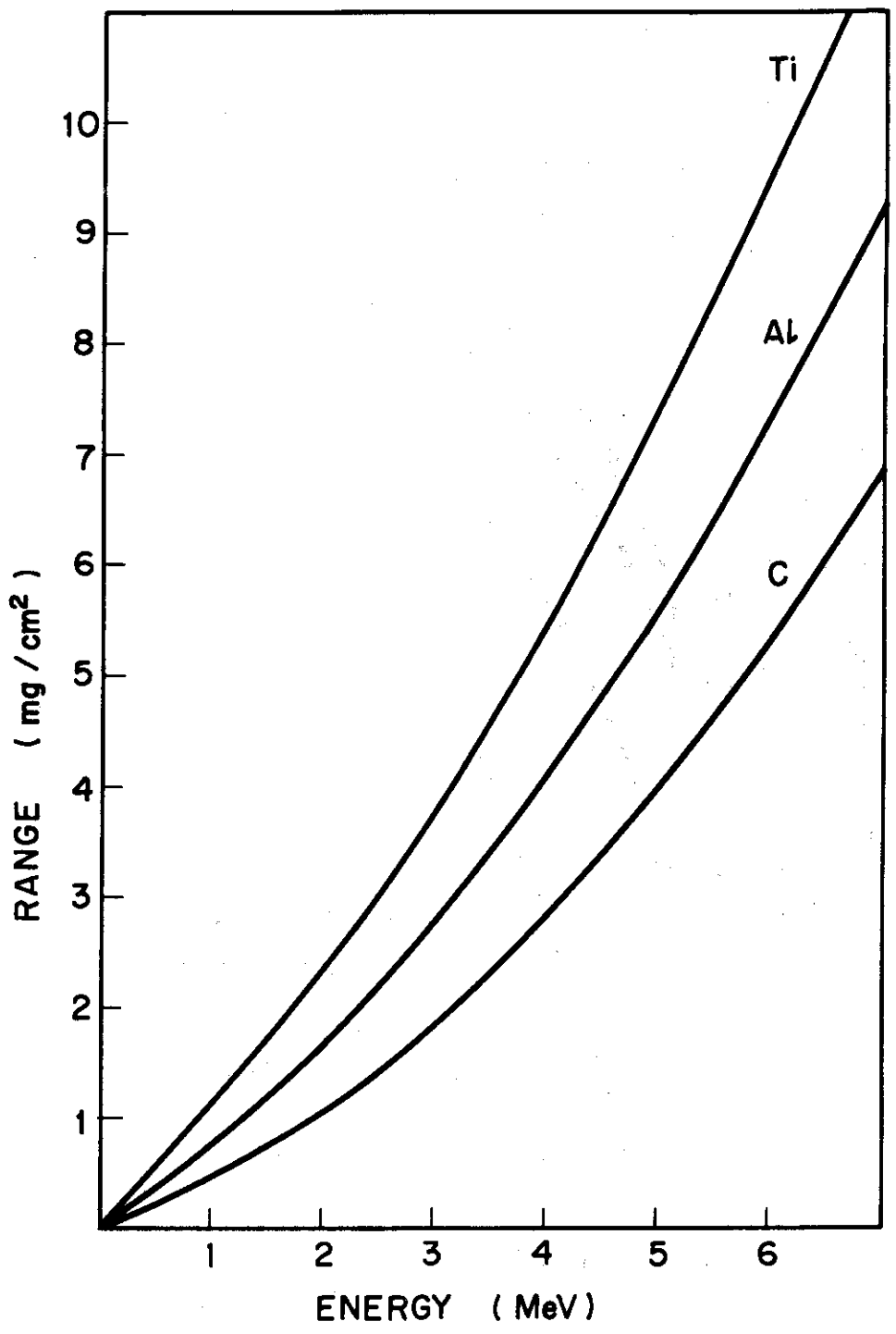

Fig. 9 Range-energy relations for alpha particles.

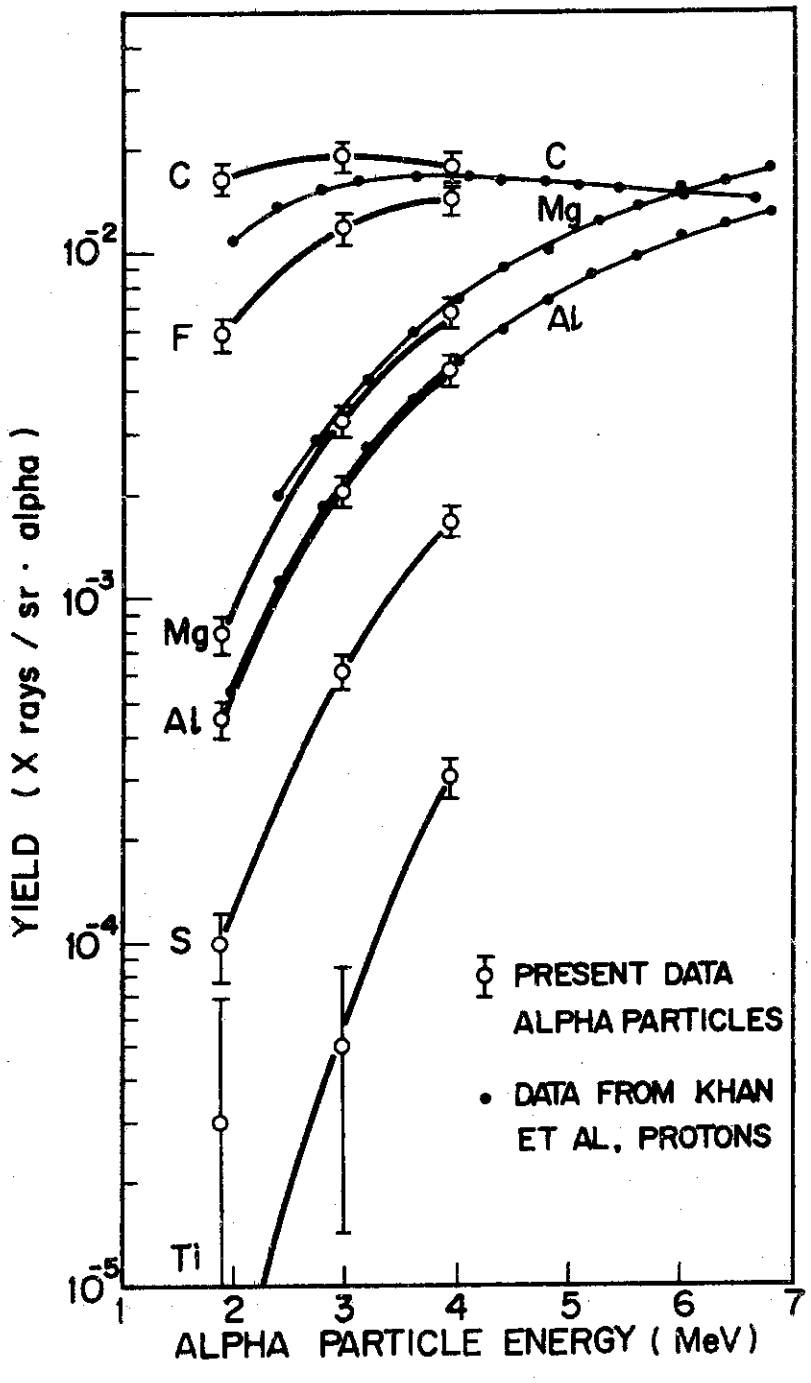

Fig. 10 Plot of experimental thick target yields of alpha-excited X rays versus alpha energy, compared with proton-excited X rays.

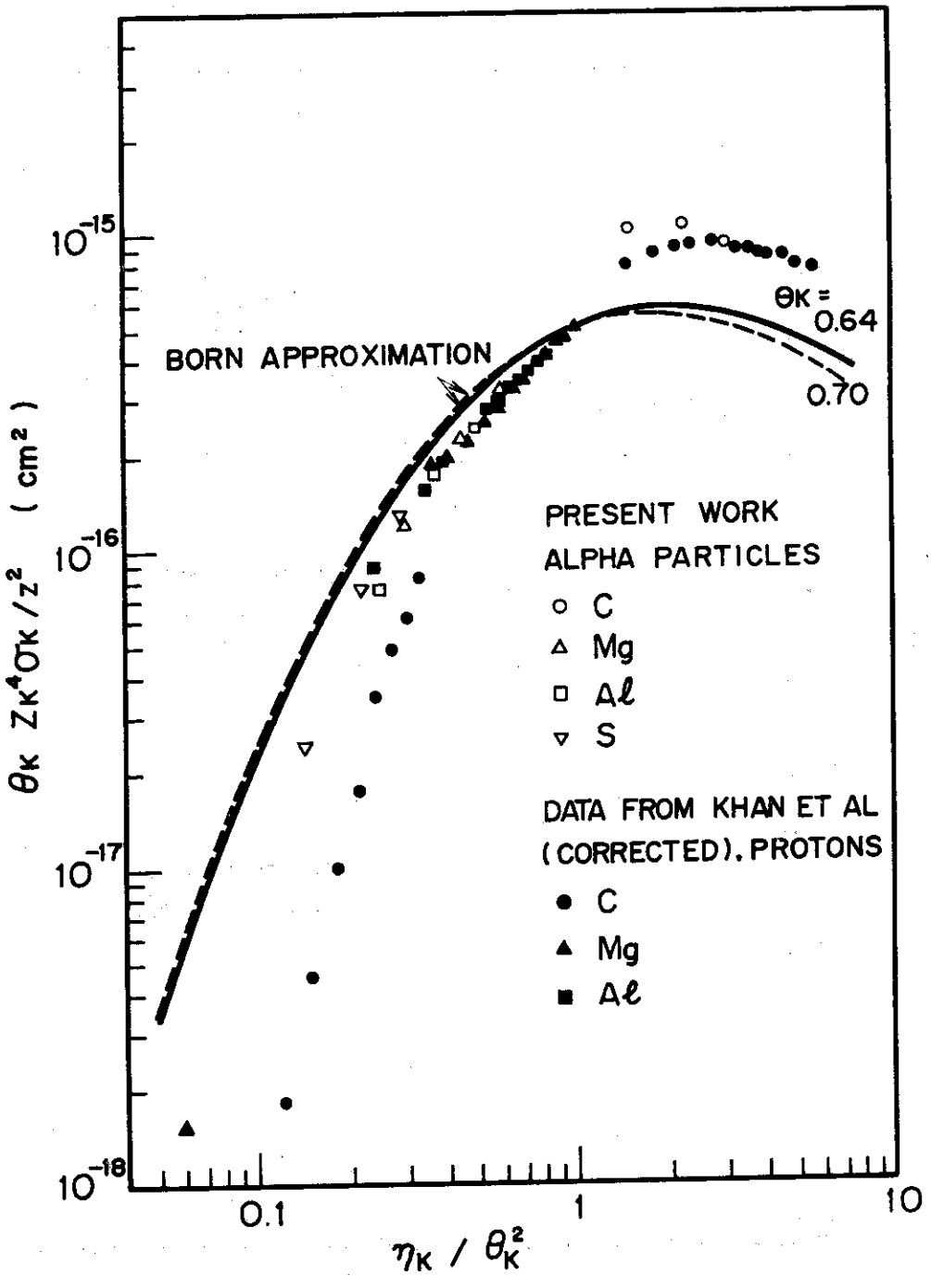

Fig. 11 Experimental K-shell ionization cross sections compared with previous data by proton impact and a theory based on the Born approximation.

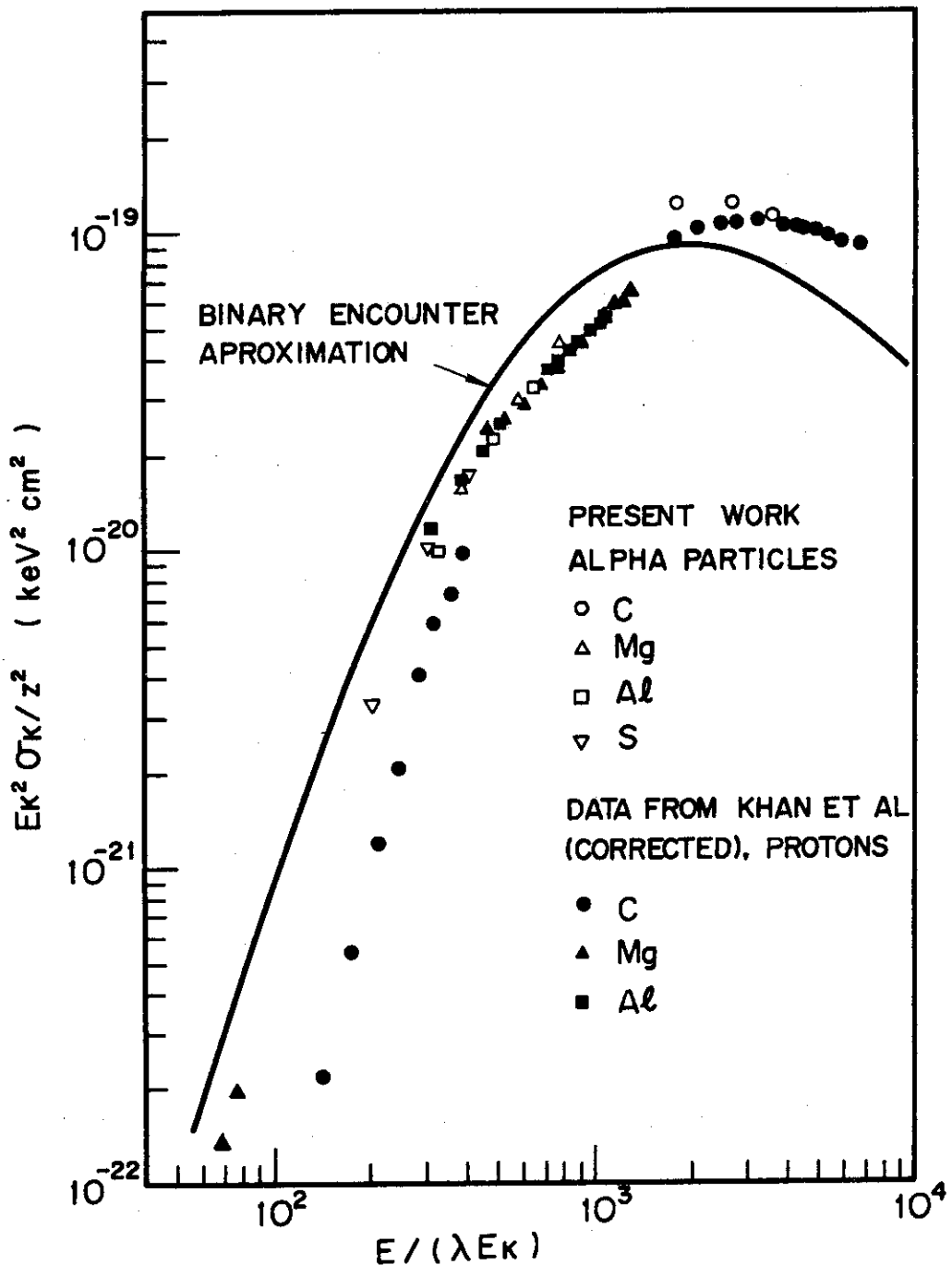

Fig. 12 Experimental K-shell ionization cross sections compared with previous data by proton impact and a theory based on the binary-encounter approximation.

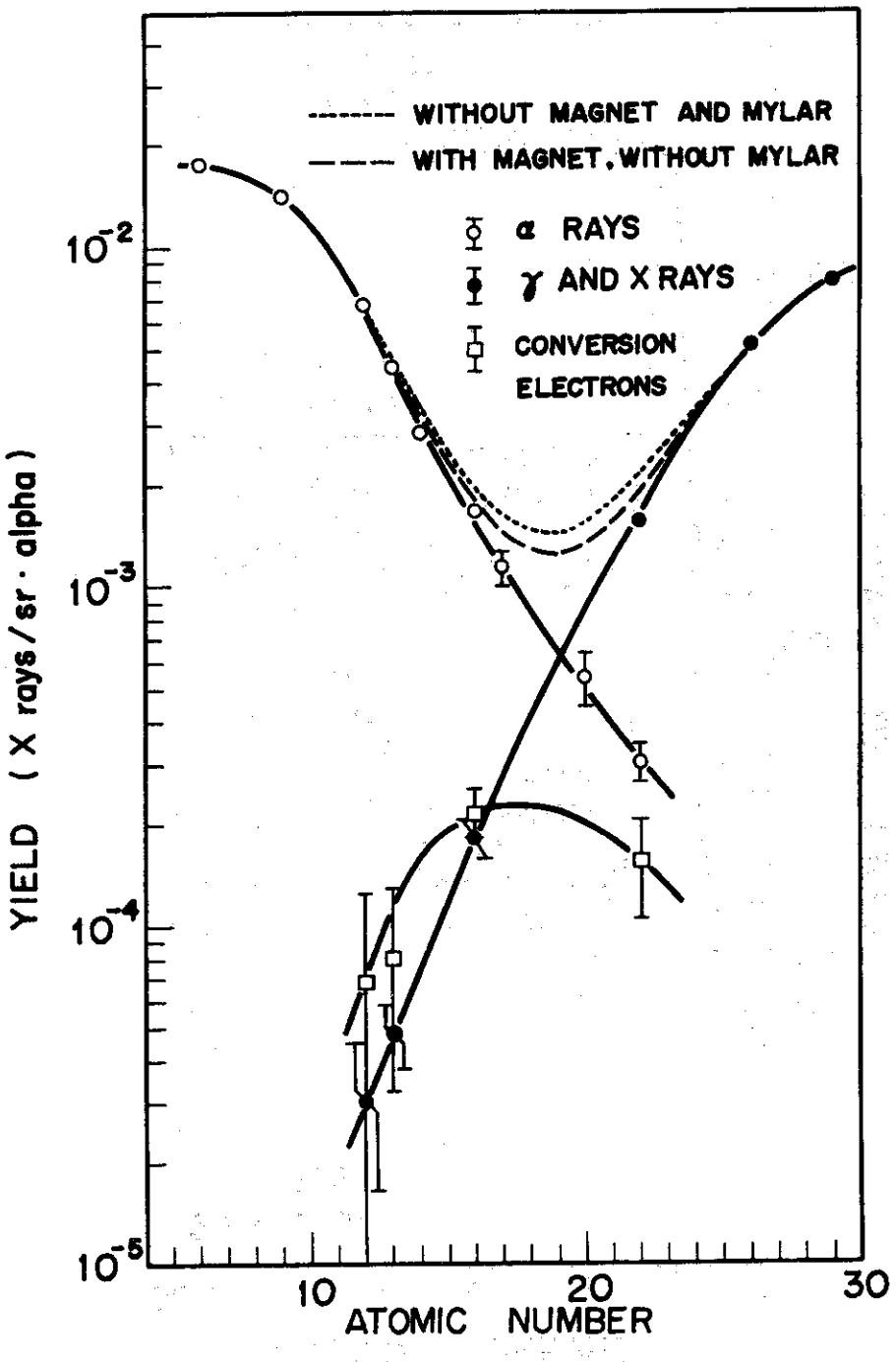

Fig. 13 Intensity comparison of characteristic X rays produced by alpha particles, photons, and conversion electrons from the ^{241}Am source. Data without error bar have errors of 10 %.

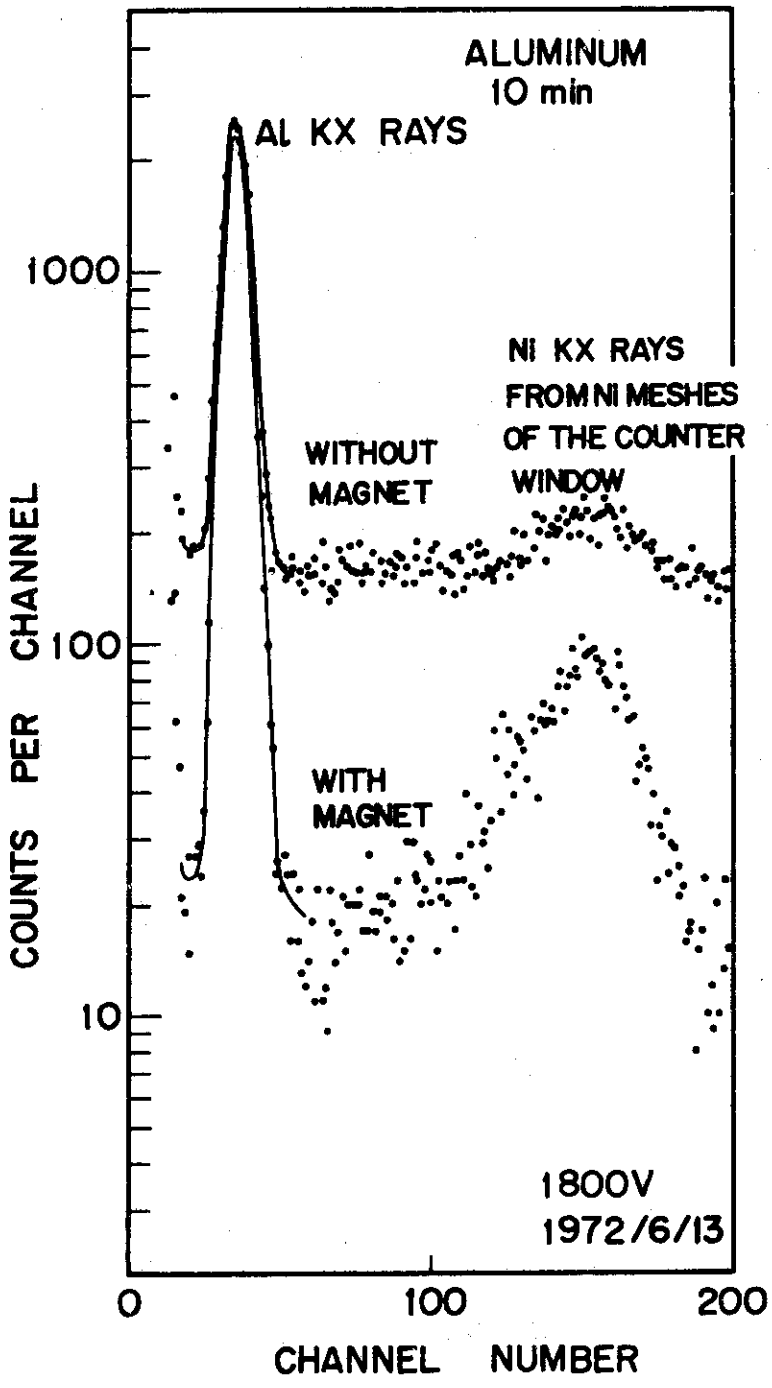

Fig. 14 Pulse-height spectra of X rays from an aluminum target excited by radiations of the ^{241}Am alpha-ray source with and without a magnet.

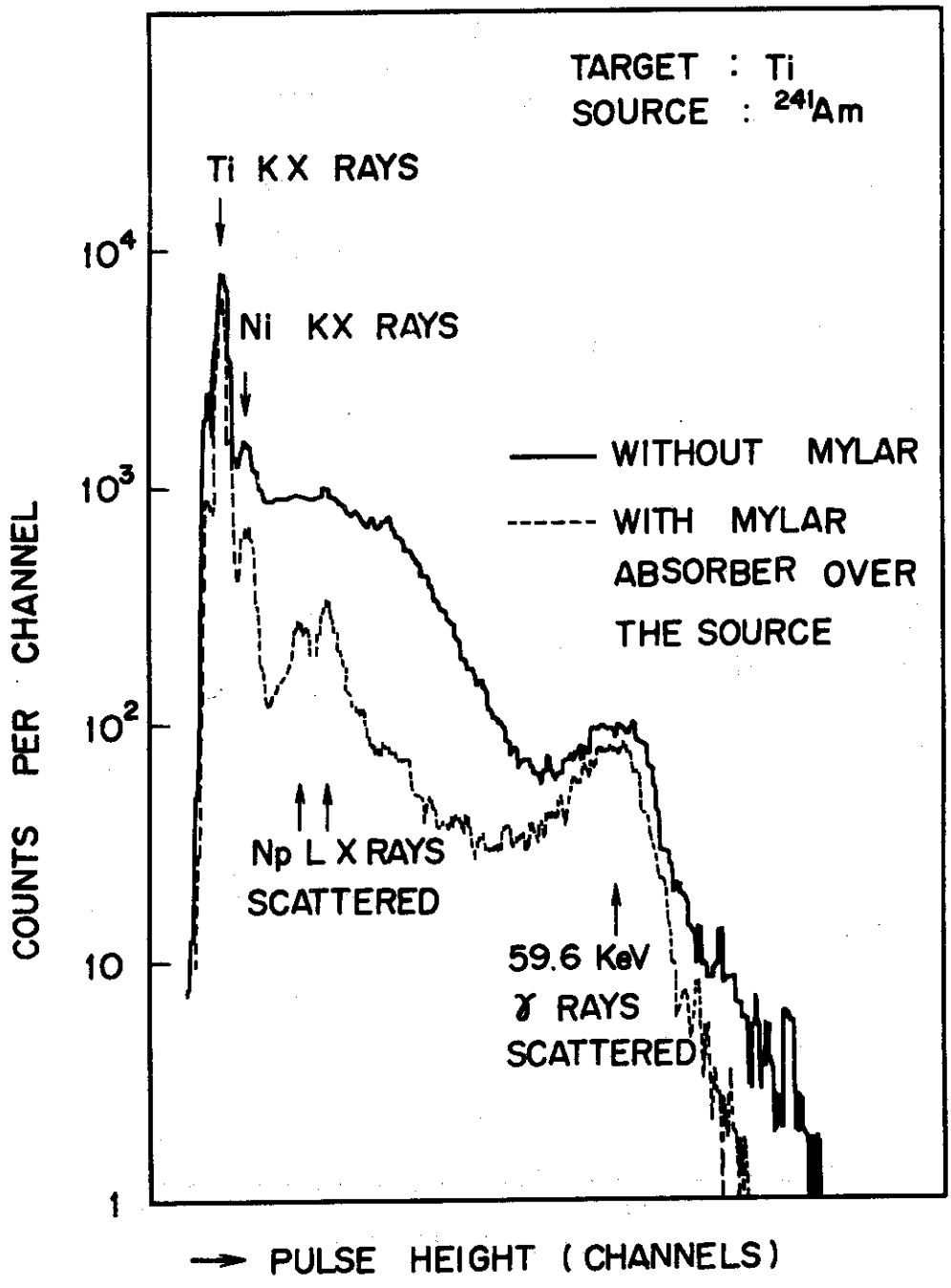

Fig. 15 Pulse-height spectra of excited X rays and background in the case of the ^{241}Am alpha-ray source without magnet, with and without a Mylar film absorber of 3.6 mg/cm^2.

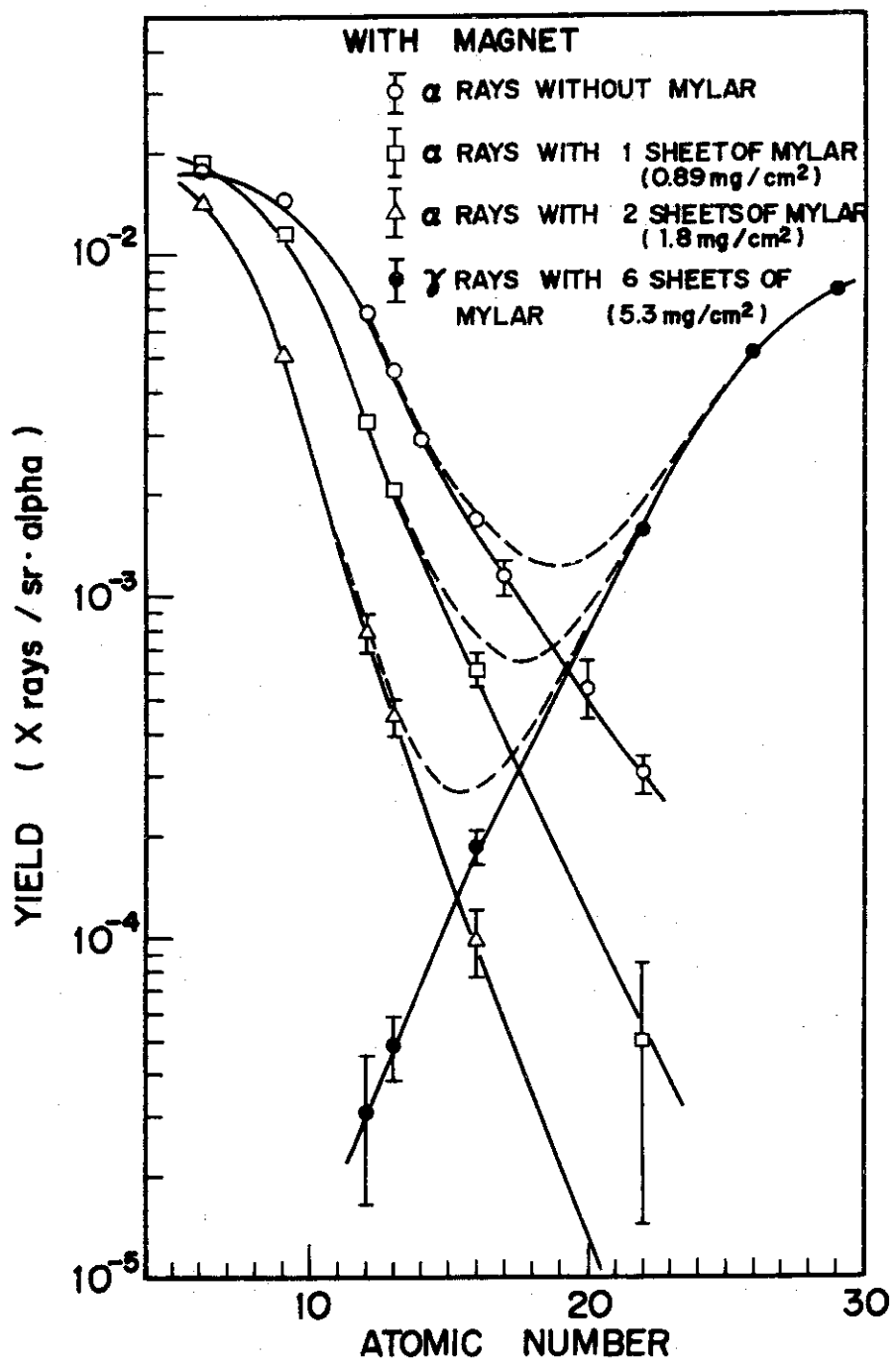

Fig. 16 Thick target yields of K X rays produced by radiations from the ^{241}Am alpha-ray source, with a magnet and Mylar films in various thicknesses. Broken lines show the yields for both alpha and gamma (or X) rays. Data without error bar have errors of 10 %.

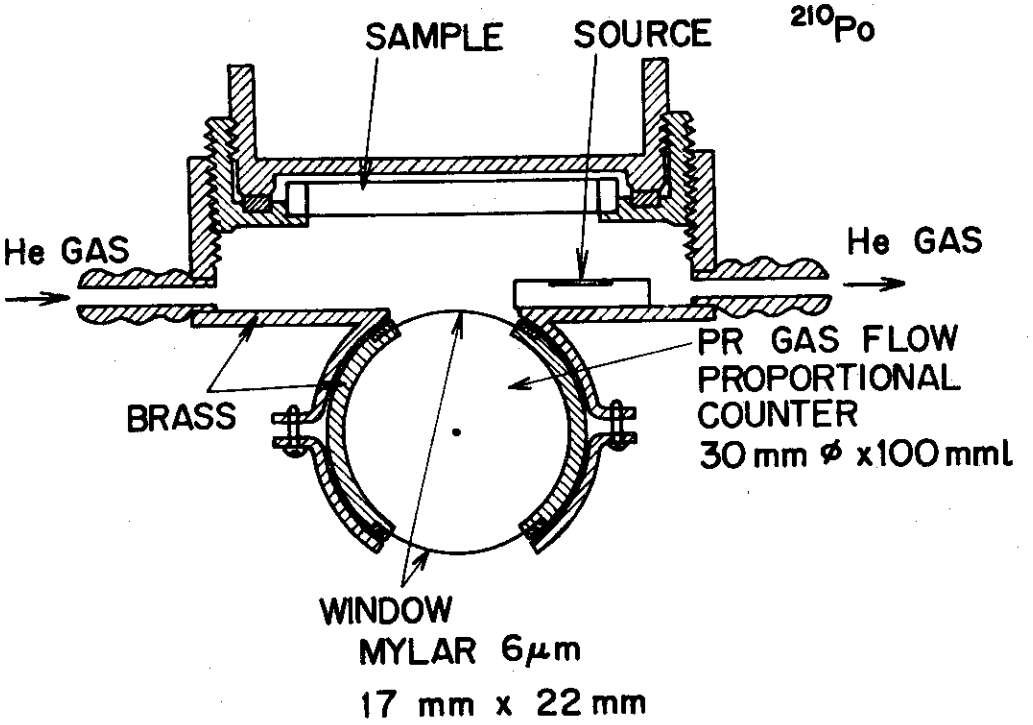

Fig. 17 Measuring chamber used for the experiments of X-ray excitation by a ^{210}Po alpha-ray source and tritium X-ray sources.

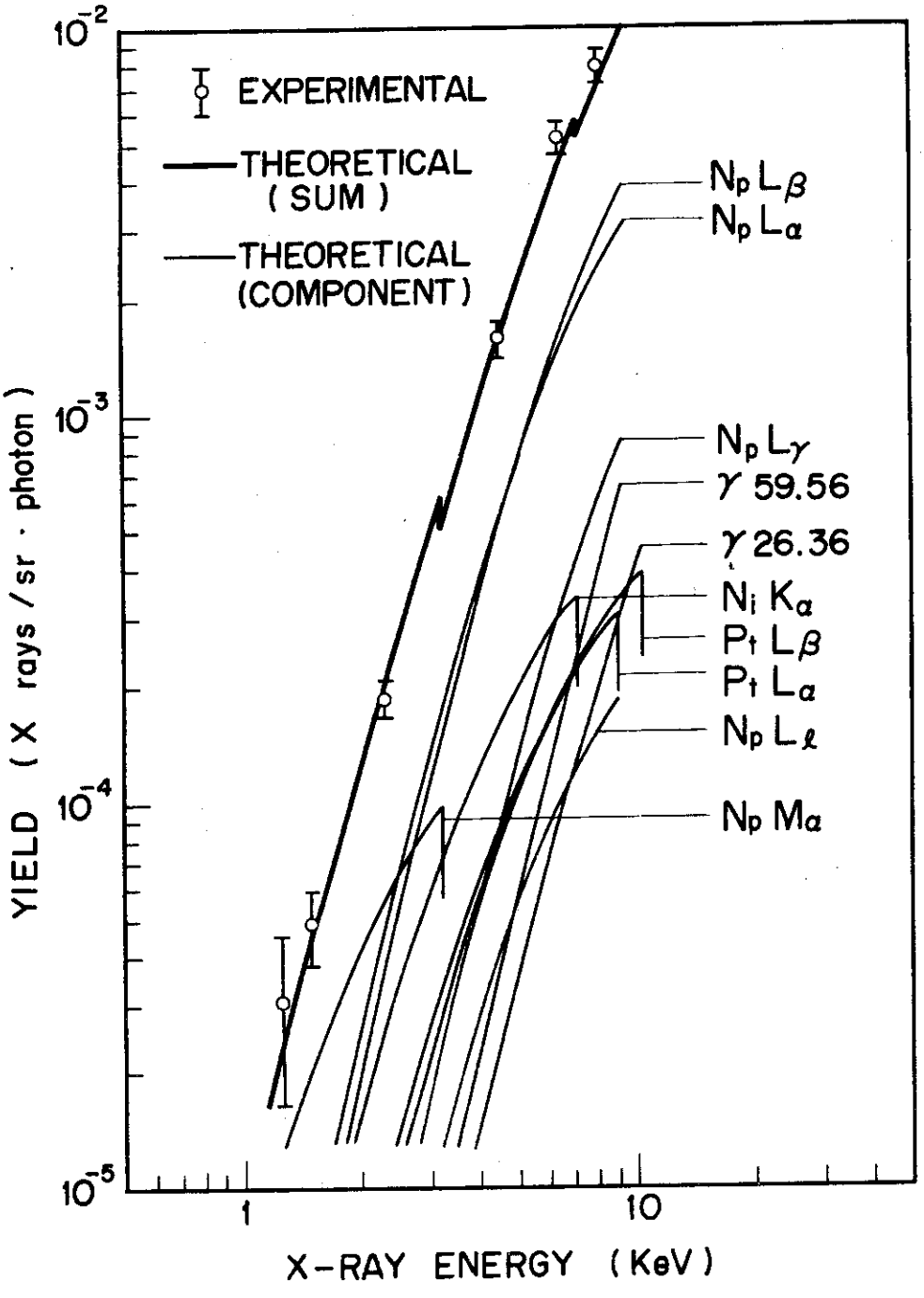

Fig. 18 Thick target yields of K X rays produced by gamma and X rays from the ^{241}Am source with 6 sheets of Mylar.

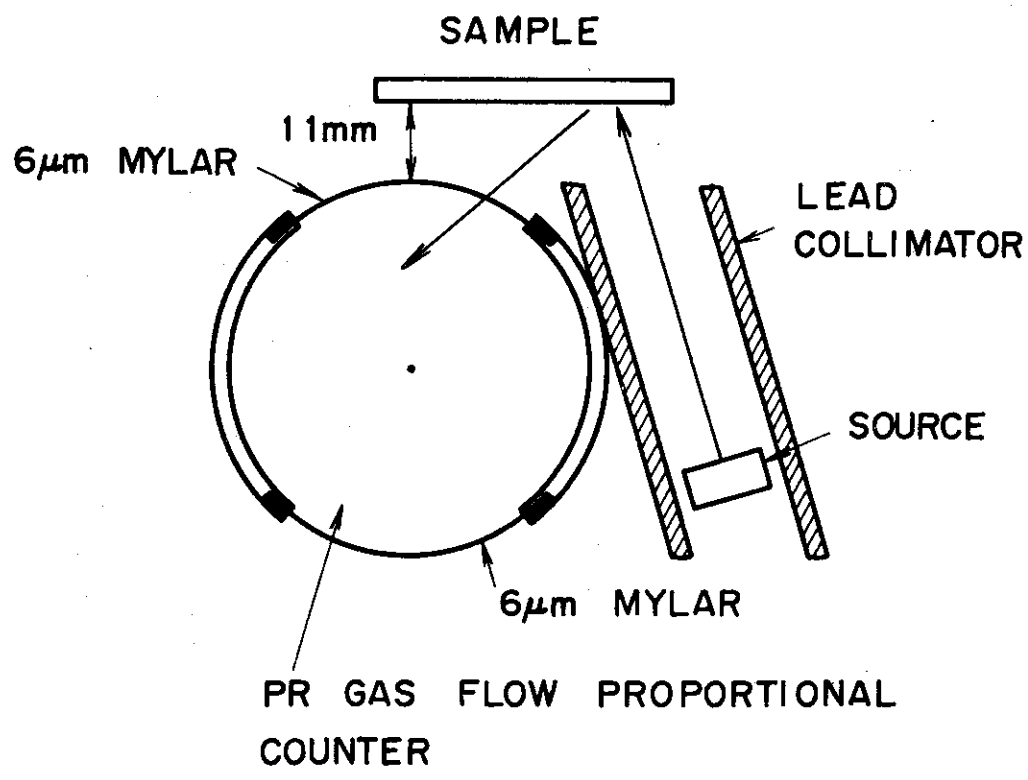

Fig. 19 Arrangement of source, sample, and detector used for the X-ray excitation by a ^{241}Am L X-ray source.

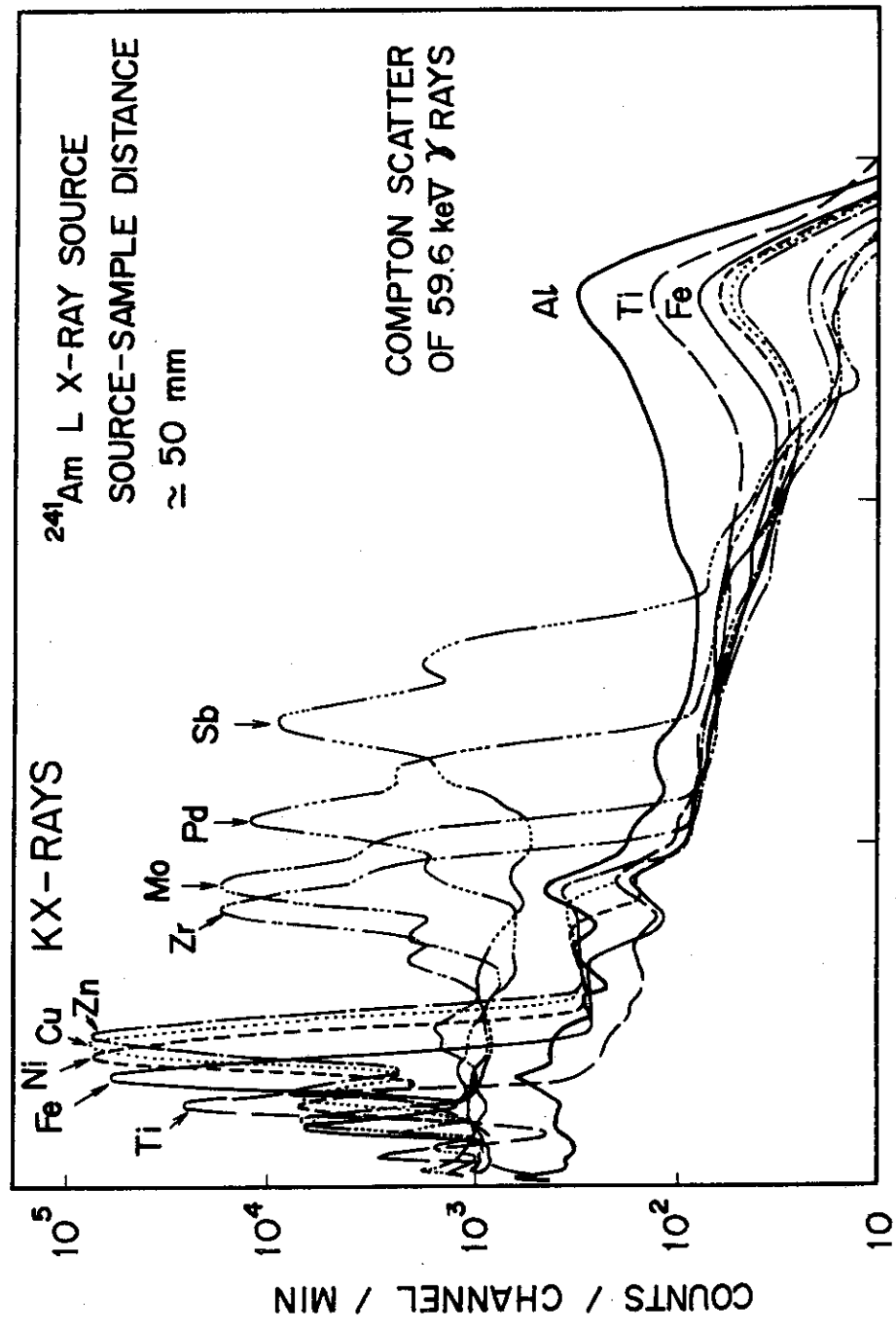

Fig. 20 Pulse-height spectra of emitted X rays and scattered gamma (and X) rays from pure element thick targets in the case of the ^{241}Am L X-ray source.

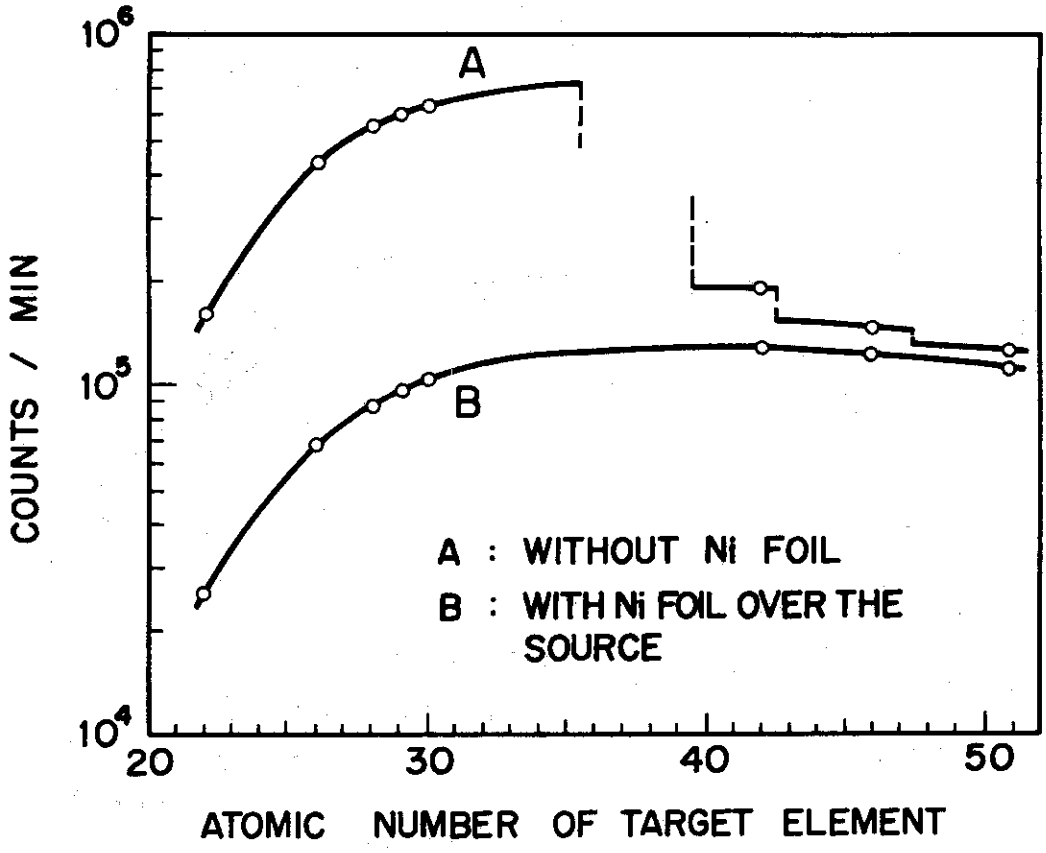

Fig. 21 K_α-ray counts of pure-element thick targets produced by the ^{241}Am L X-ray source, measured by a proportional counter.

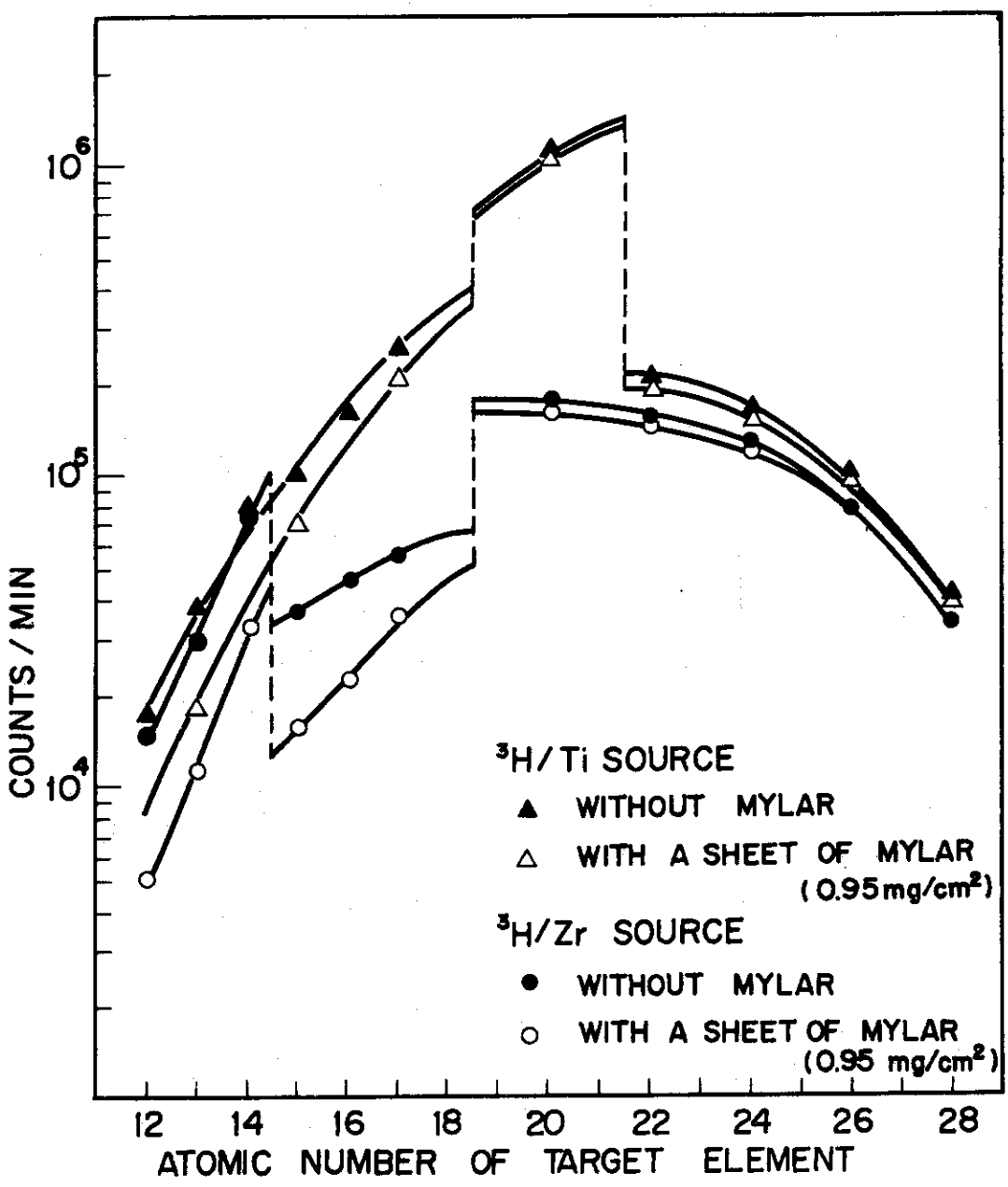

Fig. 22 K_α-ray counts of pure-element thick targets produced by tritium sources, measured by a proportional counter.

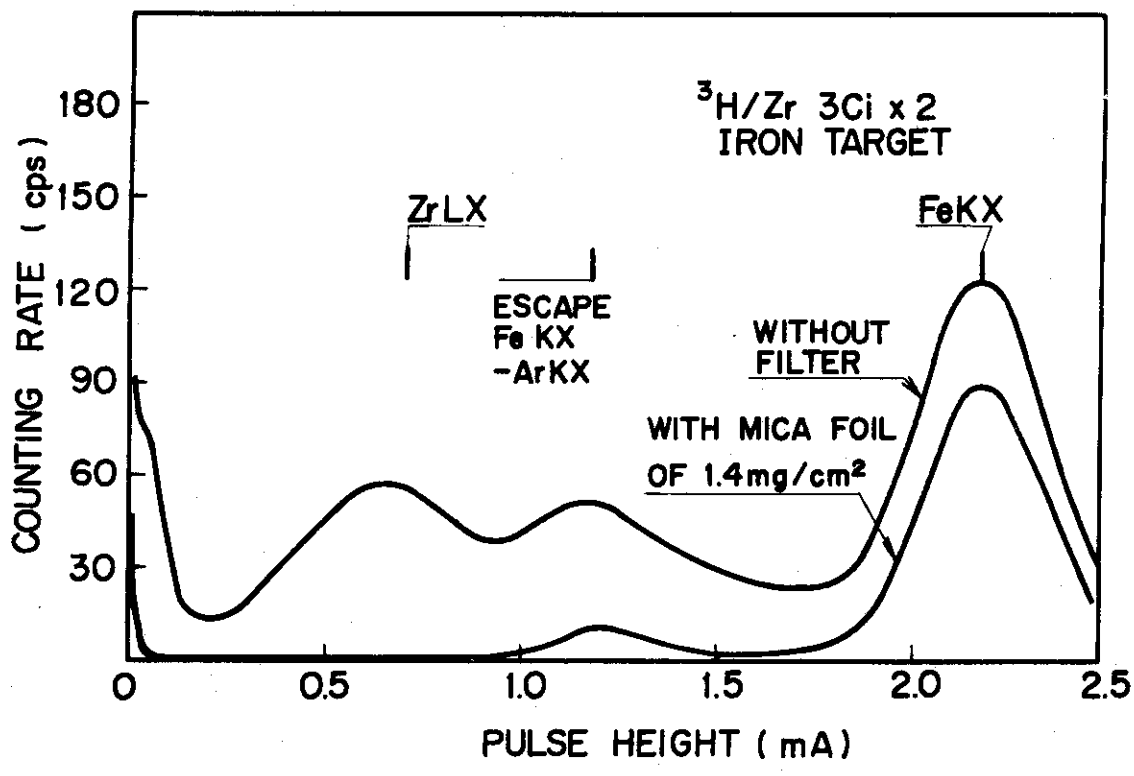

Fig. 23 Pulse-height spectra of fluorescent X rays and scattered radiations in the case of a ^{3}H/Zr source in vacuum.

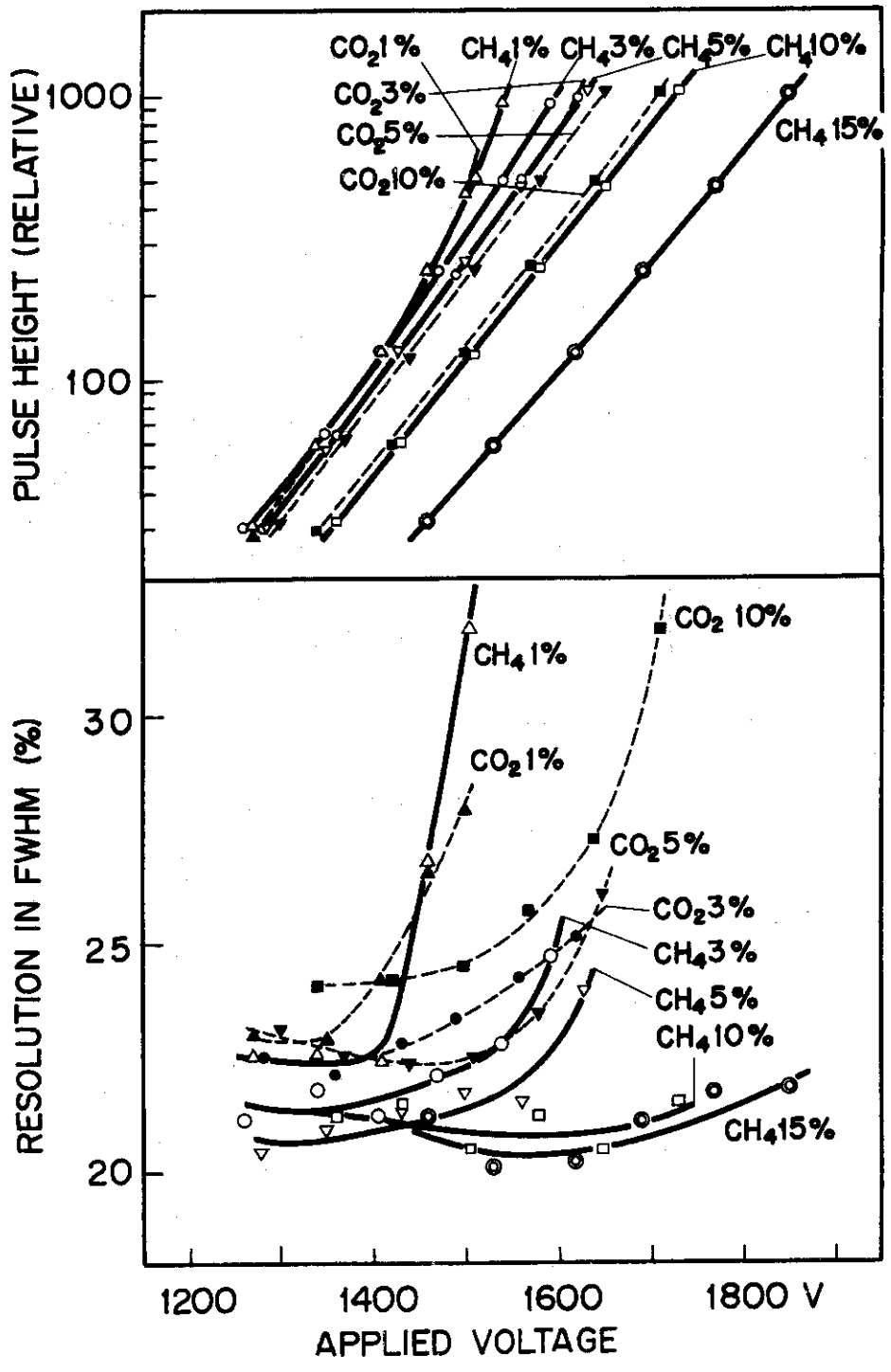

Fig. 24 Gas gain and energy resolution of a proportional counter using Ar-CH_4 or Ar-CO_2 gas mixtures.

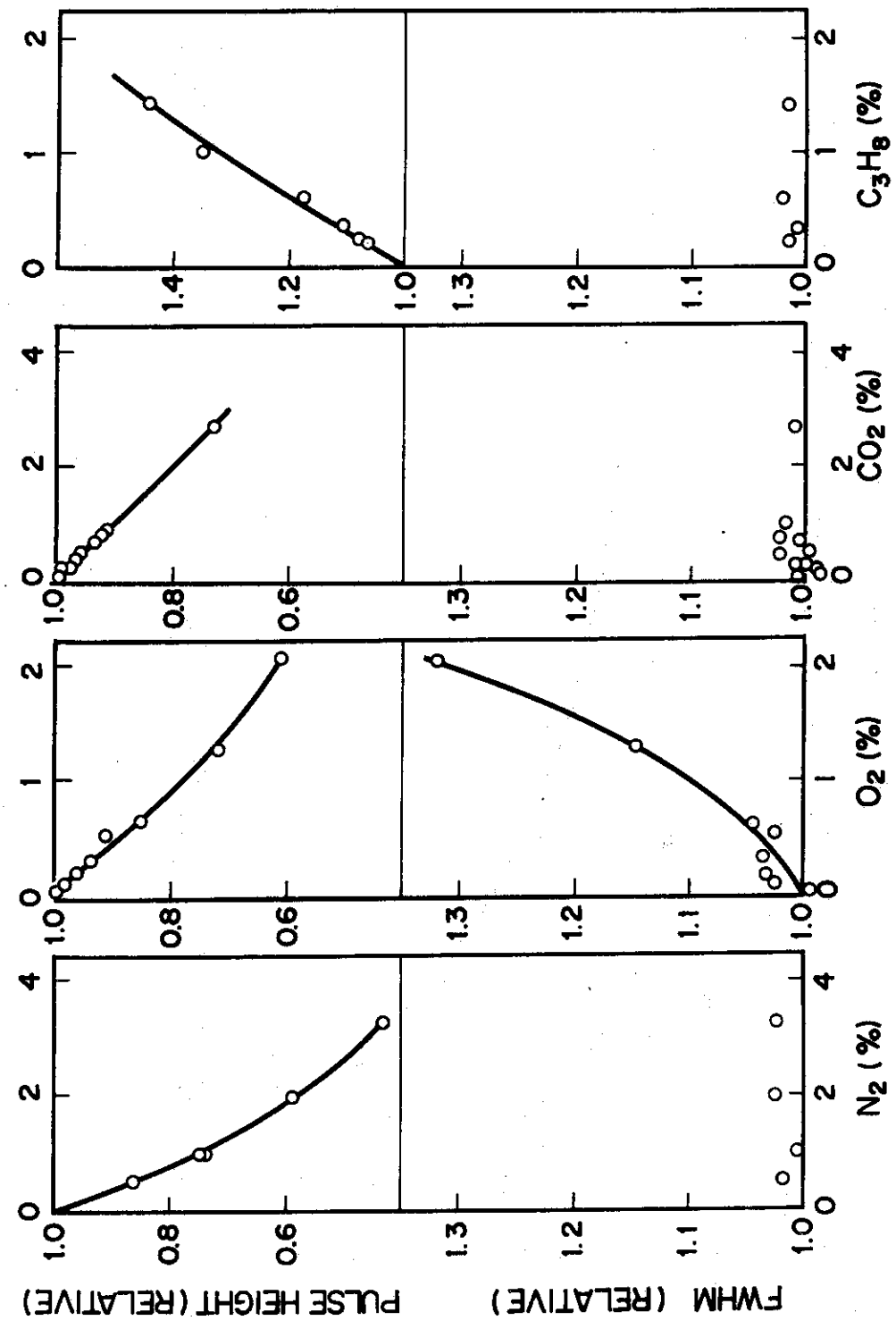

Fig. 25 Effects of impurity gases in a proportional counter using an Ar 90% plus CH_4 10% gas.

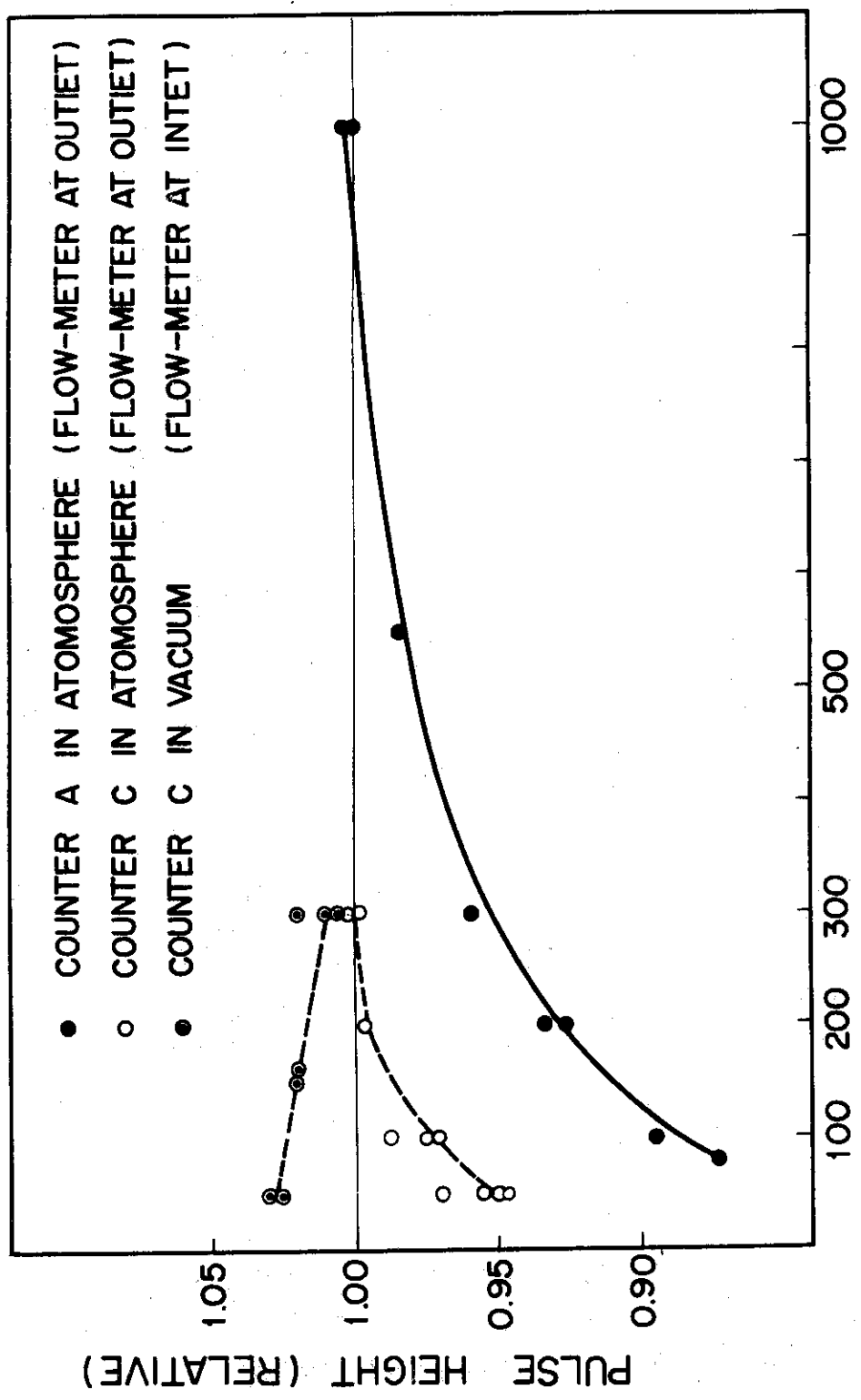

Fig. 26 Flow-rate dependence of gas gain in proportional counters.

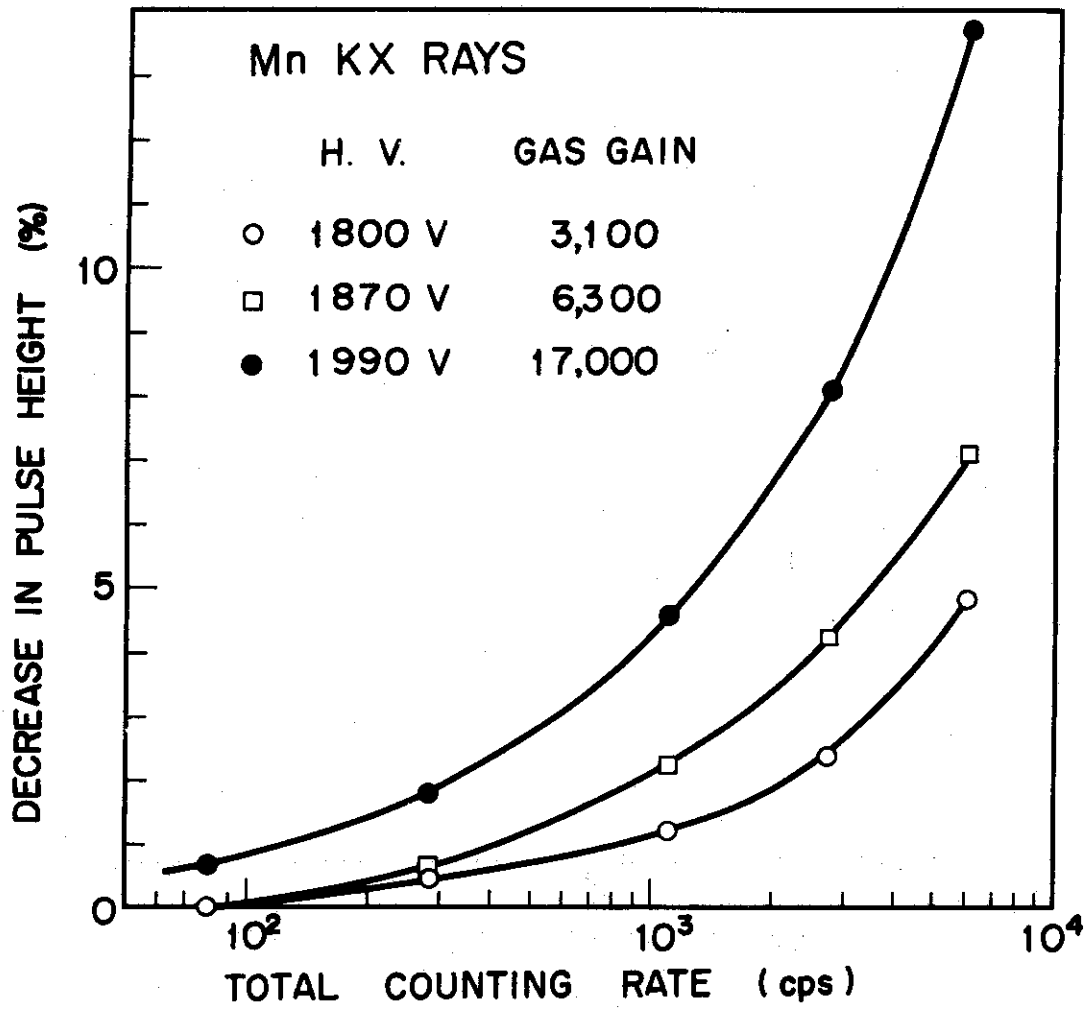

Fig. 27 Pulse-height shift versus counting rate in a proportional counter.

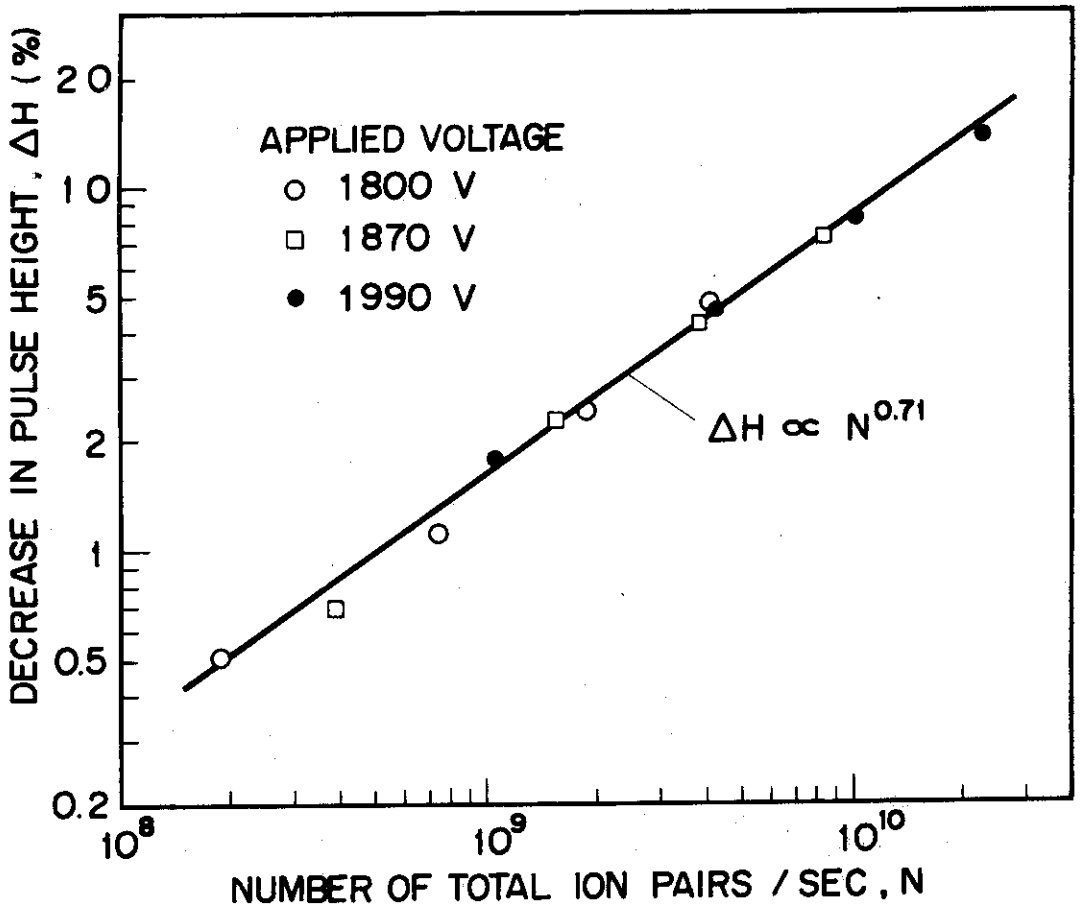

Fig. 28 Pulse-height shift versus total electric charge production in a proportional counter.

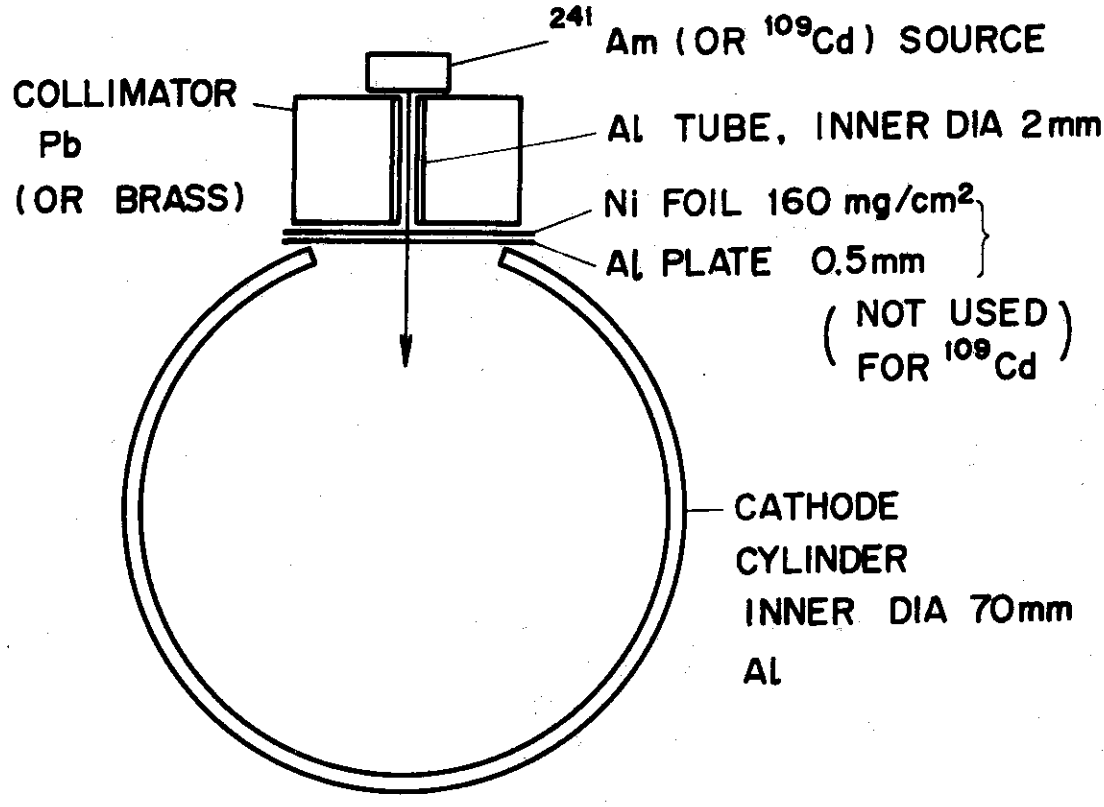

Fig. 29 Arrangement of source, collimator, and counter, set in a pressurizing vessel for measurement of pulse-height distribution characteristics of proportional counter.

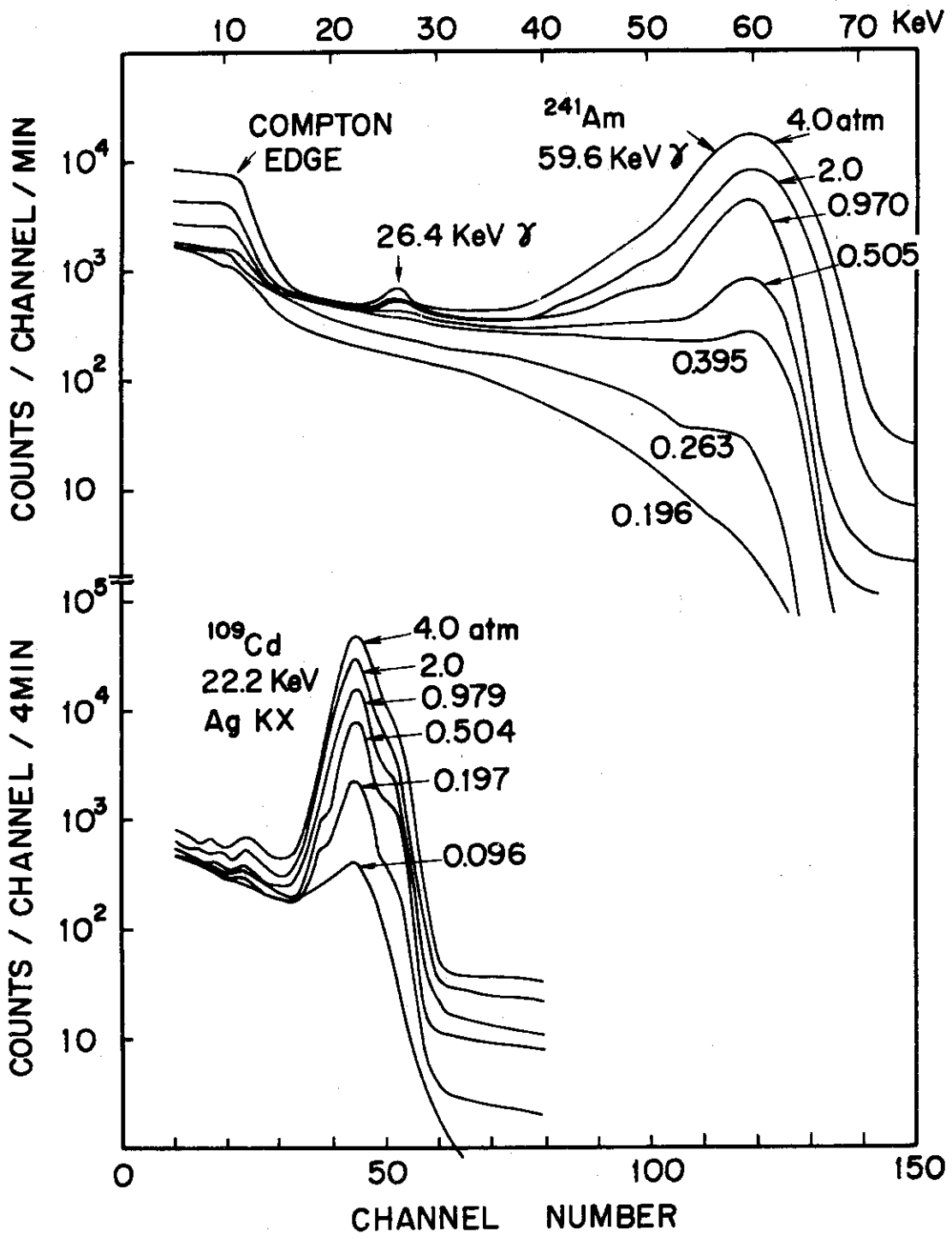

Fig. 30 Pulse-height distributions of a proportional counter with PR gas in various pressures.

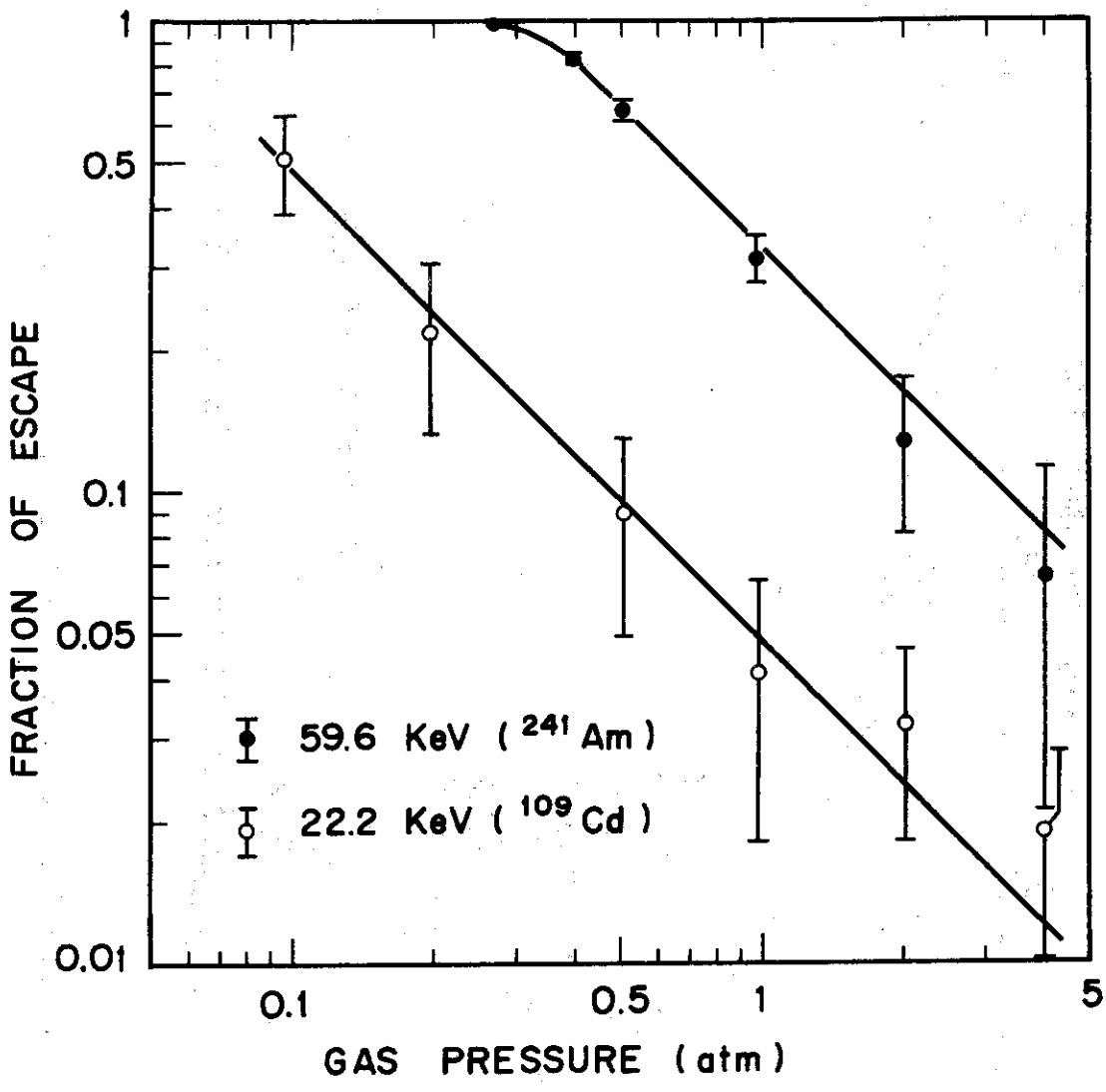

Fig. 31 Fraction of photoelectron escape. Solid lines are inversely proportional to gas pressure.

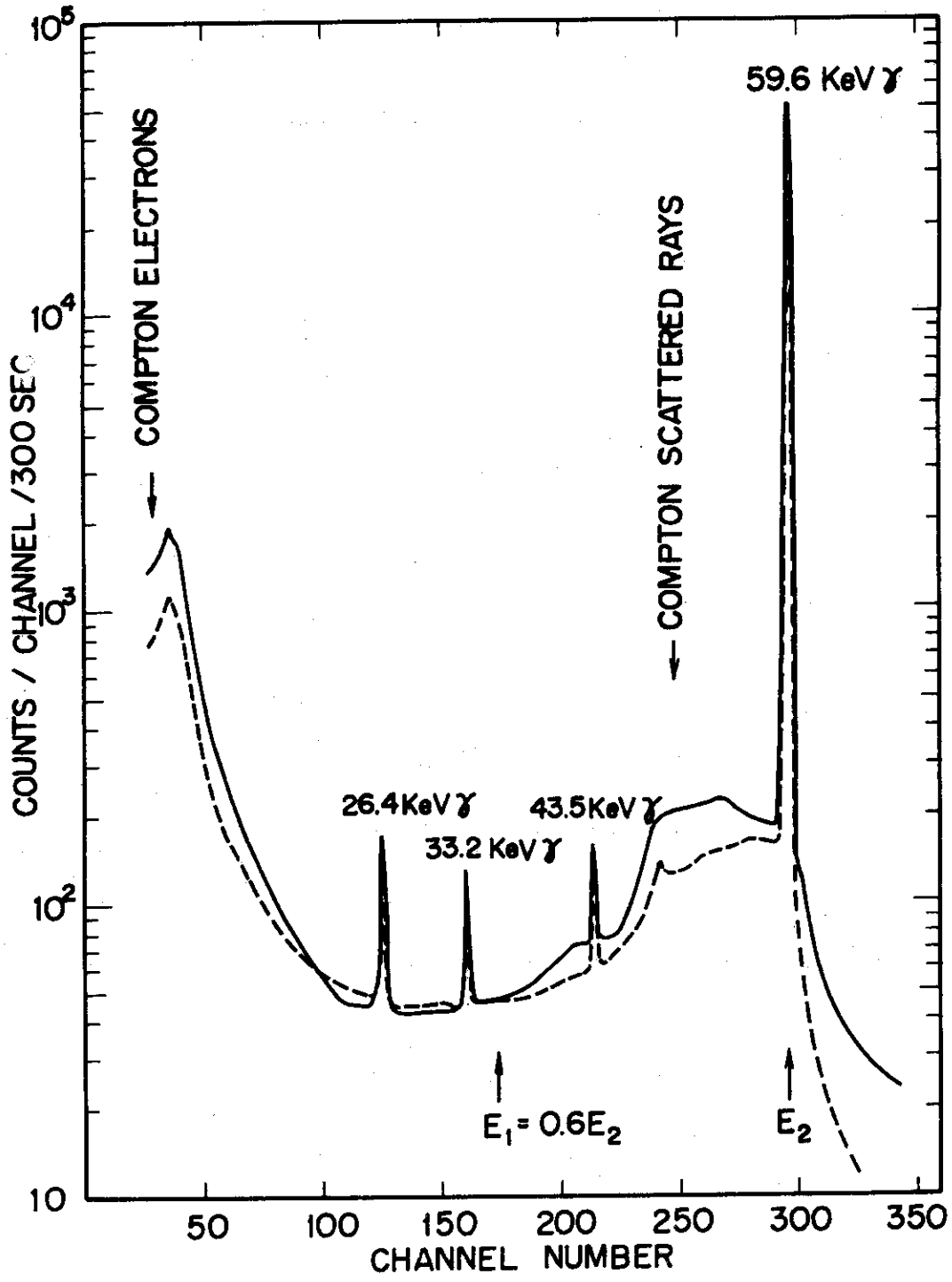

Fig. 32 Pulse-height distributions of a Si(Li) detector for the collimated 59.6 keV gamma rays from ^{241}Am with a brass plus aluminum absorber. Solid line: collimated to the center part of the sensitive area, and broken line: collimated to the edge part of it.

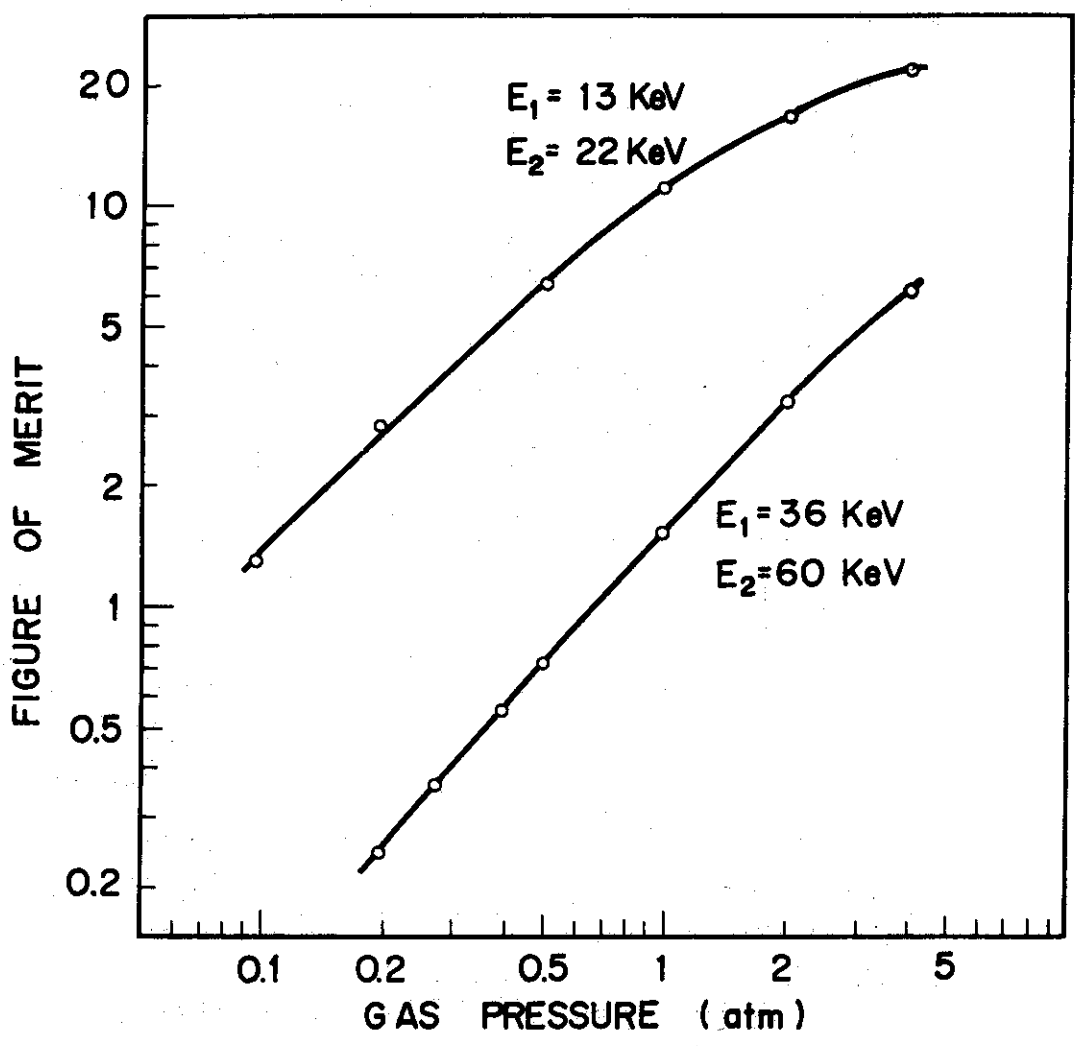

Fig. 33 Figure of merit of the proportional counter of Fig. 29 versus PR gas pressure.

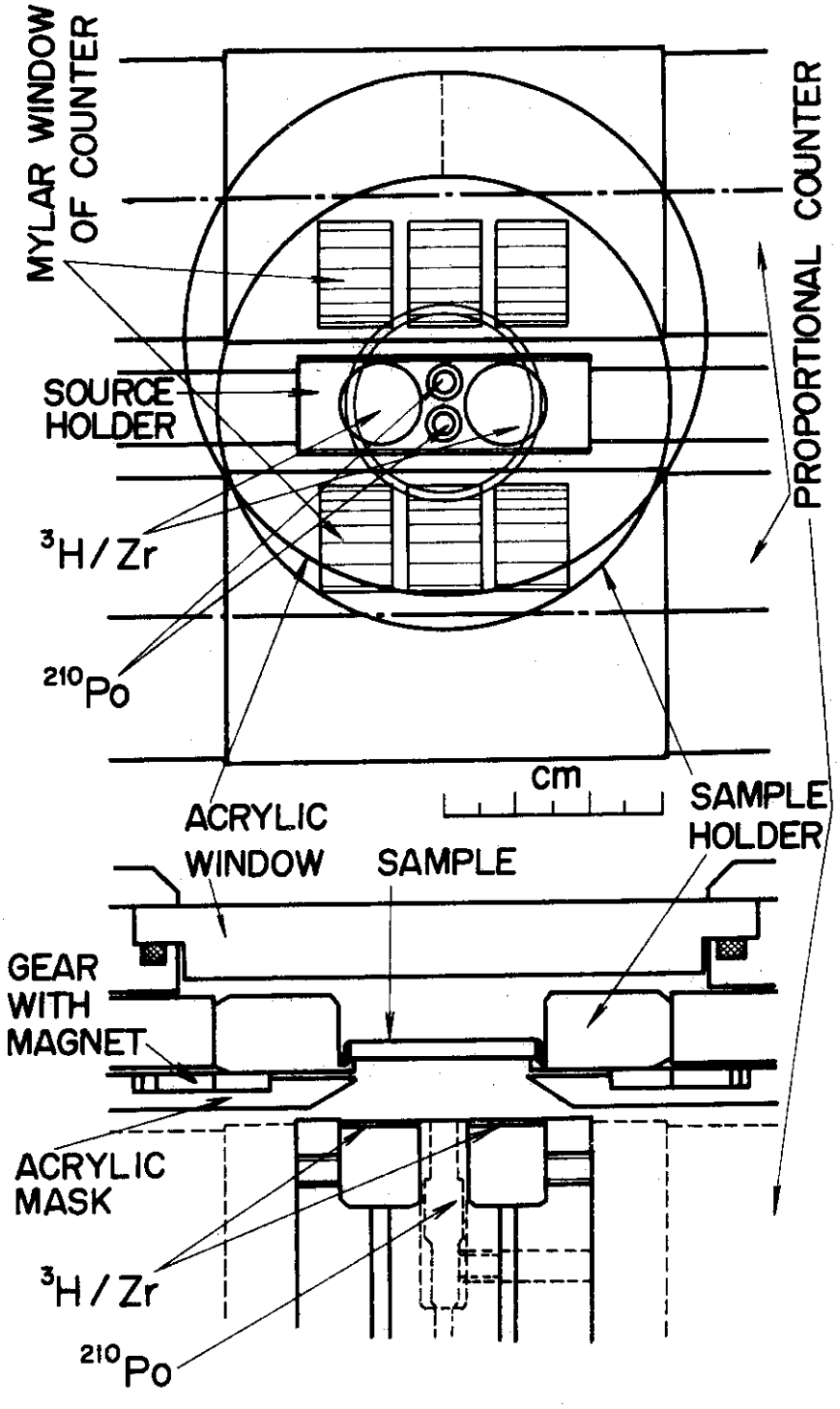

Fig. 34 Arrangement of the source, sample, and proportional counters in the X-ray analyzer for cement raw mixtures.

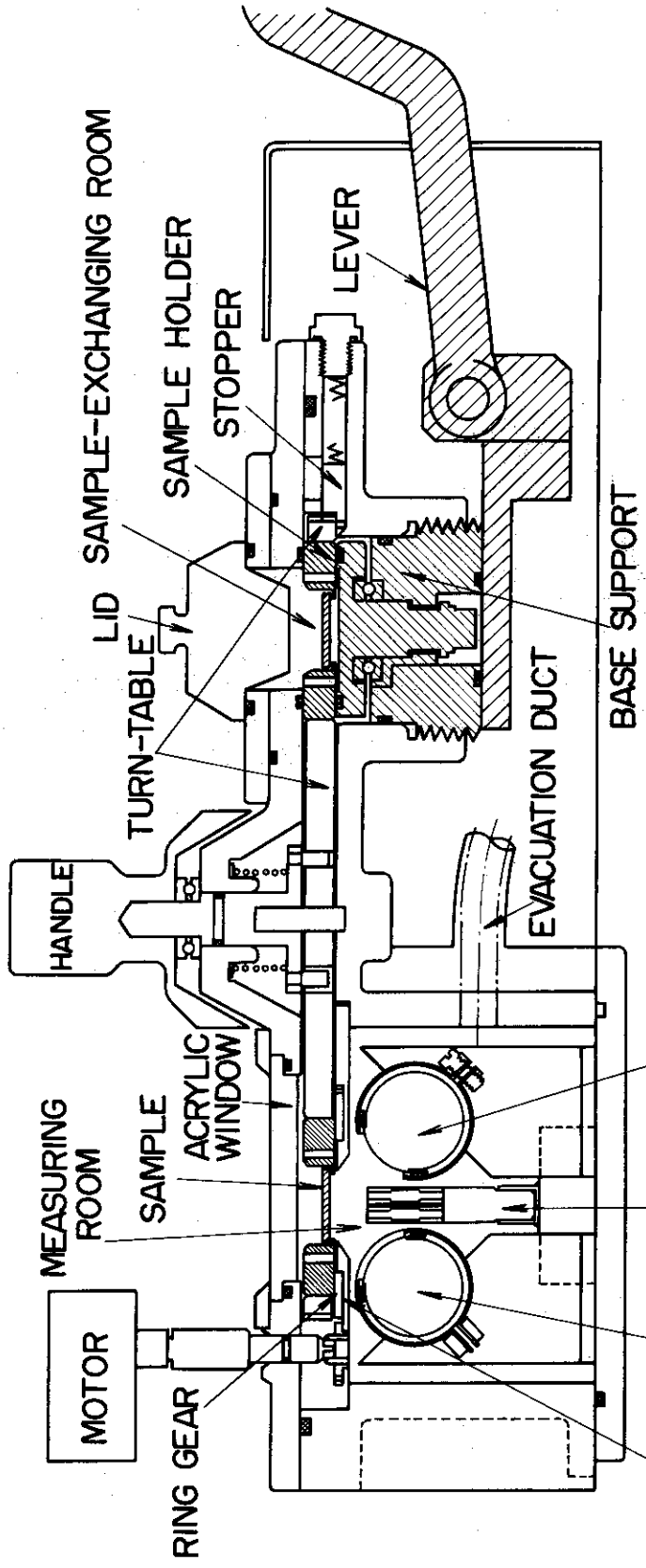

Fig. 35 Cross section of the measuring head in the X-ray analyzer for cement raw mixtures.

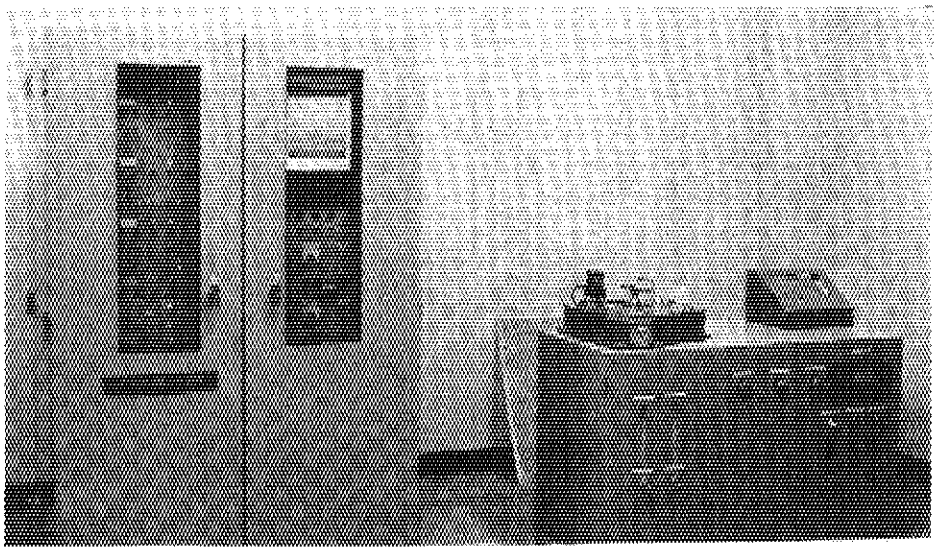

Fig. 36 Outside view of the analyzer for cement raw mixtures.

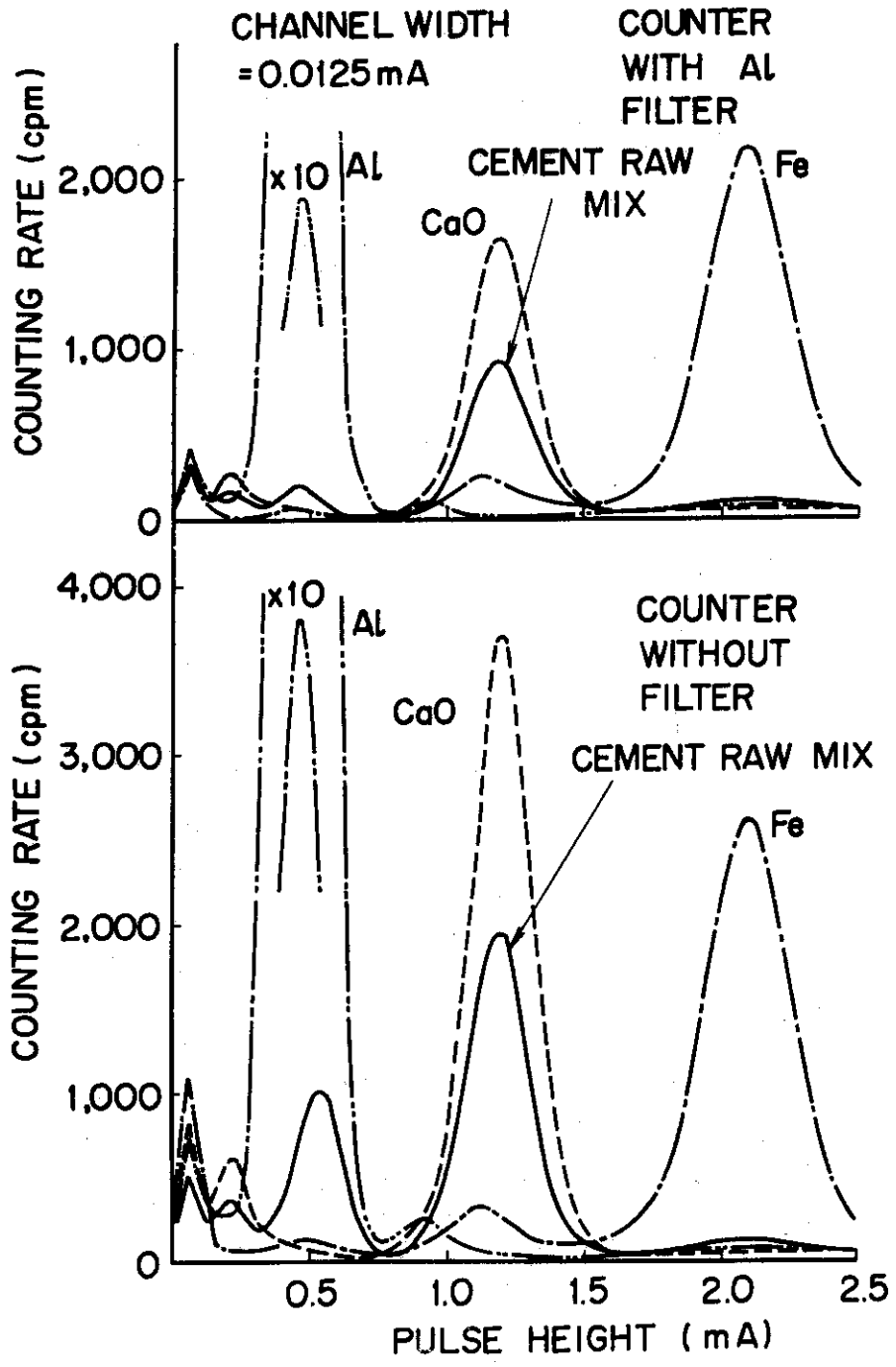

Fig. 37 Pulse-height spectra of the X rays from the pure elements and a cement raw material mixture; Fe_2O_3 2.21%, CaO 43.19%, SiO_2 15.02%, Al_2O_3 3.39%, MgO 0.69%, and ignition loss in the raw mixture.

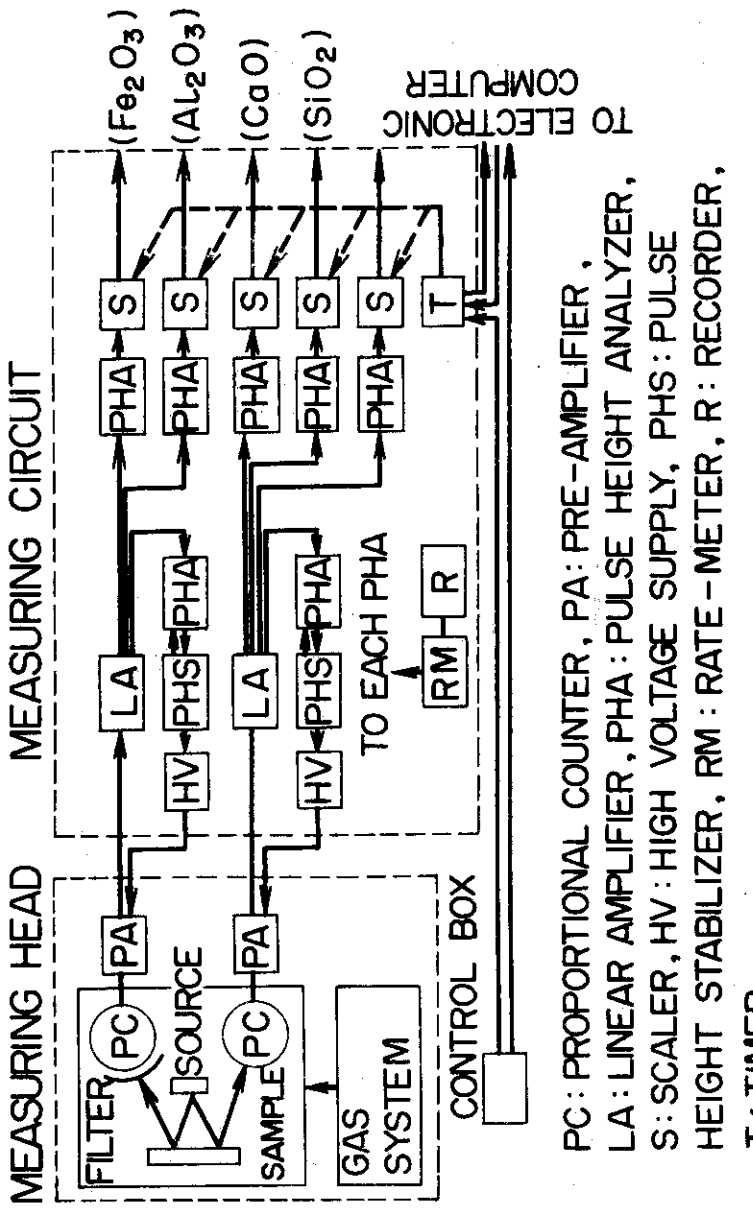

Fig. 38 Blockdiagram of the X-ray analyzer for cement raw mixtures.

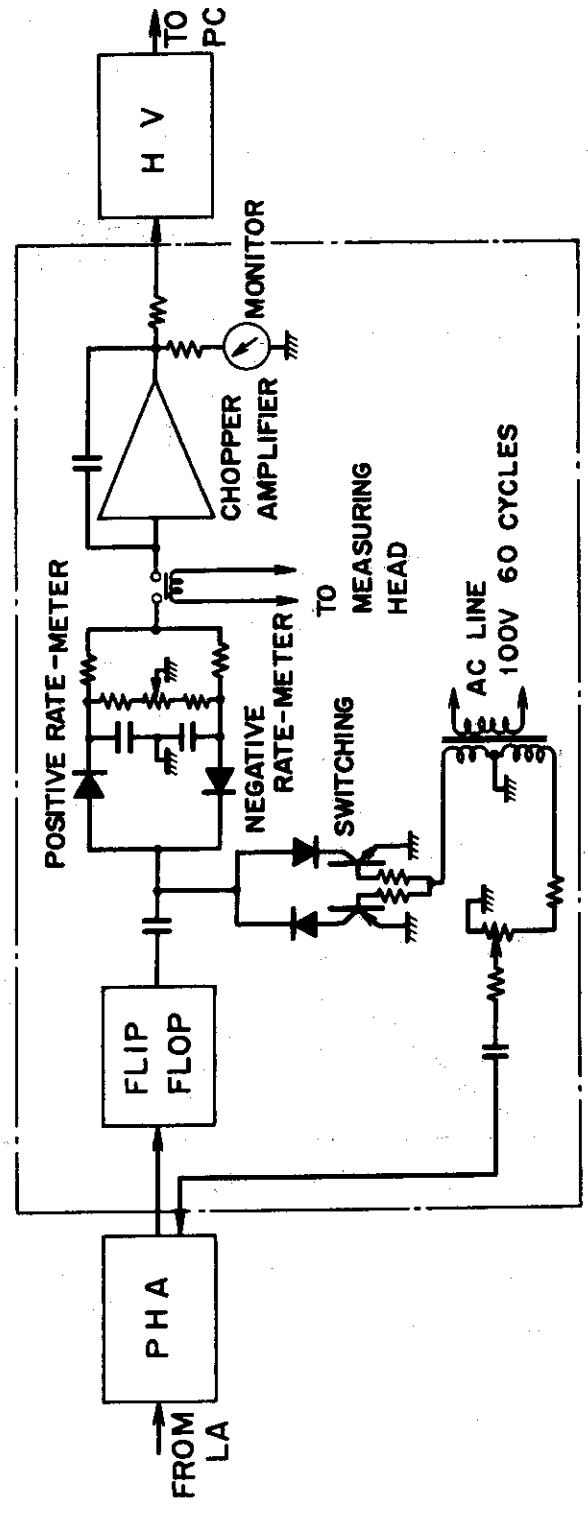

Fig. 39 Schematic circuit of the pulse-height stabilizer used in the X-ray analyzer for cement raw mixtures.

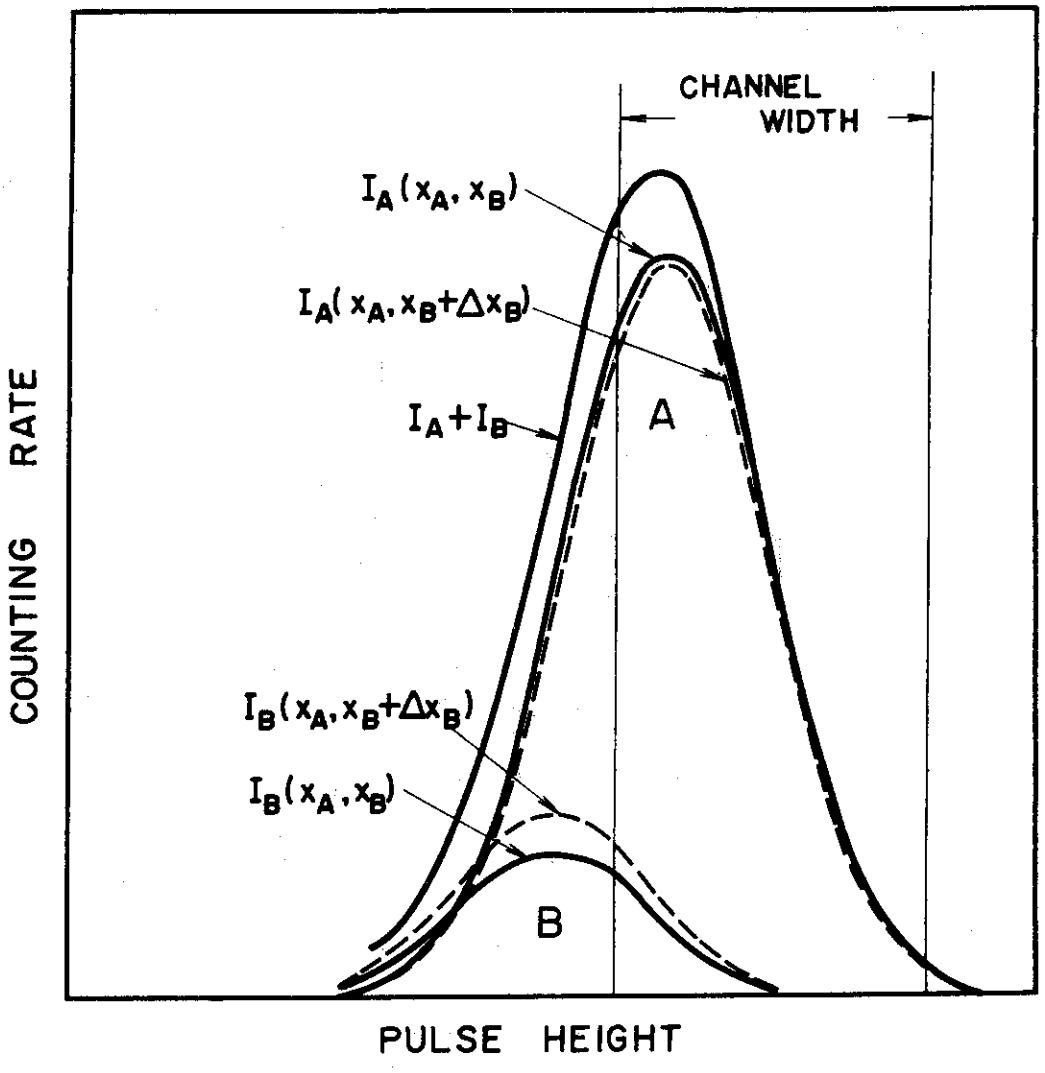

Fig. 40 Channel-level-setting utilizing the cancel effect in quantitative analysis by pulse-height discrimination. Broken lines are pulse-height distributions when only x_B increases by a small quantity Δx_B.

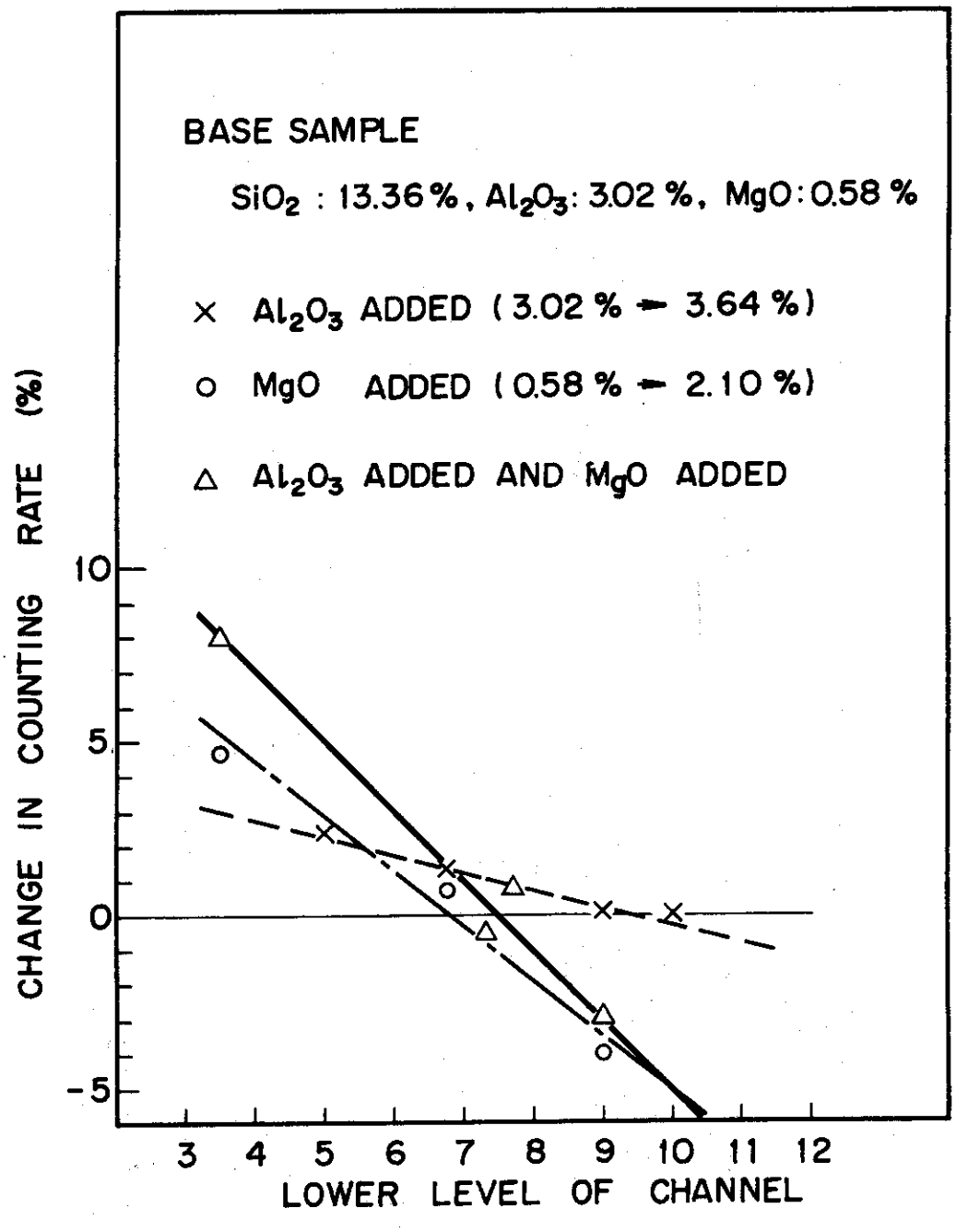

Fig. 41 Effects of Al_2O_3 and MgO contents to the count of the Si-channel.

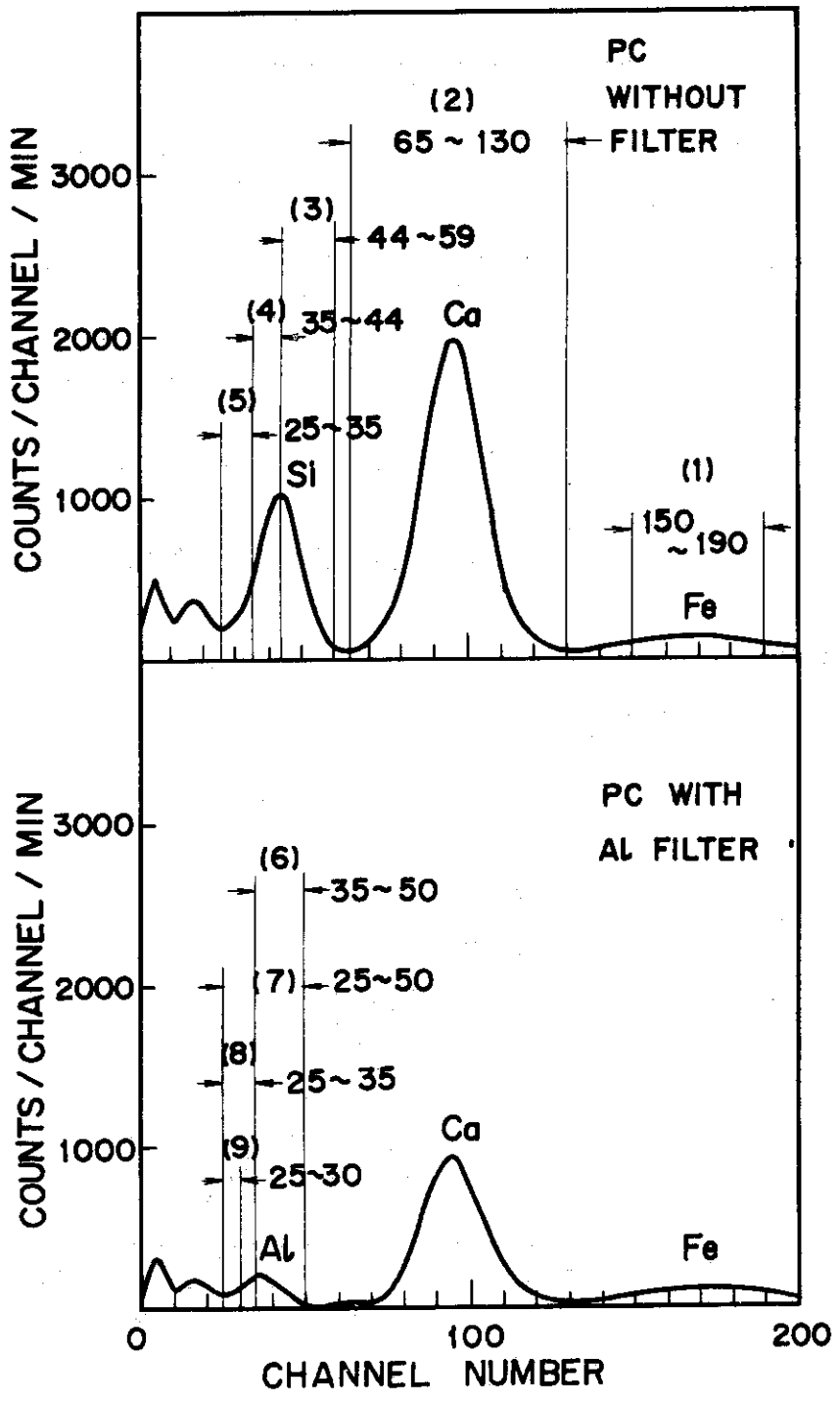

Fig. 42 Channel setting for determination of calibration coefficients and analysis of cement raw mixtures.

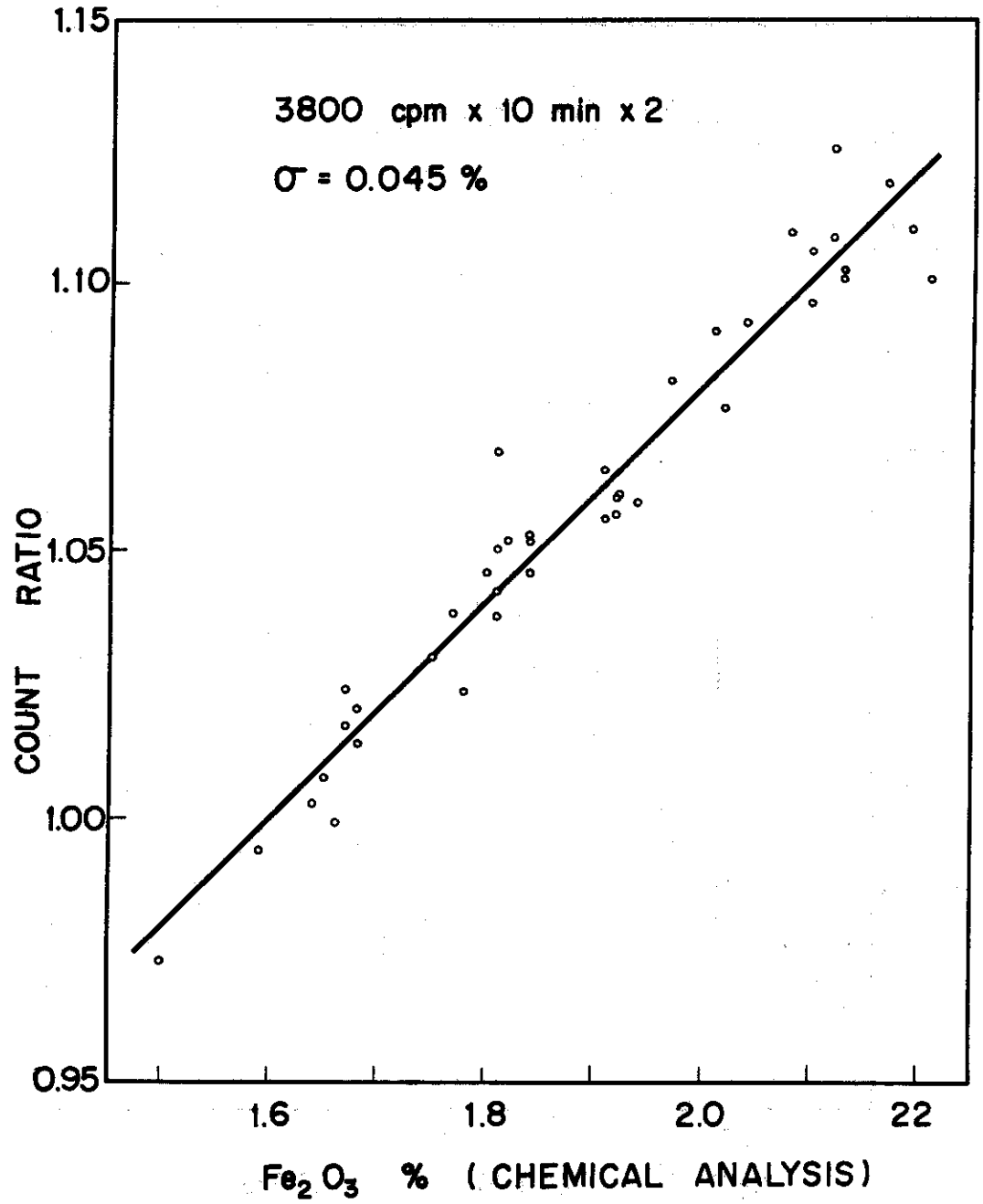

Fig. 43 Count of the Fe-channel versus the content of Fe_2O_3 determined by chemical analysis.

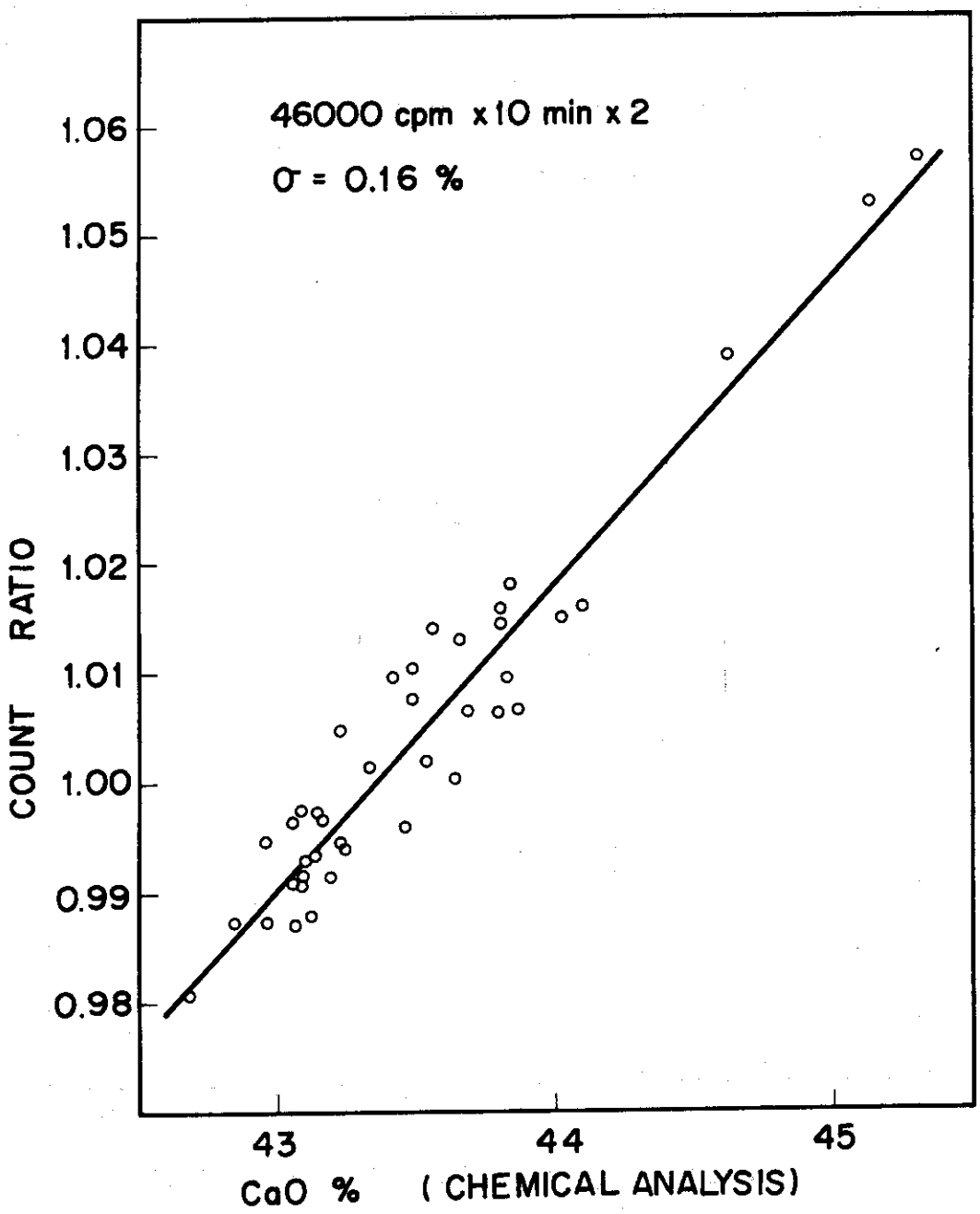

Fig. 44 Count of the Ca-channel versus the content of CaO cetermined by chemical analysis.

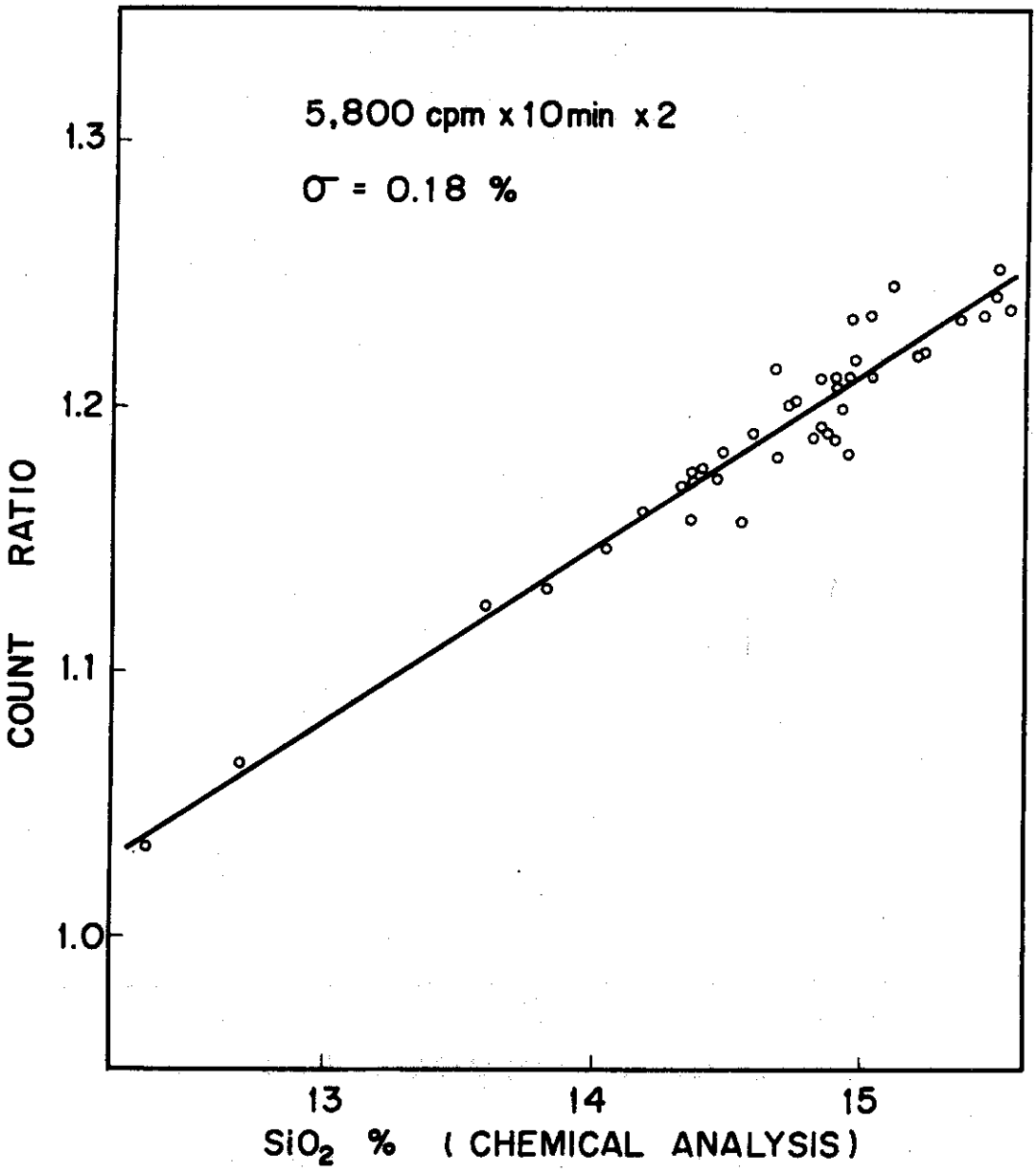

Fig. 45 Count of the Si-channel versus the content of SiO_2 determined by chemical analysis.

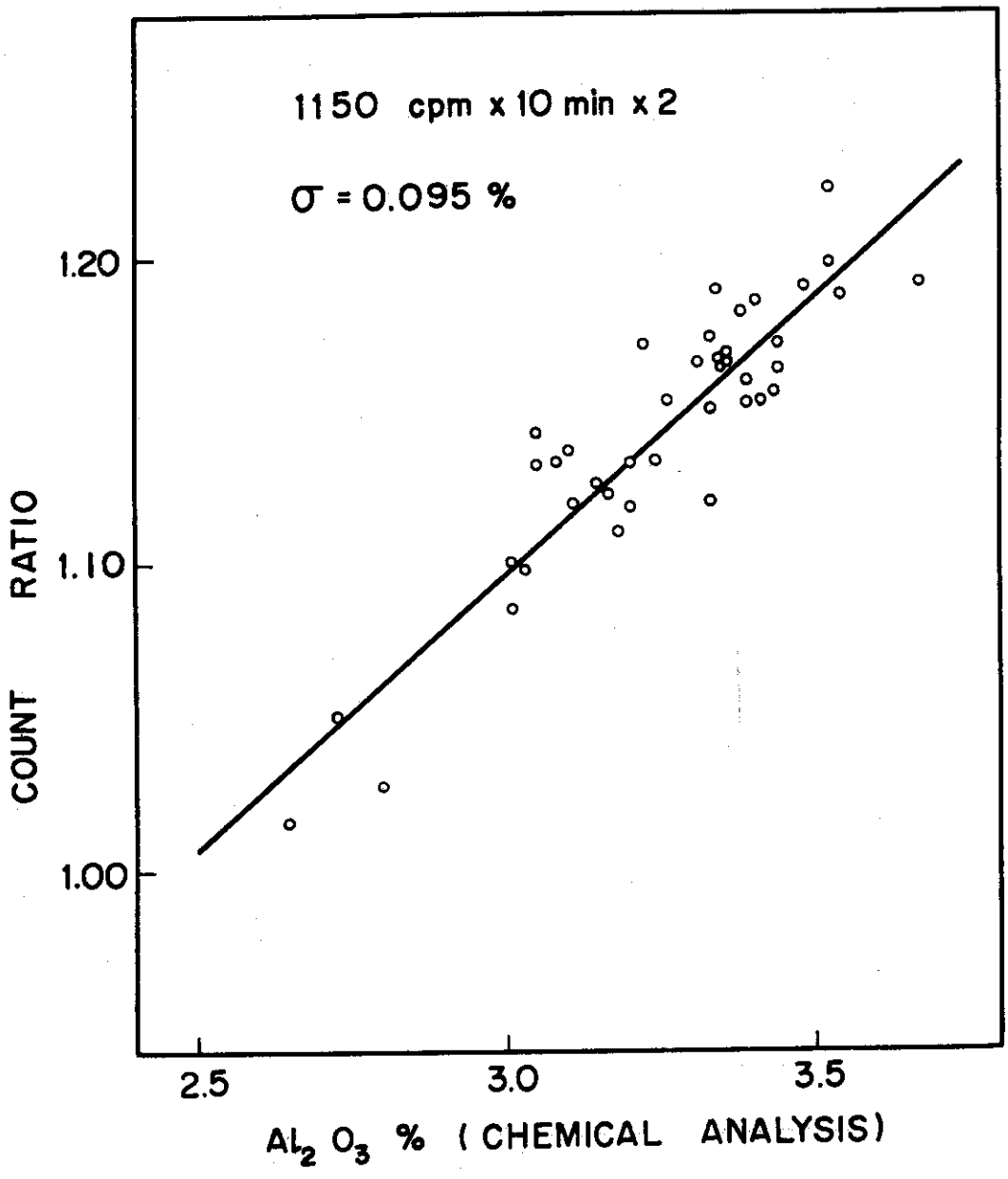

Fig. 46 Count of the Al-channel versus the content of Al_2O_3 determined by chemical analysis.

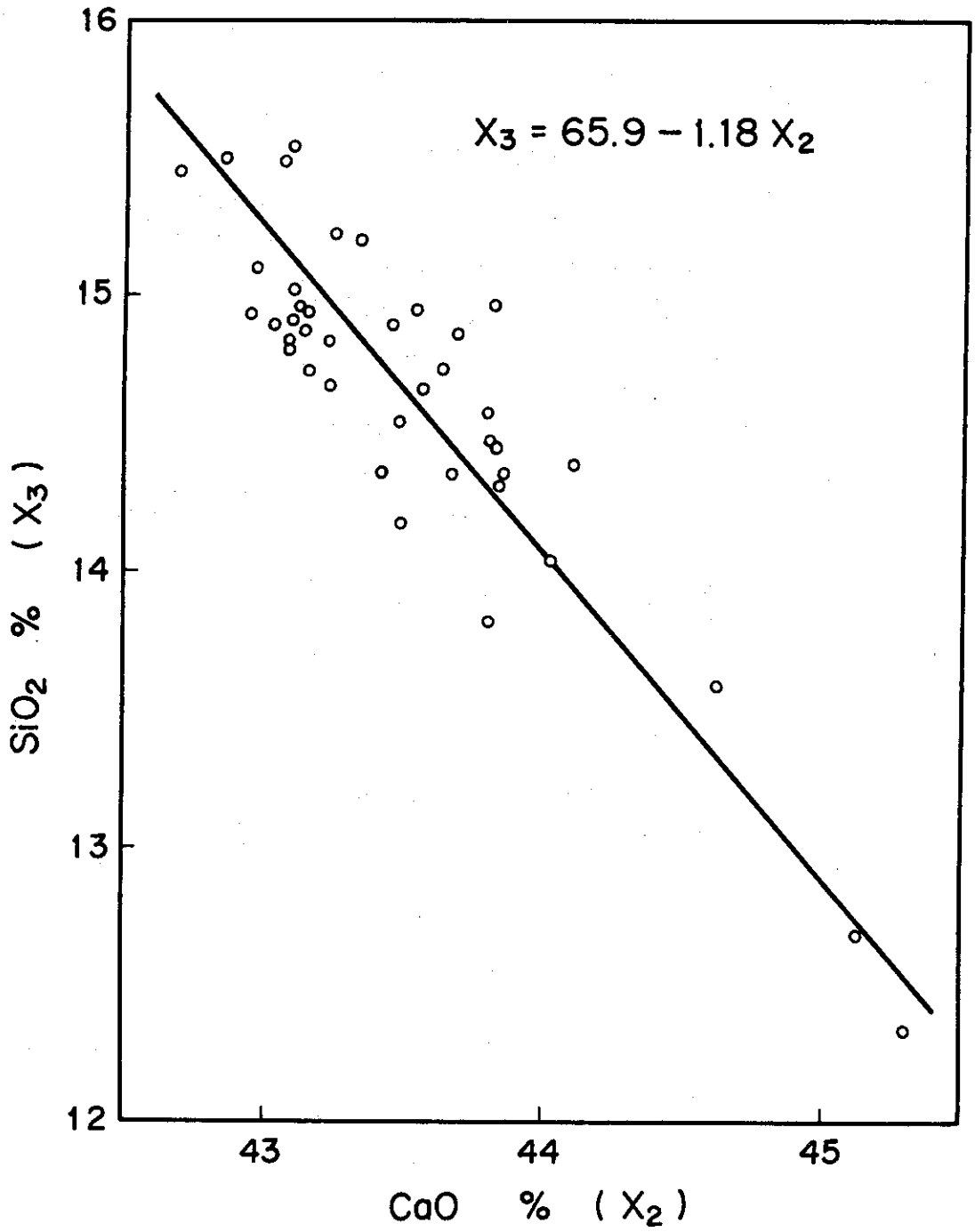

Fig. 47 Correlation between the lime and the silica in cement raw mixtures.

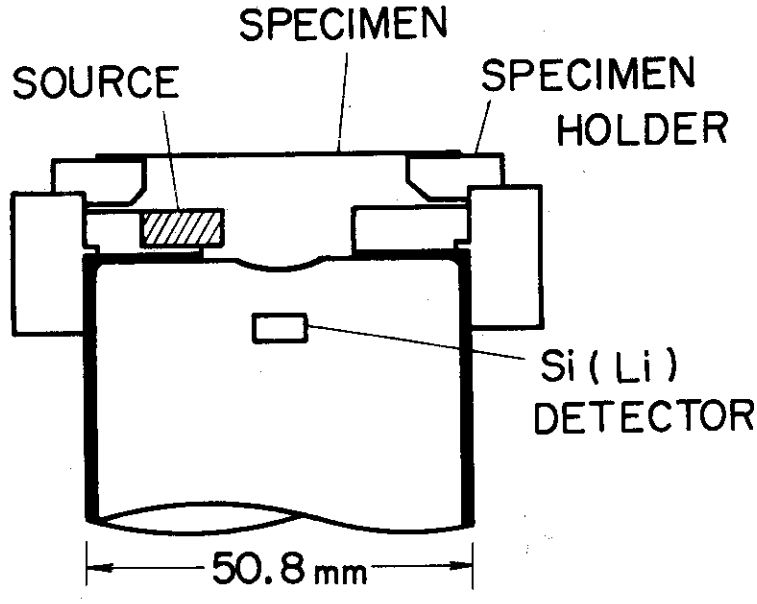

Fig. 48 Geometrical arrangement of source, specimen, and detector for analysis of airborne particulates.

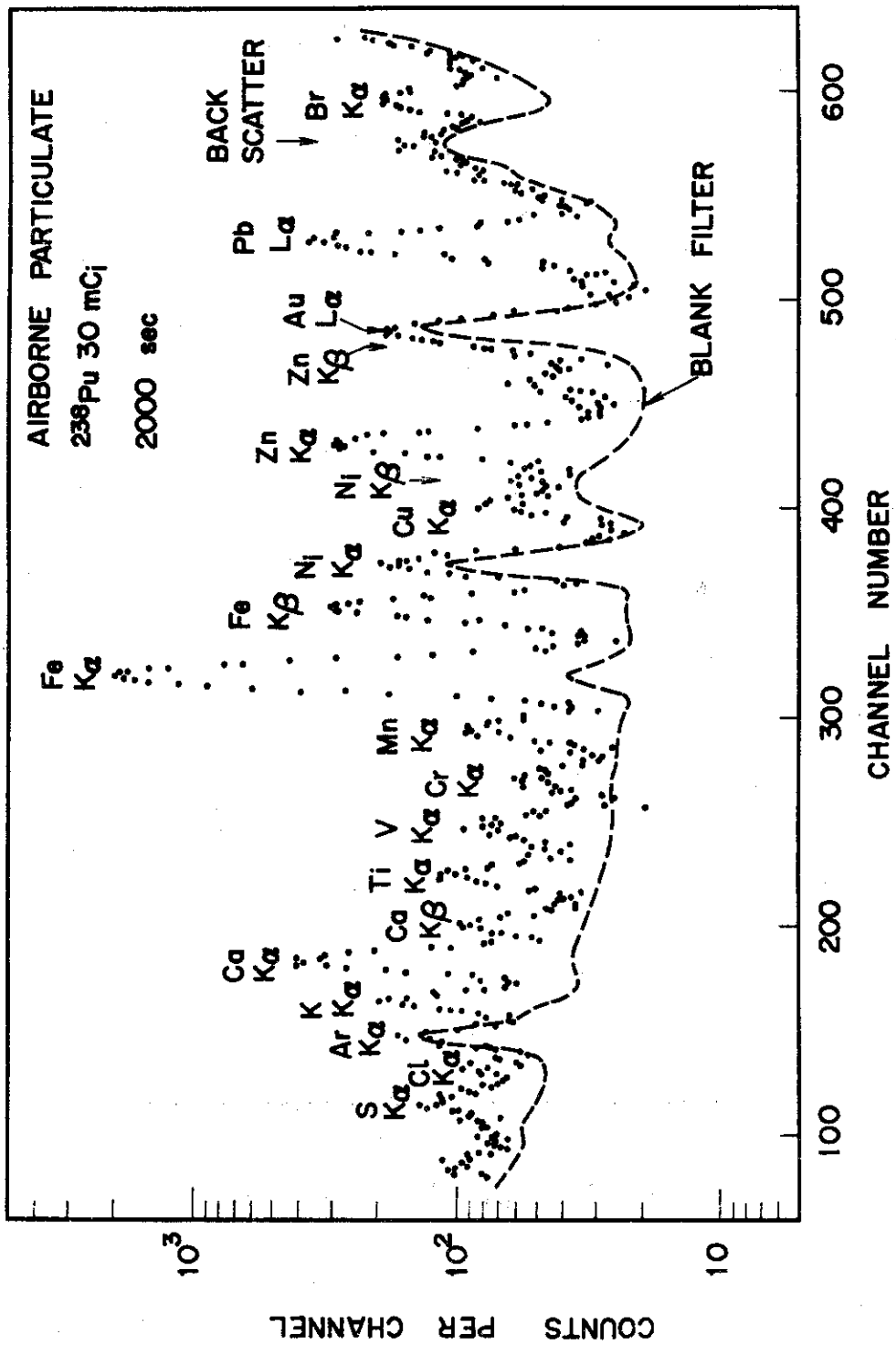

Fig. 49 Fluorescent X-ray spectrum of air filter specimen measured with a Si(Li) detector system.

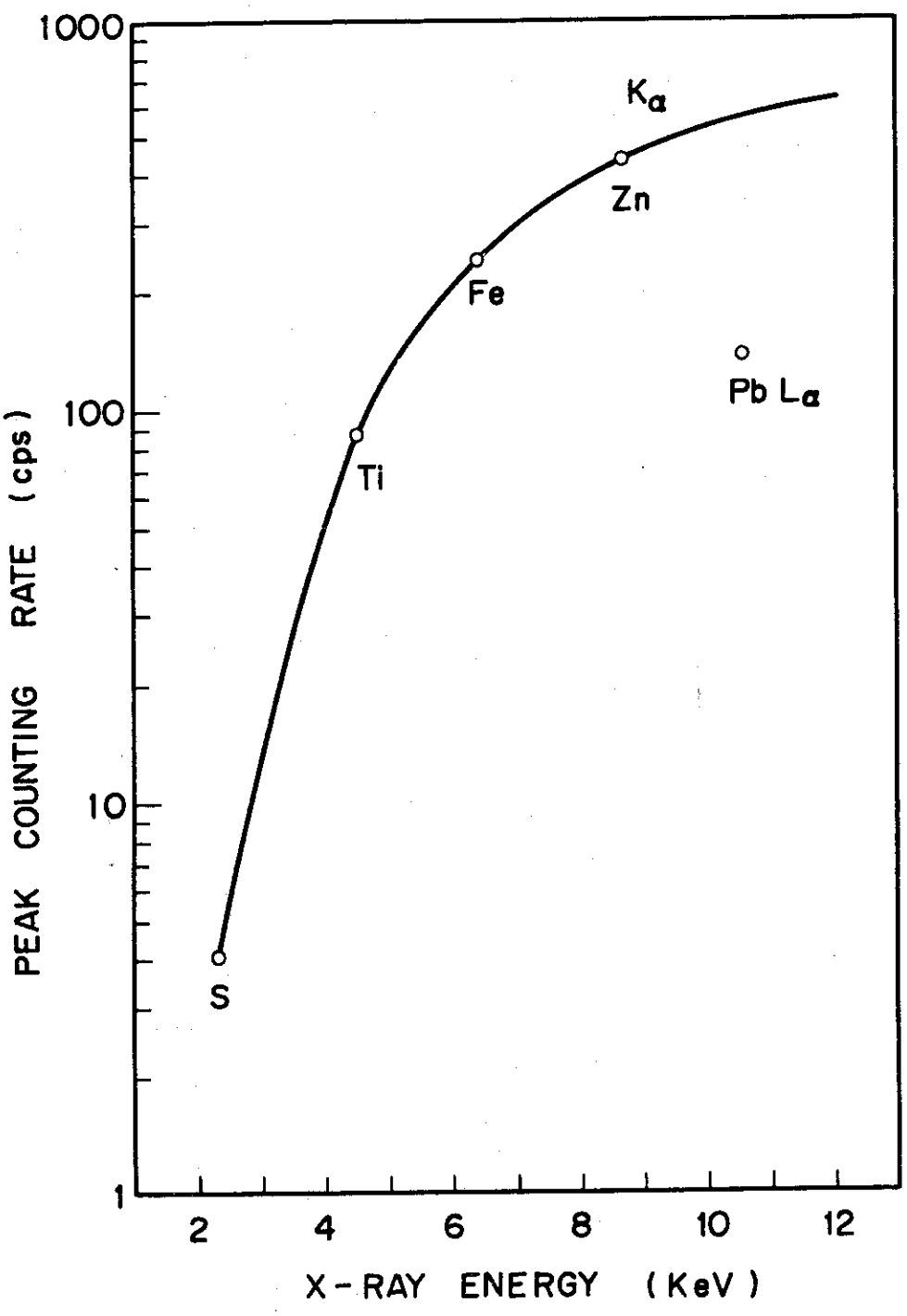

Fig. 50 Peak channel count of pure-element thick targets versus energy of the characteristic X rays, in the apparatus of Fig. 48 with 30 mCi ^{238}Pu X-ray source.

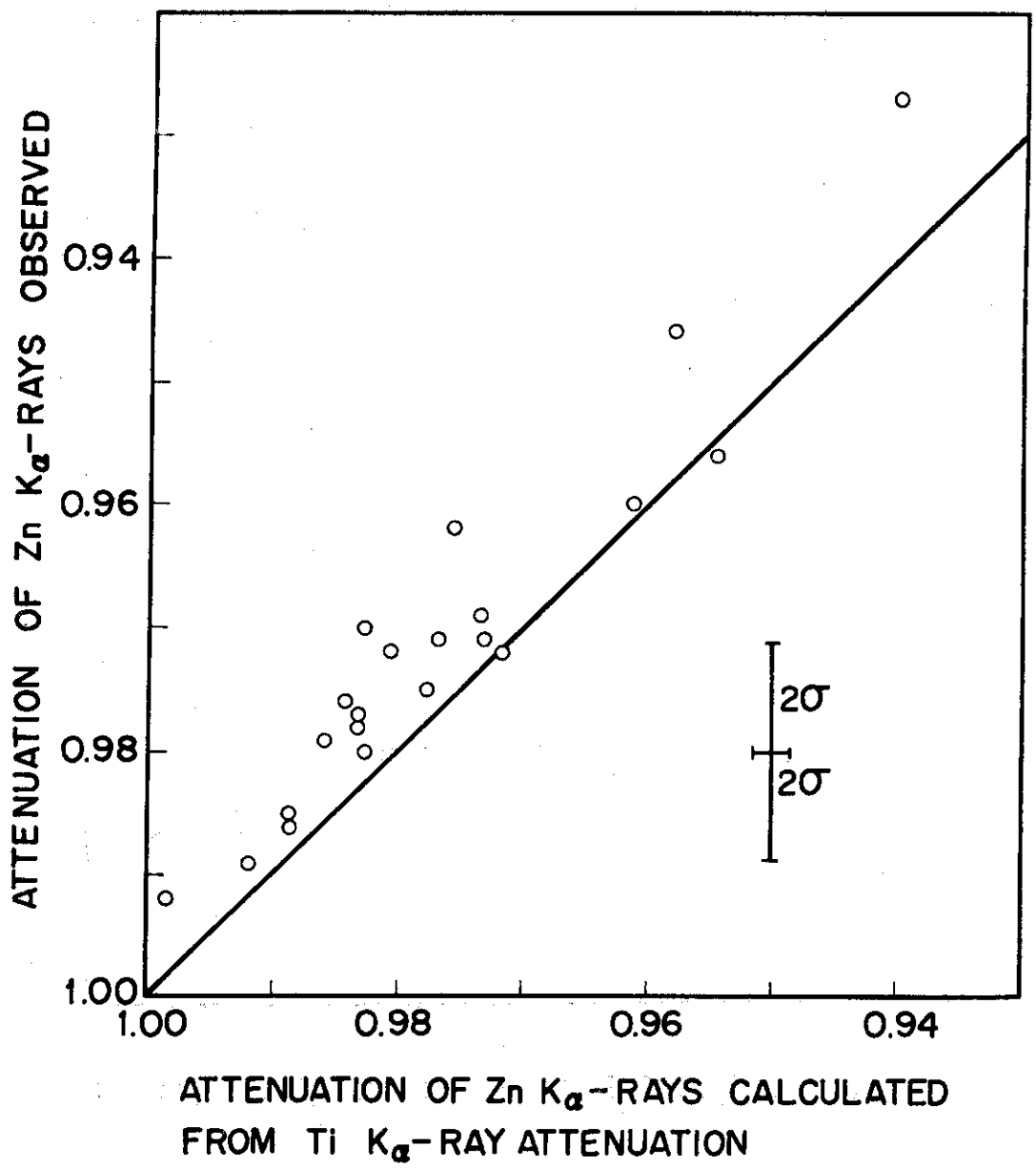

Fig. 51 Comparison between the observed and the calculated matrix absorption in airborne particulate specimens.

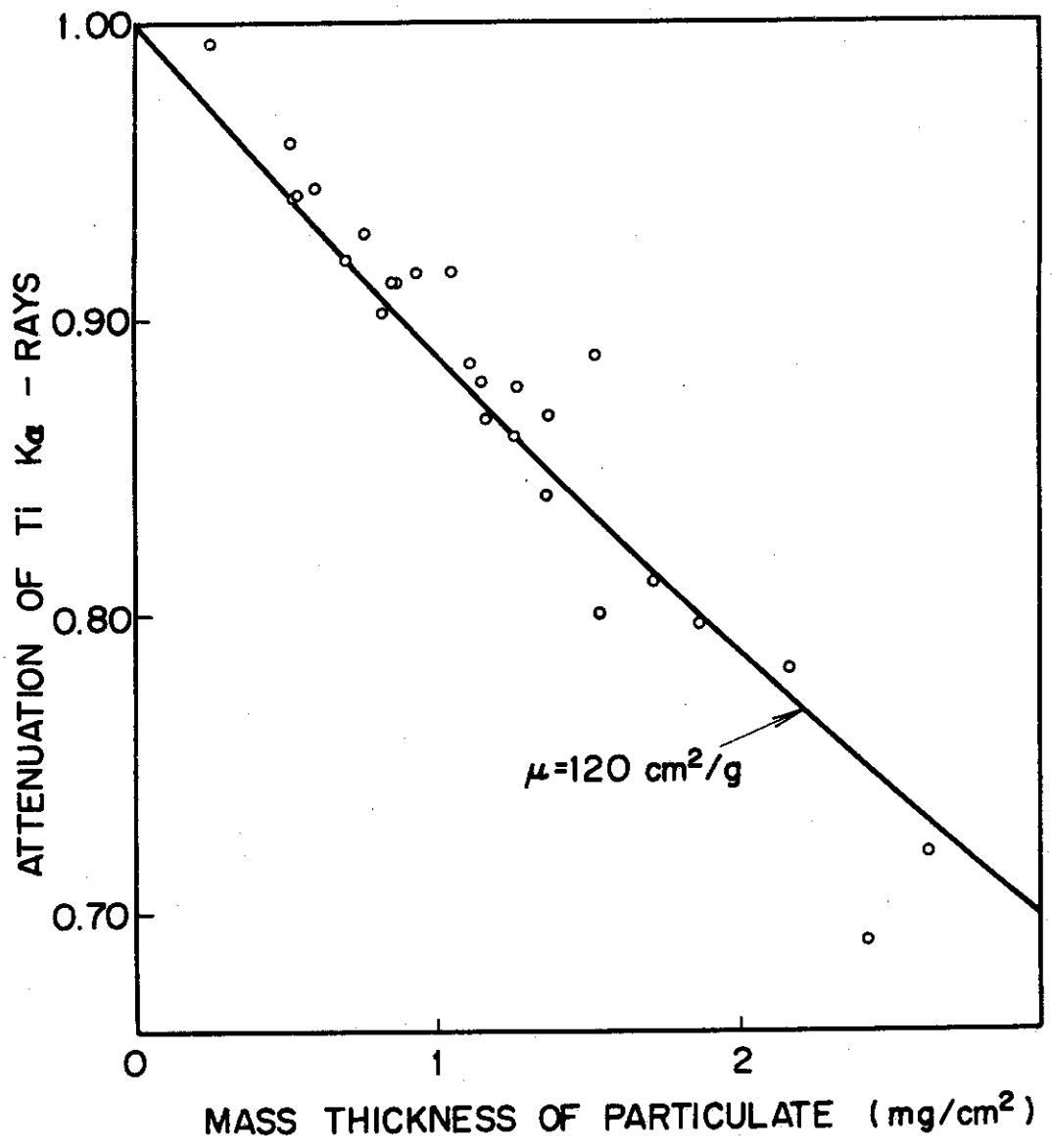

Fig. 52 Relation between the matrix absorption and the total mass thickness in airborne particulate specimens.

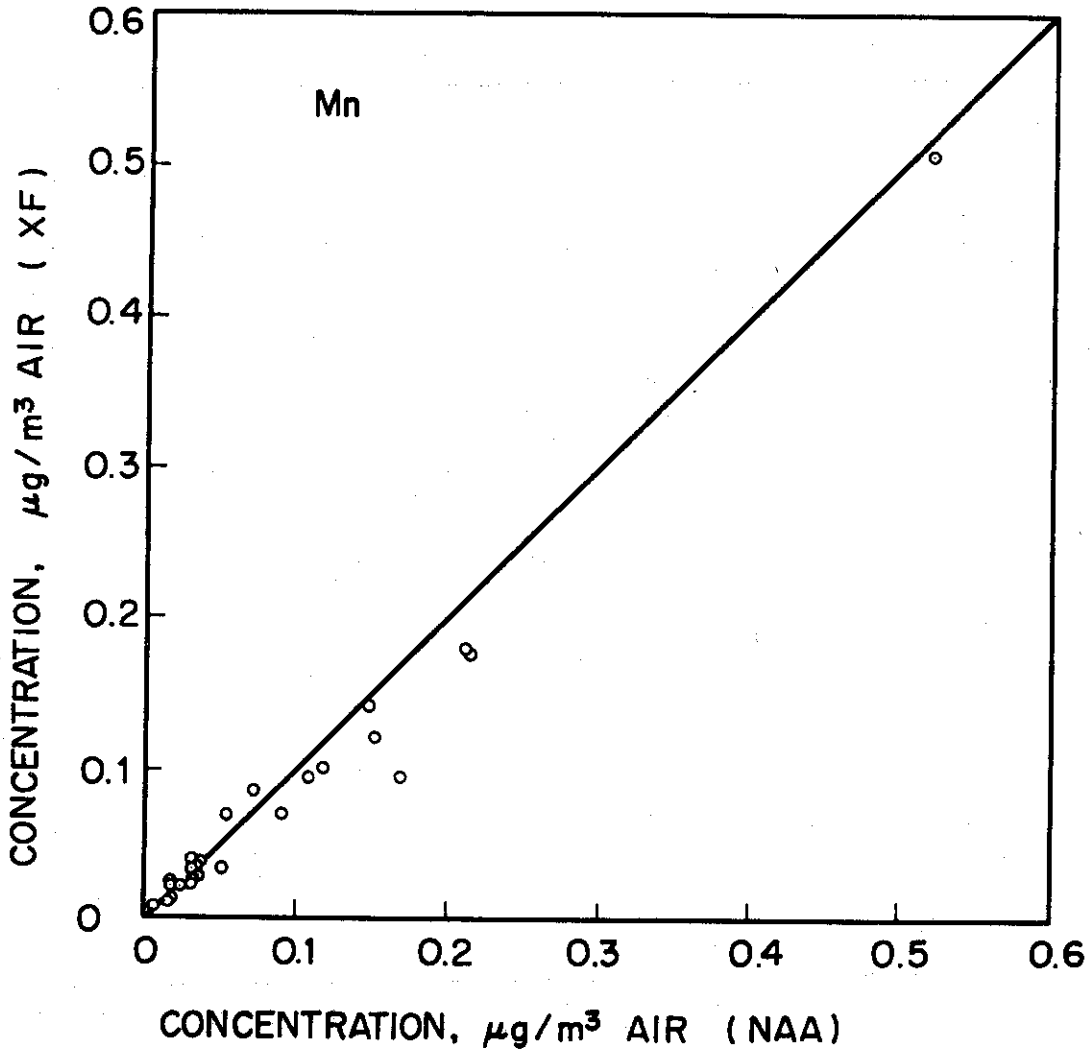

Fig. 53 Comparison of the fluorescent X-ray analysis with the neutron activation analysis, for manganese.

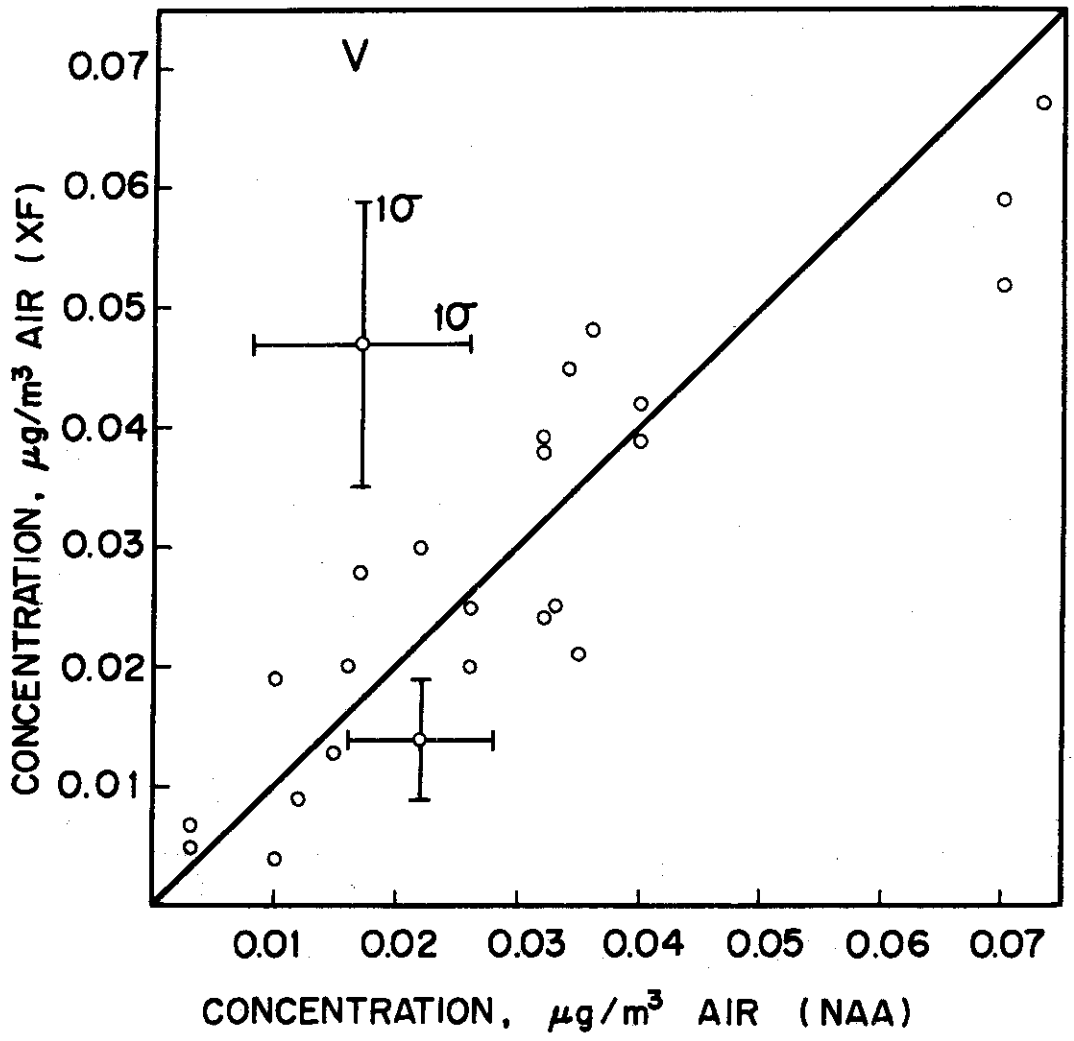

Fig. 54 Comparison of the fluorescent X-ray analysis with the neutron activation analysis, for vanadium.